POLITECNICO DI MILANO

Scuola di Ingegneria Civile Ambientale e Territoriale

Master of Science in Civil Engineering for Risk Mitigation

POTENTIAL OF AMBIENT SEISMIC NOISE CROSS-CORRELATION TO CHARACTERISE THE HYDROGEOLOGY OF A CLAYEY LANDSLIDE:

APPLICATION TO “MAS D’AVIGNONET” LANDSLIDE IN TRIÈVES REGION (FRANCE)

RELATORE: Prof. Stéphane Garambois

CORRELATORE: Prof. Laura Longoni

STUDENTE: Vincenzo Milesi

MATRICOLA: 817095

In collaborazione con:

Université Grenoble-Alpes,

ISTerre, Institut des Sciences de la Terre, France

ANNO ACCADEMICO 2014-2015

\

Table of contents

\

\

List of tables

List of figures

\

\

Acknowledgements

I would like to thank my supervisor prof. Stéphane Garambois because he allowed me to develop my work at ISTerre strongly supporting me along six months.

However, I could not achieve successfully my work without the special suggestions and the strong support offered by prof. Grégory Bièvre in hydrogeology and prof. Christophe Voisin in seismology. They gave me competently a great knowledge of new understandings getting me close to research environment.

I would like equally to thank prof. Laura Longoni for the coordination and the precious suggestions given supporting me in the decision to do my thesis abroad.

Moreover, I want to thank all the researchers and the students working at ISTerre because they kindly gave me their help. Particularly, I remember Christelle, Clara, Eric, Florent, Francesco, Helias, Lara, Mai-Linh, Marcello, Noélie, Philippe, Qingyu, Rose Mary...

Finally, I want to thank my family that gave me the possibility to study supporting me economically and morally. They taught me never give up keeping an open mind.

Anyway, my special thought is for my girlfriend, Lisa, because she always imparts me her determination making me stronger.

Merci beaucoup…
Grazie di cuore…

\

Abstract (Italiano)

Questo lavoro presenta uno studio multidisciplinare su una frana in argilla (“Mas d’Avignonet”) nelle Alpi Francesi, 40 km a sud di Grenoble monitorata permanentemente dal 2007 da OMIV (Ente per l’osservazione delle instabilità di versante). Dopo un’analisi iniziale degli studi messi in campo in passato e delle misurazioni ambientali (idrometeorologiche e geofisiche) effettuate da strumenti di monitoraggio dislocati in una zona particolarmente attiva della frana, il lavoro verte sull’applicazione del metodo di cross correlazione di rumore sismico ambientale. Questo metodo permette di ritrovare le variazioni temporali di velocità sismiche (dv/V) che vengono in seguito correlate principalmente con misure piezometriche (livello di falda superficiale) e indirettamente con le misurazioni meteorologiche (pluviometria, pressione e temperatura), topografiche (GPS), idrogeologiche (SP e TDR) e geofisiche con l’applicazione di metodi di resistività elettromagnetici (EM31) ed elettrici (ERT) precedentemente elaborate.

Il metodo, inizialmente basato sulla cross correlazione di rumore sismico (registrato su tre componenti per stazione) di una coppia di stazioni, è stato successivamente esteso cross correlando componenti differenti di una medesima stazione. Questo processo ha permesso, soprattutto per il primo caso, di ritrovare variazioni di velocità sismiche coerenti con le variazioni di falda superficiale per una determinata banda di frequenza delle onde di Rayleigh.

In seguito, abbiamo studiato il ruolo della saturazione dei fluidi nelle variazioni di velocità sismiche applicando la teoria poroelastica di Biot-Gassmann che considera il terreno un mezzo poroelastico con fase fluida. In particolare, abbiamo applicato leggi di omogeneizzazione della fase fluida, descrivendo l’influenza dell’acqua nella propagazione delle onde di Rayleigh. Il metodo permette infine la valutazione delle variazioni di velocità sismiche rispetto alla frequenza (considerando che il rumore sismico sia composto per lo più da onde di Rayleigh) spiegando quantitativamente i risultati ottenuti con la cross correlazione.

Il seguente lavoro mostra in prima analisi come il metodo di cross correlazione sia un valido strumento di monitoraggio non distruttivo permettendo di descrivere dinamiche idrogeologiche di frane in argilla. Tuttavia la complessità dei risultati suggerisce che la presenza di più stazioni consentirebbe davvero di raggiungere dei risultati soddisfacenti.

Parole chiave: *Frana; Argilla; Monitoraggio; Rumore sismico ambientale; Cross correlazione; Idrogeologia; Geofisica e Sismologia.*

\

Abstract (English)

This work focuses on the study of "Mas d'Avignonet" landslide, a slow moving clayey landslide located in French Western Alps, which benefits from a multi-parameter monitoring implemented by OMIV (Multidisciplinary observatory landslide) since 2007. After an analysis of the several studies carried out and after data acquisition from environmental measurements (meteorological, hydrogeological and geophysical), we apply cross-correlation of ambient seismic noise. This method allows the retrieval of seismic velocity variations over time. We assess its potential mainly through the correlation with piezometrical measurements (water table variations). However, we consider also meteorology (pluviometry, air temperature and pressure), geodesy (GPS), hydrogeology (SP and TDR) and geophysics with the implementation of electromagnetic (EM31) and electric (ERT) resistivity method.

Initially based on the cross-correlations of seismic noise between a pair of stations (each station records three components signal), we extend this method to a single station by cross-correlating the different signal's components. This processing allows obtaining local velocity changes. Particularly, we find that water table changes are consistent with seismic velocity variations for a specific frequency band of Rayleigh waves' signal.

In addition, we studied the role of fluid saturation on seismic velocity changes by using the Biot-Gassmann poroelastic theory. We focus on the influence of the water in Rayleigh waves' propagation considering a poroelastic medium with a fluid phase and by applying fluid substitution mixture laws. This approach allows assessing the amplitude of the velocity changes according to frequency (assuming the seismic noise being composed of Rayleigh waves) and to quantitatively explain cross-correlation results.

This work shows that cross correlation of ambient seismic noise method represents an effective non-destructive monitoring tool able to describe landslide hydrogeology in order to predict its dynamics. The results suggest that the method works but the complexity of the landslide could be completely explained by increasing the stations' number.

Key words: *Landslide; Clays; Monitoring; Ambient Seismic Noise; Cross-correlation; Hydrogeology; Geophysics and Seismology.*

\

1. Introduction

Landslides are one of the biggest hazard for the human planning and society development in mountain's regions. They are characterised by rock, soil and debris displacement under gravity effect (gravity hazard). These mass movements evolve with different velocities and their characterisation consists generally of three steps (Renalier, 2010): study of the affected area, stability analysis and dynamics evolution.

In this work, we will consider slow moving clayey landslide defined by literature as "soil creep" (Cruden and Varnes, 1996). The triggering factors are steepness of the slope, water absorption, material nature and vegetation of the area. However, water is primary factor provoking in clays a soil expansion and instability. Soil creeps move with a rate of few centimetres per year but water changes could activate catastrophic mudflows. We will study these considerations in "Mas d'Avignonet" clayey landslide in French Western Alps. This region (Trièves) made of quaternary glaciolacustrine clays (Bièvre, 2010) is vulnerable to mudflows. We recall "L'Harmalière" landslide in 1981 with 250.000 m^3 involved (Moulin and Robert, 2004) or "La Salle en Beaumont" landslide in 1994 with 1.3 million m^3 that claimed four victims and severe damages (Moulin and Chapeau, 2004).

The prediction of these events is the challenge of the people dealing with landslide monitoring in order to implement prevention measures. This work will move towards this purpose trying to develop a new non-destructive monitoring tool using seismology. Particularly, we will apply ambient seismic noise cross-correlation method describing landslide hydrogeology showing a correlation with piezometrical measurements (water table changes).

Researchers have more and more considered ambient seismic noise in Earth's subsurface imaging and monitoring in the last 15 years. They developed imaging techniques such as seismic tomography, reflection seismic or ultrasonic imaging representing Earth's interior structure. They produced good results in volcanos observing that small perturbations could be detected as temporal changes of seismic wave propagation properties like seismic velocity (Sens-Schönfelder and Wegler, 2006; Brenguier et al., 2008; Duputel et al. 2009; Mordret et al., 2014; Brenguier et al., 2011).

Sens-Schönfelder (2006) proposed passive image interferometry technique combining coda wave interferometry (Snieder et al., 2002) with the technique of passive imaging with noise. Coda wave interferometry estimates slight changes in mean shear velocity comparing multiple scattered seismic waves before and after a perturbation. This approach requires repeatable seismic sources getting similar waveforms of the multiple scattered waves before and after perturbation. Instead, passive imaging allows Green's function retrieval between two seismometers cross correlating a diffusive wave field detected by two instruments at the same time. However, Green's function, representing physically the ground response to seismic wavefield, could be retrieved cross correlating ambient seismic noise (Shapiro and Campillo (2004); Shapiro et al. (2005)). This method could acquire ballistic surface waves travelling between two receivers considering one source of the other (Campillo and Paul (2003)) but also scattered coda waves (Sens-Schoenfelder and Wegler, 2006). Therefore, passive image interferometry is a useful tool to monitor changes in hydrocarbon reservoirs, volcanoes (Sens-Schoenfelder and Wegler (2006) and fault zones (Wegler and Sens-Schoenfelder (2006)). At Mt. Merapi (Sens-Schoenfelder (2006)), seismic velocity variations showed a depth dependence to the hydrological model and particularly to rainfalls. These attainments were the basis for following developments.

Mainsant et al. (2012) focused on the importance of the daily cross correlation of ambient seismic noise in Pont Bourquin clayey landslide (Swiss Alps) showing that seismic velocity variations are an efficient

\

tool to predict its reactivation. Moreover he showed that the drop of seismic velocity variations is related to pore water pressure and consequently to the hydrological conditions. Larose et al (2015) proposed a review on daily noise cross correlation technique developing environmental seismology. It is then possible to detect waves' propagation changes due to thermal, hydrological and gravitational (landslide) effects.

The last two are very important because they represent the core of this work. Larose's paper, in hydrological forcing paragraph, depicts a remoulded sandstone landslide (Utiku, New Zealand) studied by Voisin and Garambois (2016). This case suggested that seismic ambient noise is sensitive to hydro-meteorological conditions making possible hydrological monitoring. Particularly, water table variations were well correlated with ambient seismic noise.

Prof. Garambois proposal was to develop my work at ISTerre (Institut des Sciences de la Terre) in Grenoble applying cross correlation of ambient seismic noise to "Avignonet" clayey landslide in order to confirm Utiku achievements. This landslide represents an important natural hazard because it hangs over "Saint Eynard" Lake reminding "Vajont" tragedy in Italy.

Ergo, this work aims to confirm ambient seismic noise cross correlation method with the development of a multidisciplinary monitoring study to Mas d'Avignonet clayey landslide. We will support this thesis firstly by studying meteorology (pluviometry, air temperature and pressure), geodesy (GPS), hydrogeology (SP and TDR) and geophysics with the implementation of electromagnetic (EM31) and electric (ERT) resistivity method. Finally, by considering the influence of the water in Rayleigh waves' propagation considering a poroelastic medium with a fluid phase and by applying fluid substitution mixture laws.

The first part (Chapter 2) will show a general overview of the case of study ("Mas d'Avignonet" landslide) taking into account the monitoring surveys and studies realised since the eighties. We will then analyse the multi-physical data collected in a degraded active area of the landslide. We will carry out the data interpretation correlating meteorology (pluviometry, air temperature and pressure), hydrogeology (piezometry, SP and TDR) and geodesy (GPS). We will then further investigate this active area with geophysical surveys performing electromagnetic method (EM31) and electrical resistivity tomography (ERT).

The following part (Chapter 3) represents the core of the dissertation. We will examine here cross correlation of ambient seismic noise method giving firstly a physical understanding of the principle with last academic attainments. Later we will apply the technique to seismic records of two seismological stations located on landslide using two methodological approaches. Seismic velocity variations detects medium changes (water table and fluid saturation). The first conventional approach consists in cross correlating the seismic records of the two stations while the second empirical approach considers the cross correlation of different components' records of a single station. We will analyse each phase of data processing and we will discuss about the results. We will take into account the physical understanding discussed in Chapter 2 correlating seismic velocity with water table changes.

In Chapter 4, we will study the role of fluid saturation on seismic velocity changes by using Biot-Gassmann poroelastic theory. We will consider the influence of the water in Rayleigh waves' propagation. We assume that the medium is poroelastic with a fluid phase. The correlation between the seismic velocity changes obtained by this approach and by cross correlating of ambient noise will be carry out.

\

2. Mas d’Avignonet clayey landslide characterisation

This chapter deals with the presentation and the characterisation of Mas d’Avignonet case study. It gives an opening overview description talking about geology, morphology and hydrology taking into account the monitoring surveys and studies realised since the eighties. Multi-physical data collected in a degraded active area of the landslide are processed and analysed. Then, data interpretation is carried out correlating meteorology (pluviometry, air temperature and pressure), hydrogeology (piezometry, SP and TDR) and geodesy (GPS). The final part of this chapter handles with geophysical surveys on active area by performing electromagnetic method (EM31) and electrical resistivity tomography (ERT).

2.1 Site description

2.1.1 Localisation and morphology of the site

The “Mas d’Avignognet” clayey landslide is located 40 km south of Grenoble in French Western Alps. The studied landslide is at the northern border of the Trièves region (*Figure 1*) that is a large depression (300 km^2) covered up by clayey sediments reaching until 200 m depth. This plateau (800 m a.s.l.) is drained by Drac River and its tributaries, Gresse and Ebron.

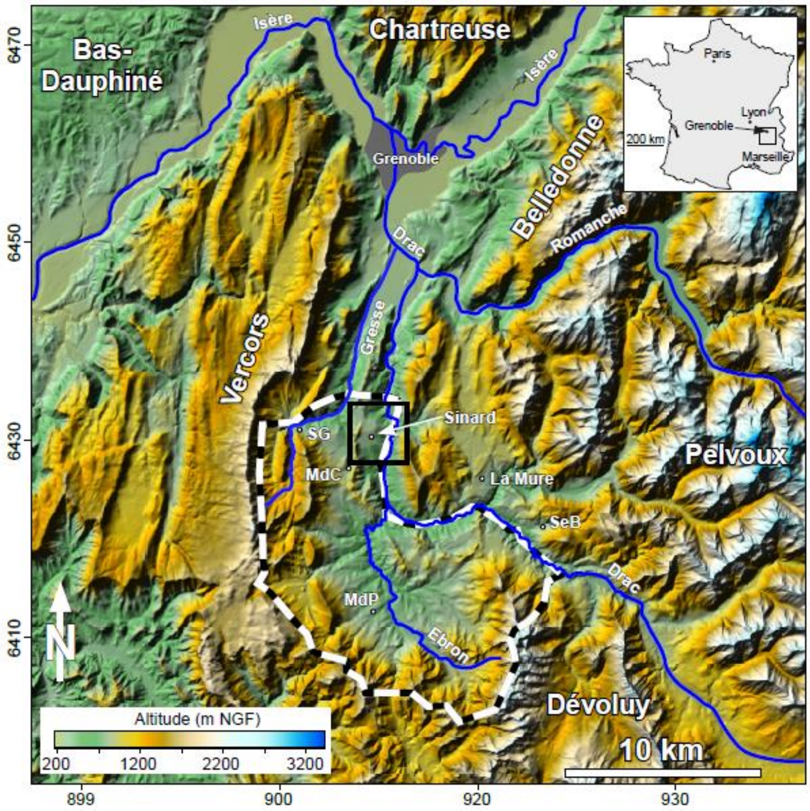

Figure 1 – *Geographical site location.*
The Trièves region, delimited by the dark and white dashed polygon, has a 300 km^2 surface and it is enclosed by Vercors Massif (West), Devoluy (South) and Belledonne - Taillefer (East). The black square focuses on the “Mas d’Avignonet” area. Figure recovered from Bièvre (2010).

The clayey sediments were drained after Wurm glaciation by the rivers and the sediments were destabilised engendering many landslides like “Mas d’Avignonet”. This landslide is located on the Drac’s left bank (western side) above the Monteynard Lake which was created by a dam built in 1962. Jongmans et al. (2008) considered that about 15 % of the clay cover is unstable and consequently

\

landslides are generated. Bièvre (2010) affirms that these landslides are moving slowly (few cm/year) but they could evolve in rapid mudflows. We remind l'Harmalière landslide in 1981 where 1.5 million m^3 of woods and meadows turn out into the Monteynard Lake (Moulin and Robert, 2004) or La Salle en Beaumont tragedy in 1994 where four people were killed and nine houses and the church of the village were destroyed or seriously damaged (Moulin and Chapeau, 2004). Simultaneously to Harmalière mudflow (1981) damages were observed in "Mas d'Avignonet" housing estate (Bronner, 2009). The site's morphology presents a slow slope at the border with the Sinard plateau and proceeding through east (Lake) this slope increases (*Figure 2*). The surface "Mas d'Avignonet" landslide is 1.6 km^2.

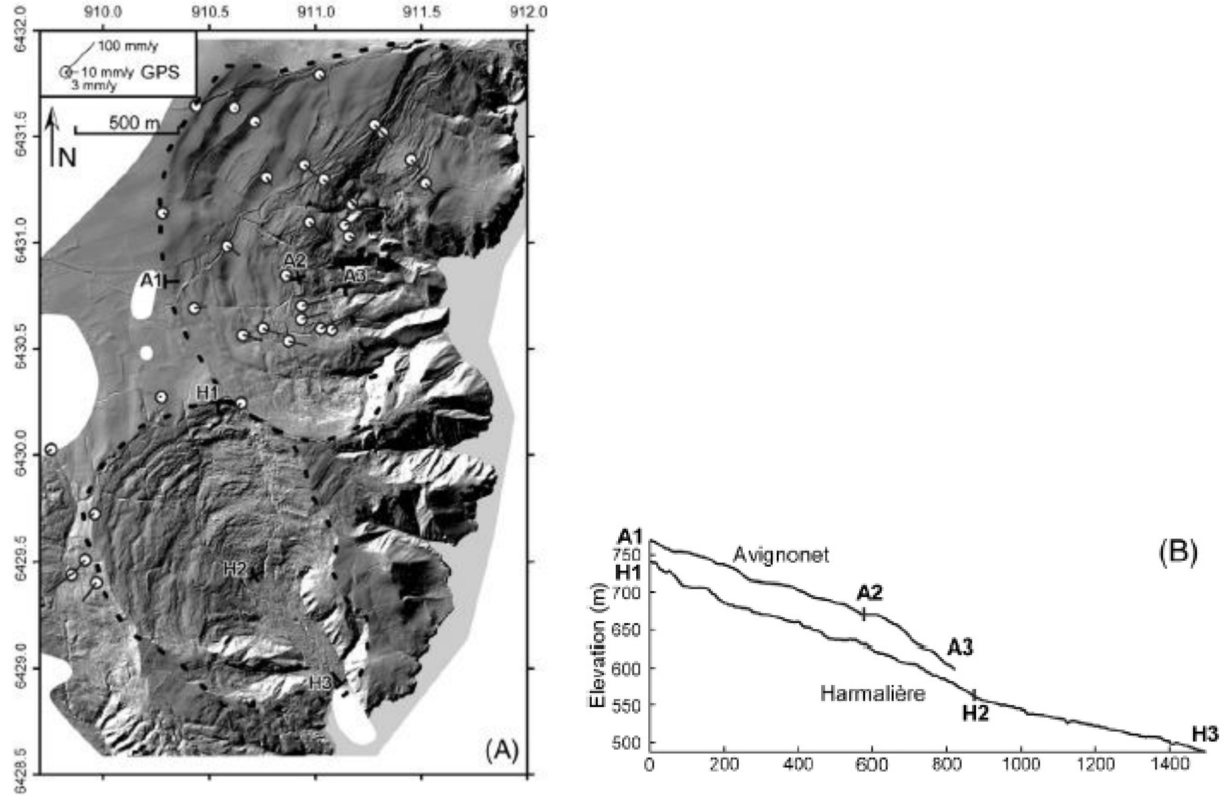

Figure 2 – Site morphology.
A) Lidar acquisition (campaign performed in November 2006) covering Avignonet (north) and Harmalière (south) landslides. The dark dashed lines are the landslides limits while the white circle are the GPS points and the thin dark lines represent the displacements along 11 year measurements. The A1-A3 (Avignonet) and H1-H3 (Harmalière) represent the points adopted to elevation profile. B) Elevation profile of the Avignonet and Harmalière landslides. From Bièvre (2010).

2.1.2 Geology and Hydrology

Geologically, this region is highly characterised by glaciolacustrine clays (Bièvre, 2010) that are susceptible to sliding *(Figure 3).* These clays (200 m layer) were formed in Quaternary during the Würm Glaciation when the Alpine glaciers (Isère glacier) occupied the Grésivaudan Valley and the Romanche Valley from North-East to South-West ending at Sinard in Trièves *(Figure 1).* Here the glaciers obstructed river Drac forming consequently a big lake allowing the formation of this clay layer (alternation of clays and silts) above the Jurassic Bedrock moulded by alpine orogenesis. This substratum was carved by glacial and inter-glacial phase allowing the formation of alluvial deposits. Morainic deposits stands over clays (southern border of the alpine glacier). Observing the section X-X' in the figure 3 we can see this geological distribution corresponding to Avignonet landslide *(Figure 3).*

\

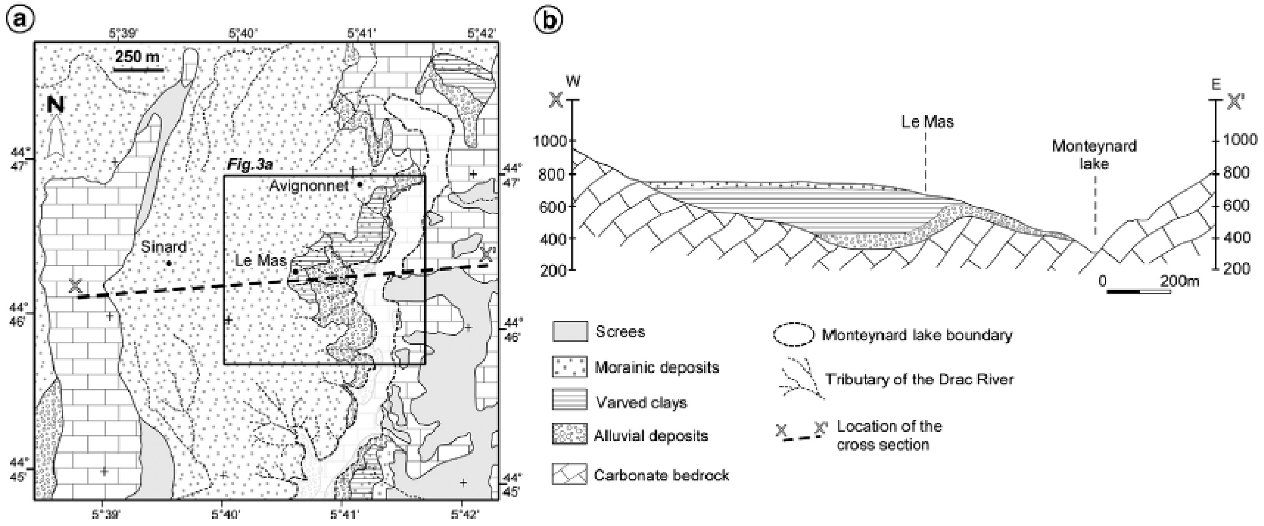

Figure 3 – *Geological model.*

a) Geology map of the "Mas d'Avignonet" landslide. b) X – X' the longitudinal section passing through the Mas housing estate. From Jongmans (2009).

The site's hydrology (*Figure 4*) is consistent with the geology because there are many streams emerging at different altitudes. Bièvre (2010) affirms that there are temporal sources at 750 m a. s. l. corresponding to morainic/clays interface. However, most of sources are located at 600-620 m at the clays/alluvial deposits interface. Finally, other sources in clays/silts layers at 700 m a. s. l. are probably due to the presence of rough sediments. Avignonet slope is a catch basin and the water flows go towards Monteynard Lake consistently with landslide displacements.

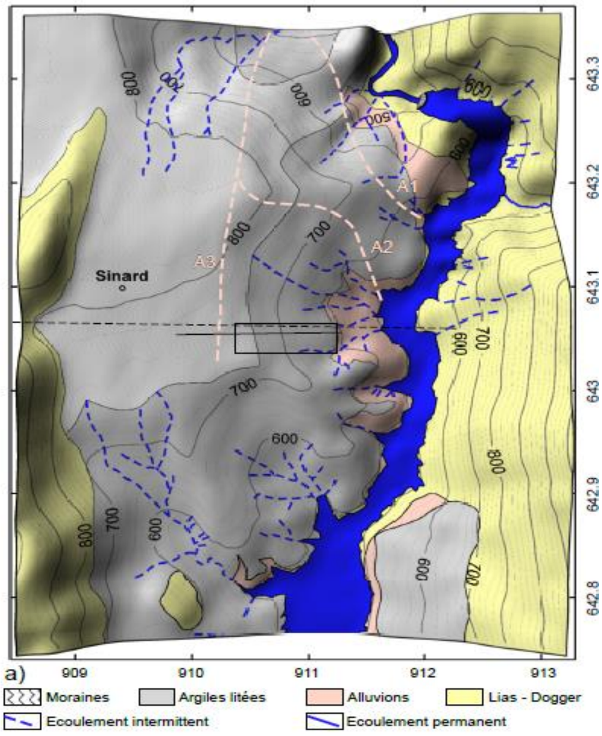

Figure 4 – *Hydrogeological model.*

Hydrogeology with geological map (morainic deposit is not represented) superposed with hydrographic network (temporary sources with dashed lines and permanent with continuous lines) and topography. Figure from Bièvre (2010).

\

2.2 Site characterisation

This section deals with the analysis of some environmental measurements recorded since 2007 by stations deployed in Mas d'Avignonet landslide *(Figure 5)* by OMIV (Multidisciplinary Observatory of Landslide). We will analyse here meteorology (rainfalls), hydrogeology (piezometry, TDR and SP) and geodesy (GPS) for the period 2008-2015 (like seismology records). The final part of this section (2.2.4) handles with geophysical surveys by performing electromagnetic method (EM31) and electrical resistivity tomography (ERT) on the active area where hydrogeology instruments (piezometers, TDR and SP) are present.

Figure 5 – Monitoring instruments location.
Meteorological (AVP2), piezometrical (sc_02, sc_bas and aquatroll), GPS (AVR_{GPS}, $AVP2_{GPS}$ and $AVN3_{GPS}$) and seismological (AVR_{SIS}, AVP_{SIS} and AVM_{SIS}) monitoring instruments deployed. Figure modified from Bronner (2009).

\

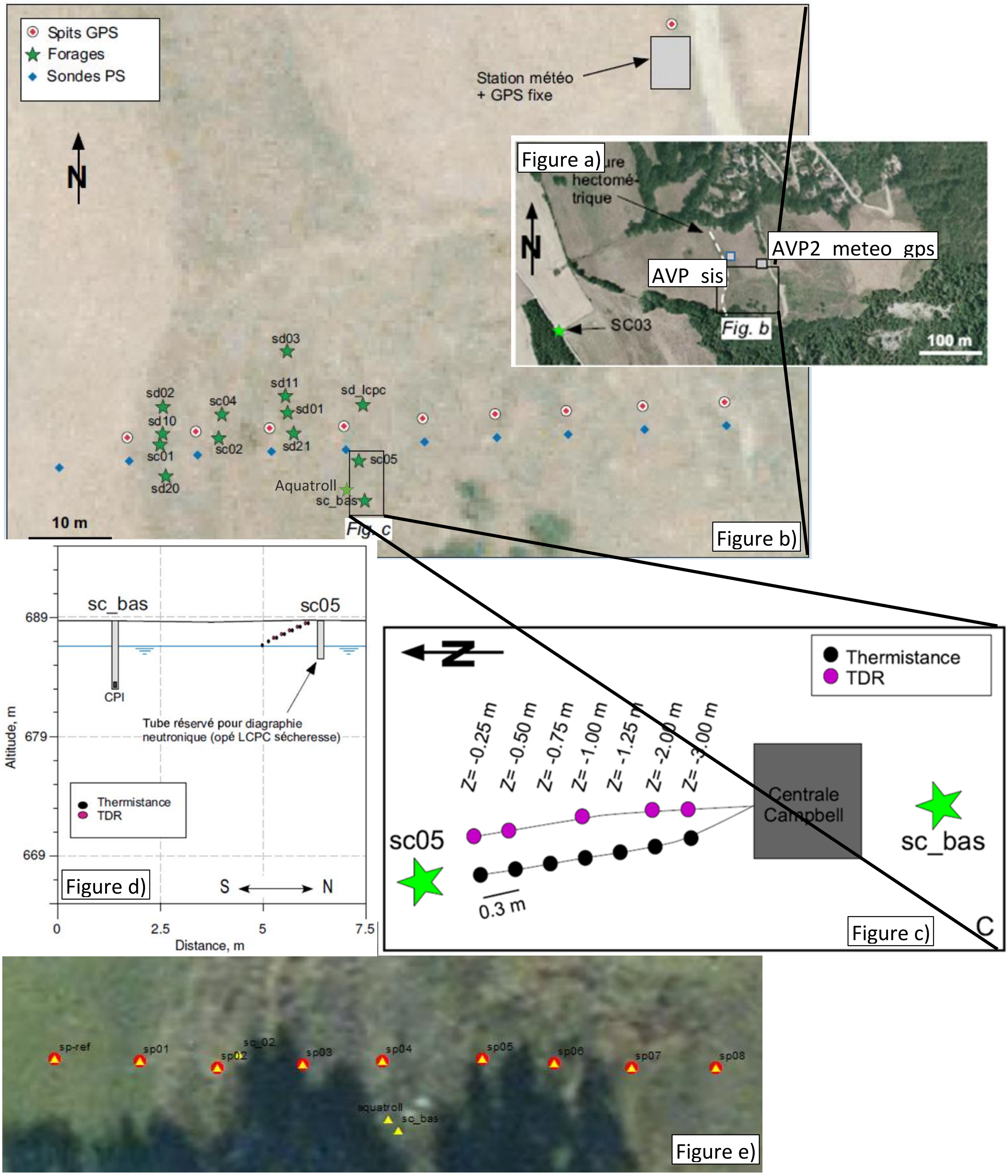

Figure 6 – *Monitoring instruments location in "Combe du Mas d'Avignonet".*
a) Degraded area is near the housing estate "Mas d'Avignonet" representing a real hazard, in fact the resident people have been evacuated. Therefore this area has been equipped by monitoring tools. b) Boreholes realised in the area (green stars), spontaneous potentials electrodes (blue dots) and GPS spits (red dots). c) Detail of the TDR and ground temperature tools. d) TDR sensor with respect to the depth. e) Detail of the spontaneous potentials electrodes (red circles and yellow triangles) and piezometers (yellow triangles). Figures a-b-c modified from Bronner (2009). Figure d has been realised using GIS tools.

\

2.2.1 Meteorology

This section deals with meteorological data acquisition and processing with a special regard to pluviometry measurements in results interpretation.

2.2.1.1 Instruments

The meteorological station installed nearby AVP2 - GPS station (*Figure 7*) getting data every 30 minutes since 2007. The measured parameters are rainfalls, air temperature, atmospheric pressure, wind speed and direction. Station performs also snow measurements that we did not process because of sensor malfunctioning. During my internship I processed all these parameters but for correlation purpose this paper presents rainfalls only.

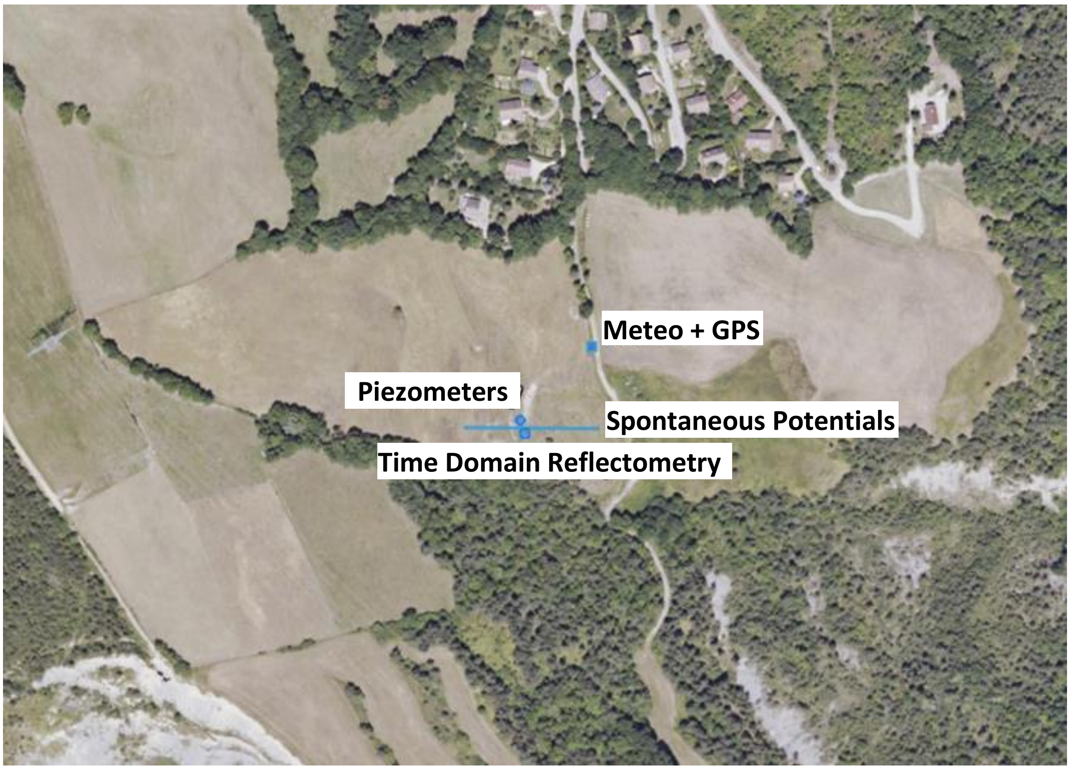

Figure 7 – Monitoring equipment overview.
"Combe du Mas d'Avignonet" area. Figure taken from OMIV website (http://omiv.unice.fr/index.php?page=meteo_avgn).

2.2.1.2 Data processing

Data acquisition is every 30 minutes. The data processing consists of converting raw data in .txt files removing not consistent data. Then we will implement them in MATLAB. We will represent in results section the pluviometry in rainfalls per day [mm/day] during the period of interest (2008-2015).

2.2.1.3 Results

We consider here below pluviometry *(Figure 8).* Data are available from the 1st of January 2008 until the 30th June 2015. However there are many missing data:

- from 06-12-2008 to 18-12-2008
- from 04-01-2009 to 27-01-2009
- from 01-08-2009 to 29-08-2009

\

- from 18-03-2010 to 22-04-2010
- from 30-06-2011 to 01-09-2011
- from 05-11-2011 to 19-01-2012
- from 01-03-2013 to 27-09-2014

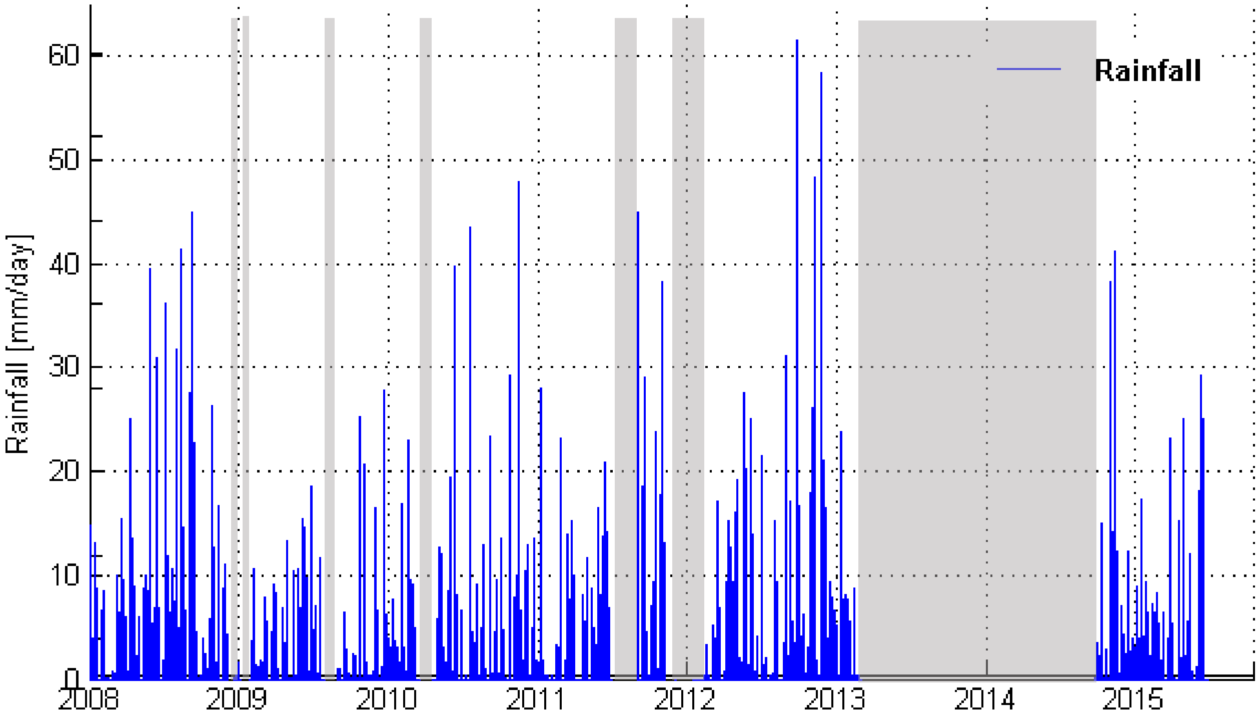

Figure 8 – Pluviometry at AVP2 station.
Rainfalls [mm/day] (blue stems) and missing (grey bands).

The pluviometry of the region is characterized by big amounts of rain in short times during the summers because of summer storms while relatively small rain amounts in winters even if the rain is better distributed. This feature is very important to understand the water table variations described in the next paragraphs.
The yearly amounts from 2008 to 2012 (from 2013 there is no sense to report because of data missing) are:

- 907.8 mm in 2008
- 500.6 mm in 2009
- 744.5 mm in 2010
- 569.4 mm in 2011
- 1046.6 mm in 2012

2.2.2 Hydrogeology

Bièvre (2010) described landslide's hydrogeology by the presence of two overlapping water table levels because of waterproof clayey layers. The upper-perched water table, detected by two different CPI sensors (sc_bas and aquatroll), is in the shallow layer (Vuillermet, 1994) directly dependent on pluviometry. Lower level is deeper and it depends on hydraulic standard of the massif. We will present here below their changes over time. This section presents firstly piezometry data acquisition, processing and results and a following correlation between pluviometry and piezometry over time.

\

Then, other two hydrogeological monitoring tools are considered (TDR and SP) and their results are interpreted correlating all the data presented before.

2.2.2.1 Instruments

Three CPI sensors equipped three boreholes (sc_02, sc_bas and aquatroll) in the degraded active area in Mas d'Avignonet landslide about 50 m far from AVP2 station (*Figure 6*). CPI sensors (Capteurs pression interstitielle) measure the interstitial pressure. It is possible to retrieve water depth from pressure as the level in which the measure is equal to atmospheric pressure neglecting rising damp phenomenon. Sc_bas and aquatroll sensors are at 5 meters depth while sc_02 is at 47.5 m. The sensors get data every 30 min (sc_bas and aquatroll) and every 10 min (sc_02).

2.2.2.2 Data processing

As mentioned before the raw data represent the interstitial pressure [mbar] that we converted in depth [m] using the formula (2.1) representing finally in absolute NGF altitude [m a.s.l.]. We input then in MATLAB recovering the water table variations.

$$h = \frac{P}{\rho \cdot g} \qquad (2.1)$$

Where h is the water height (m), P is the measured pressure (mbars), ρ is the specific weight of the water (1000 kg/m^3) and g is the gravity acceleration (≅10 m/s^2).

2.2.2.3 Results

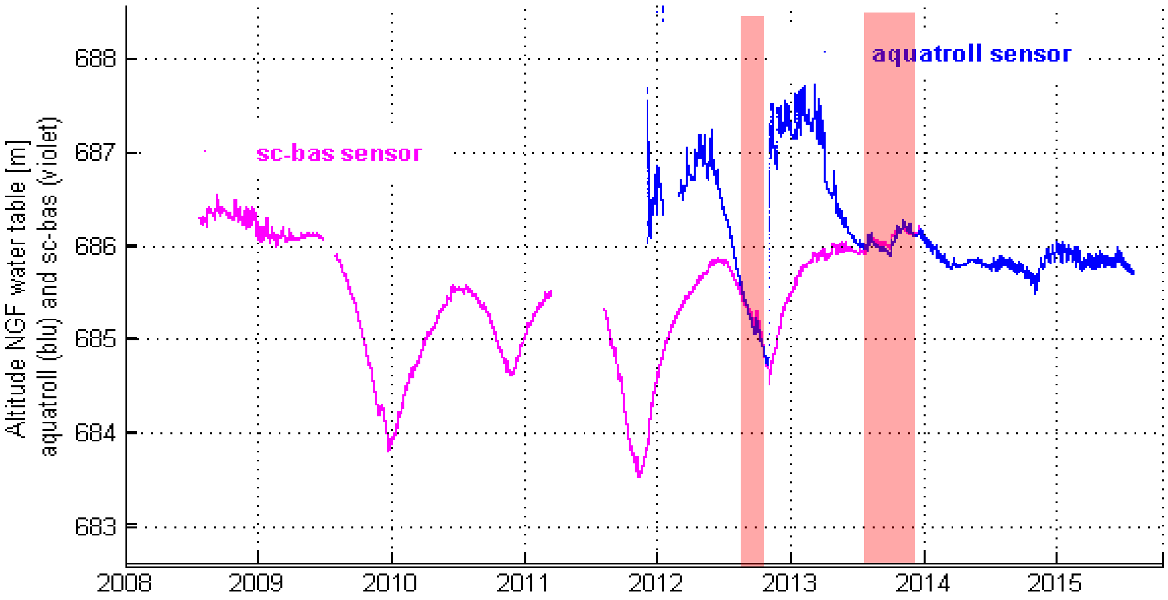

Figure 9 – *Upper-perched water table level.*
Aquatroll (blue) and sc_bas (violet) measurements are represented respect to the absolute altitude NGF. In fact, we converted interstitial pressure in water depth and then absolute values of altitude considering as references NGF altitude of sc_bas (688.58 a.s.l.) and aquatroll (687.849). The consistency between the two CPI sensors values is highlighted by the red transparent bands.

\

Starting from upper-perched water table oscillations (Figure 9), we see that the two sensors were not installed at the same time. Sc_bas worked from 2008 to 2014 while aquatroll from 2012 until nowadays. Sc_bas shows four regular annual oscillations from 2009 to 2013. We could see that replenishment phases occurred in spring and depletion phases in summer-autumn according to pluviometry and clay saturation (see paragraph 2.2.2.4). This regular trend was interrupted starting from 2013 but aquatroll results (sensor available from 2012) suggest an evident event the year before (2012). Particularly, overlapping the two trends, we could see that they are consistent in autumn 2012 but totally not consistent just before and after this period. However, they are again in accordance from summer 2013. Upper-perched water table remains constant and without annual oscillations until nowadays. These observations could be explained by the fact that the medium is prone to fissures (Bièvre, 2010). Their formation could be caused by landslide reactivation or by clay saturation. These assumptions could be verified correlating water table with GPS relative displacements even if GPS station is 50 m far from the piezometers (see paragraph 2.2.3).

We consider now the deeper water table variations over time measured by sc_02 CPI sensor that worked continuously from 21-11-2008 to 05-11-2015 with one year interruption (2014). Dataset (Figure 10) presents more or less a constant growth of the water table. This increase could alarm because of the potential reactivation of the landslide. However, it is much more probable that seepages flooded the borehole because of stresses and strains released in depth by landslide's fracture surface.

Figure 10 – Lower water table oscillations.
CPI sensor located at 47.5 m depth (sc_02 altitude is 692.6 m a. s. l.). We assume that the malfunctioning took place from the constant increase the 23-10-2010 when the drilling was probably ruined by the landslide activity.

\

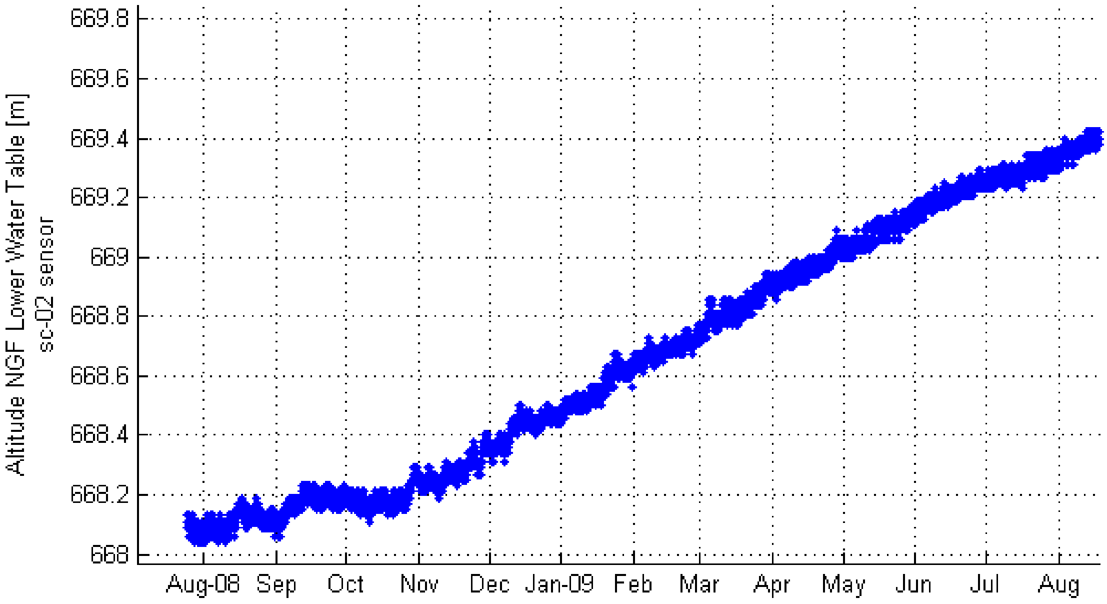

Figure 11 *– Lower Water Table values in the first year.*
We notice that the sensors worked well for the first three months. From the end of October 2008 the water table level started to increase constantly.

The only way to check out this assumption, it would be installing a new piezometer but it would be an expensive. Observing the complete data series (2008 to 2015) there are mostly three different increasing velocities with a probable ending stabilization. In order to solve this disadvantage we interpolated the data with a polynomial interpolation and we computed the standard deviation between the real data and the polynomial obtained (*Figure 12-13*).

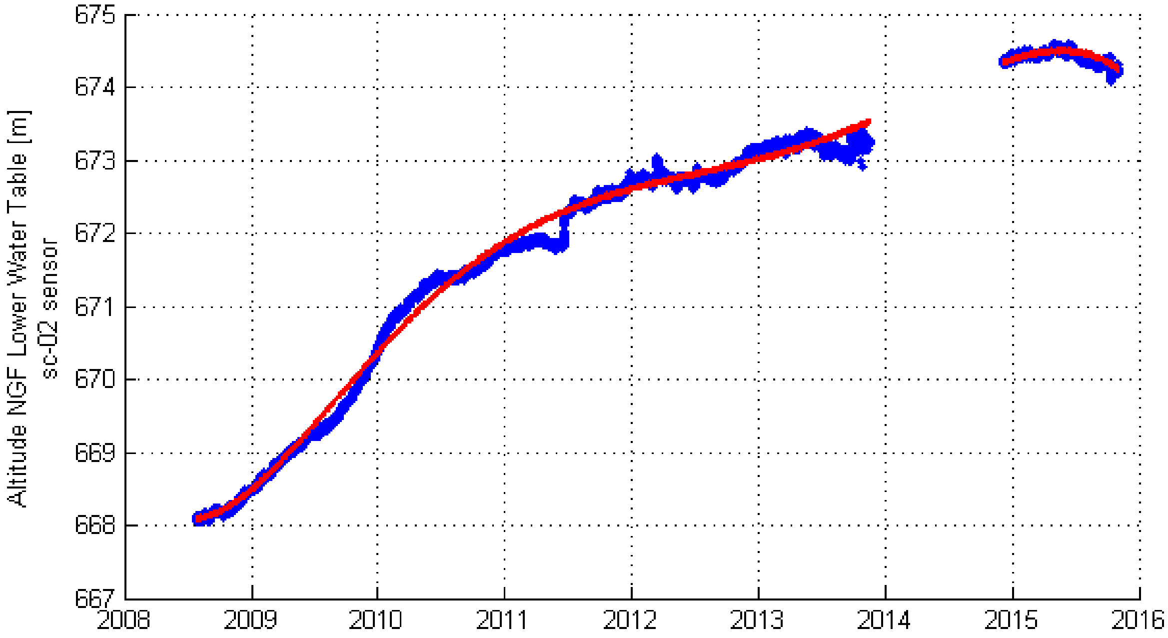

Figure 12 *- Lower water table level interpolation.*
Real values (blue) and interpolation line (red).

\

Figure 13 – *Corrected Lower Water Table.*

2.2.2.4 Correlation between Pluviometry and Piezometry

In order to better understand the results presented before about meteorology and piezometry, it is useful to correlate rainfalls with water table. Particularly, we considered the meteorological effects on upper-perched *(Figure 14)* and deeper *(Figure 15)* water table. These findings will be integrate our multidisciplinary monitoring study.

Bièvre (2010) focused on the importance of fissures in clayey landslides. In fact, these could generate destabilisation when extreme events occur draining rapidly water flows making worse mechanical properties of materials. Picarelli (2005) affirms that fissures could give a complex structure to affected materials. They subdivide them in blocks exposed to sliding (Bièvre, 2010). In long term the ground could have a pseudo-homogeneous appearance without fissures apparently (Picarelli et al., 2005).

In this case study fissures are mostly responsible for upper-perched water table changes because surface runoff is mainly associated to particular meteorological conditions. Particularly, heavy and rapid rainfalls during summer storms do not allow water absorption because of soil is not is not saturated and the high temperature causes fissures' generation. Therefore, rainfalls control variations of the upper-perched water table whose trend has been described before (paragraph 2.2.2.3).

Observing pluviometry records over time (see paragraph 2.2.1.3), we infer that 2008 was a rainy year (with 907.8 mm) maintaining the upper-perched water table more or less constant (686 m altitude) until the middle of 2009 when a 2 m drop occurred over 6 months probably due to minor precipitations (500.6 mm). It that moment, we suppose that clays were not saturated provoking a water table depletion and a surface runoff contributing to fissures formation especially during summer storm (heavy rainfalls in a limited period). After a minimum level reached at the end of autumn, the replenishment of the water table took place during winter and spring seasons where rainfalls and snowfalls permit clays saturation. This trend is recurrent until the beginning of 2013 even if 2010 and 2011 are characterised by low precipitations (744.5 mm and 569.4 mm). The turning point is 2012 during the replenishment at the end of autumn (2012 is the most rainy year with 1046.6 mm). In fact, from 2013 the upper-perched water table is constant around 686 m.

\

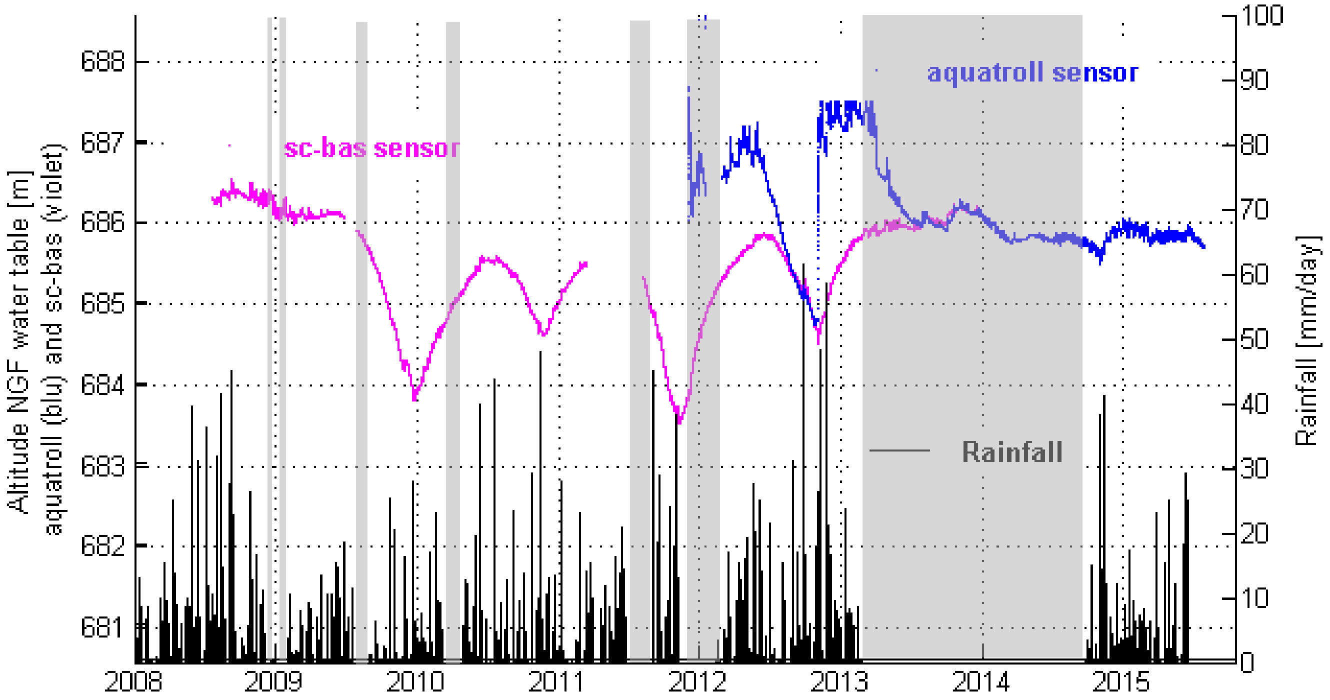

Figure 14 – *Comparison between upper water table and pluviometry.*
Comparison between upper water table measured by sc_bas (violet) and aquatroll (blue) sensors and the rainfall (mm/day) (black). The transparent grey bands means no data.

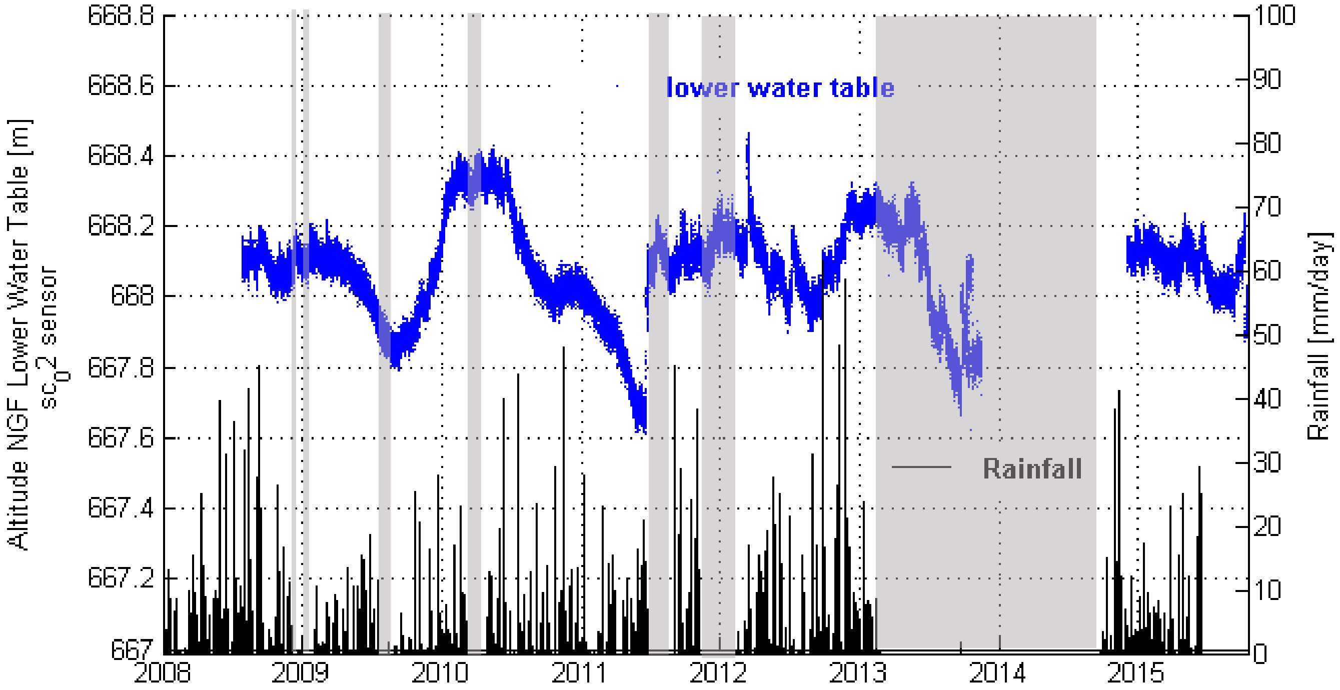

Figure 15 – *Comparison between lower water table and pluviometry.*
Comparison between lower water table (blue values) measured by sc_02 and rainfalls (mm/day) (black stems).

\

2.2.2.5 Time Domain Reflectometry

Time Domain Reflectometry (TDR) allows to retrieve soil's volumetric water content (VWC) variations over time dealing with the description of the saturated zone where rising damp occurs. This aspect will be useful for the Biot-Gassmann poroelastic theory (see paragraph 4.1). TDR probes measure the time round taken by the electromagnetic wave to pass through the stem inserted in the soil at different depth. Bièvre (2010), in order to retrieve the electromagnetic wave velocity, considered as velocity definition equation (2.2):

$$V \approx \sqrt{\frac{c}{K}} \tag{2.2}$$

V = electromagnetic wave velocity [m/s].
C = electromagnetic wave velocity in vacuum [3 x 10^8 m/s]
K = dielectric constant

In addition, he took into account the empirical equation (2.3) (Topp et al., 1980):

$$\theta_v = -5.2 \times 10^{-2} + 2.2 \times 10^{-2}\, K - 5.5 \times 10^{-4}\, K^2 + 4.3 \times 10^{-6}\, K^3 \tag{2.3}$$

Θ_V = Volumetric Water Content
K = dielectric constant

TDR probes were deployed in the degraded active area in Avignonet landslide *(Figure 6)*. They were inserted at different depth in the soil (0.25 – 0.50 – 1.00 – 2.00 – 3.00 m) and connected to "Centrale Campbell" that also process ground temperature with 7 probes parallel to TDR *(Figure 6c).* They were set within a clay-silt matrix (21 % of clays, 71 % of silts and 8 % coarser than 50 μm) except at 1 m depth where the soil is coarser (14% of clays, 41% of silts and 45% coarser than 50 μm) revealing a local vertical heterogeneity (Bièvre, 2010). These considerations are confirmed by the results *(Figures 16-17).*

We processed raw data converting in a format acceptable by Matlab for implementation. Data were available from 2009 to 2013. We present here dataset trends correlated with rainfalls *(Figure 16)* and upper-perched water table *(Figure 17).*

The results depict annual oscillations suggesting an evident correlation with pluviometry and piezometry. The VWC is mainly due to clays saturation changes. Particularly, autumn-winter-spring rainfalls and snowfalls allow an increase of water saturation observable consequently in upper-perched water table replenishment. Summer, characterised by high temperature and prolonged dry period, facilitates a decreasing in volumetric water content. Moreover, results suggest also the local vertical heterogeneity with the oscillations depicted by the sensor at 1 m depth. In fact, as it is a coarser layer, the saturation response will be different showing a sudden reaction to water respect to the other sensors that have longer reaction over time.

Unfortunately TDR station broke at the beginning of 2013. It could be interesting to see the water saturation response with the relevant event described previously by pluviometry and piezometry.

\

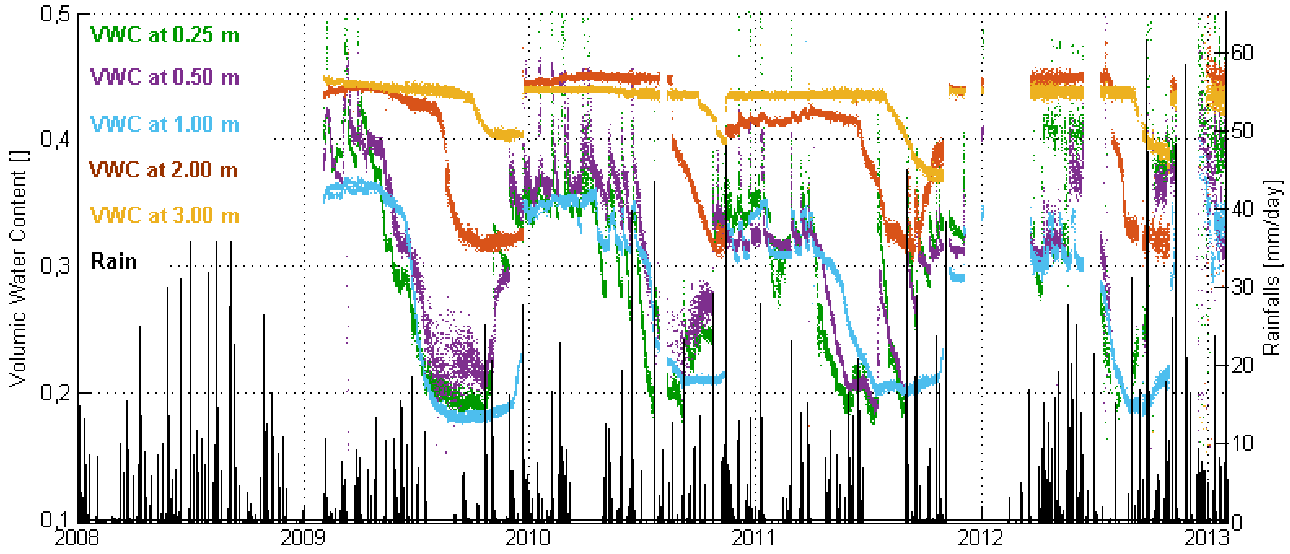

Figure 16 – Comparison between volumetric water content and pluviometry.
Comparison between volumetric water content (vwc) measured by Time domain Reflectometry and Rainfalls from 01-01-2008 to 01-02-2009.

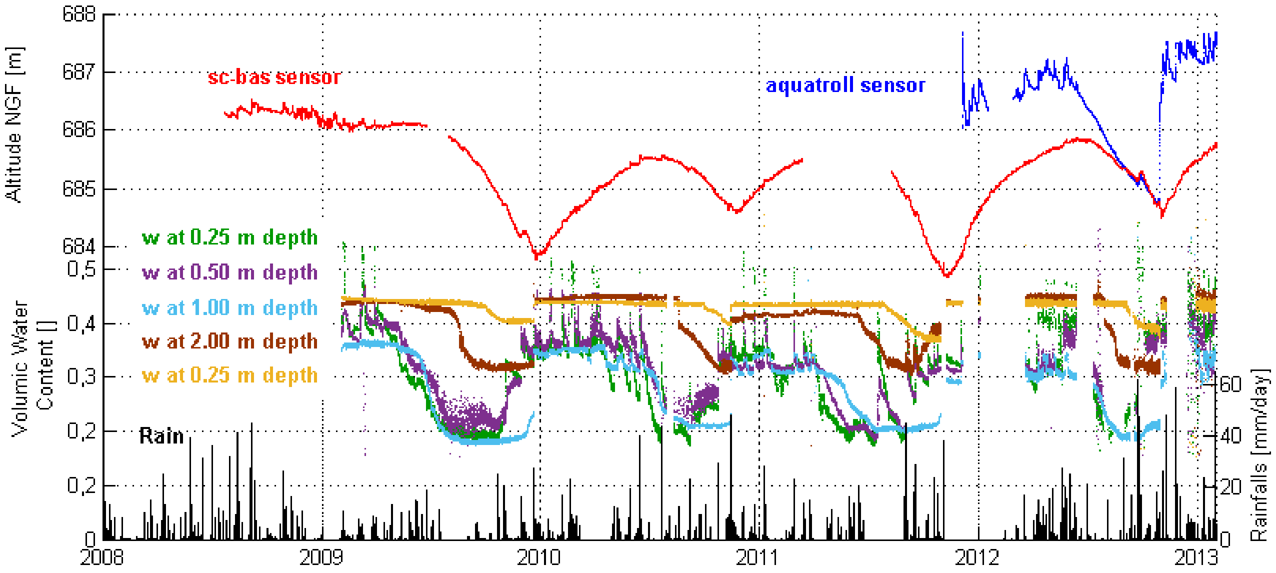

Figure 17 – Comparison among TDR, piezometry and pluviometry.
Comparison among volumic water content (w - TDR), Piezometry (upper water table measured by sc_bas and aquatroll CPI sensors) and Pluviometry (Rainfalls per day with black stems).

\

2.2.2.6 Spontaneous Potentials

Spontaneous potentials (SP) are by definition naturally occurring (static) electrical potential in the Earth that are usually caused by the charge separation in clays or other minerals, by the presence of a semipermeable interface impeding the diffusion of ions through the pore space of rocks, or by natural flow of a conducting fluid (salty water) through the rocks (Bièvre, 2010). Variations in SP can be measured in the field and in wellbores to determine variations of ionic concentration in pore fluids of rocks. Therefore, SP is a passive electric method. It consists of measuring the electric potential created by electrochemical causes, like minerals interactions, electro kinetic process, temperature and pressure gradients and mechanical activity of the fluids (Bièvre, 2010). Therefore, it provides information about groundwater movements or seepages (Corwin, 1990).

The instrumentation consists of electrodes' couples inserted in the soil and connected to a voltmeter that measures the voltage between a fixed liquid-junction reference and 8 electrodes located along the slope (Figure 6e).

Bièvre (2010) adopted this measurement to support DC resistivity electrical profiles realised in 2008 and 2009 (see paragraph 2.2.4.2). This surveys aimed to identify a resistivity anomaly in the degraded active area in Avignonet landslide (*Figure 6).*

We processed raw data in Matlab that we represented over the period of interest (2008-2015). The dataset *(Figures 18 and 19 zoom)* suggest that until 2012 the values did not present large oscillations maintaining on positive potential values. In 2012 the values were gathered with a positive oscillation. However, from 2013 (probably after the landslide reactivation event occurred at the end of 2012) the values are more scattered with larger oscillations and negative potentials. We can distinguish that the oscillations are inversely proportional to the upper-perched water table changes. The instruments could be affected by a malfunctioning because these oscillations are too large respect to the first period. Moreover, the values measured from 2013 are not specific of the clays. Therefore, it is recommended to calibrate again the instruments because of these probable amplification's effects.

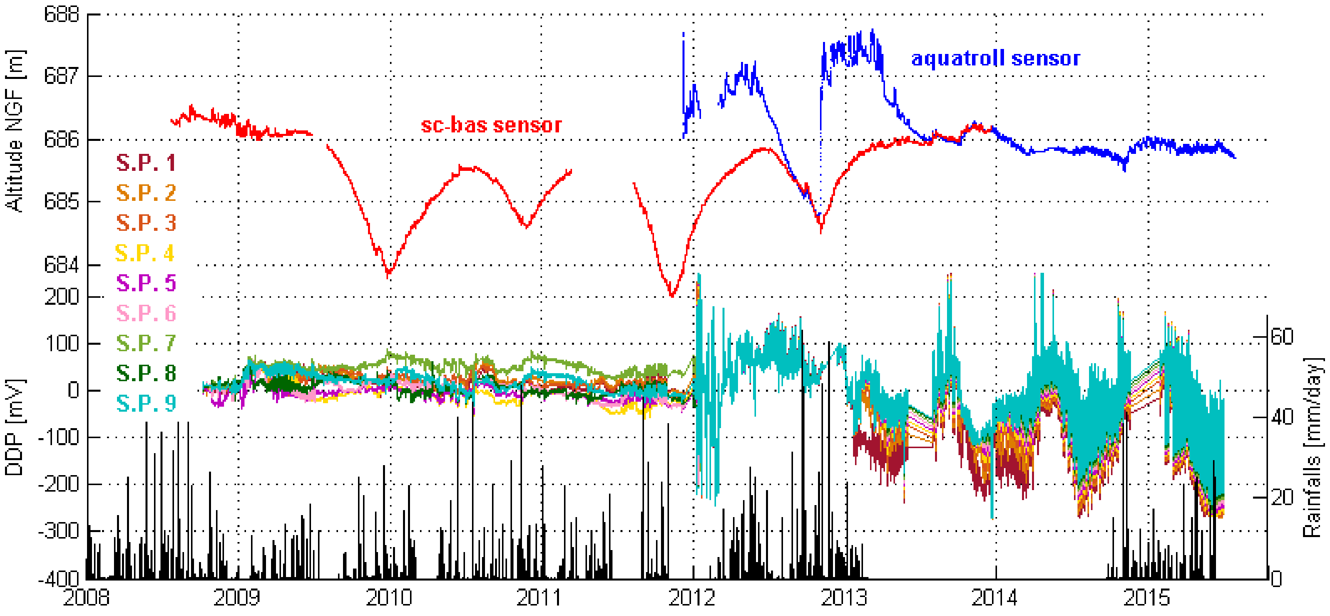

Figure 18 – *Comparison among SP, piezometry and pluviometry.*
Comparison among spontaneous potentials (S.P.), upper water table level (measured by sc_bas (red) and aquatroll (blue), the rainfalls in black.

\

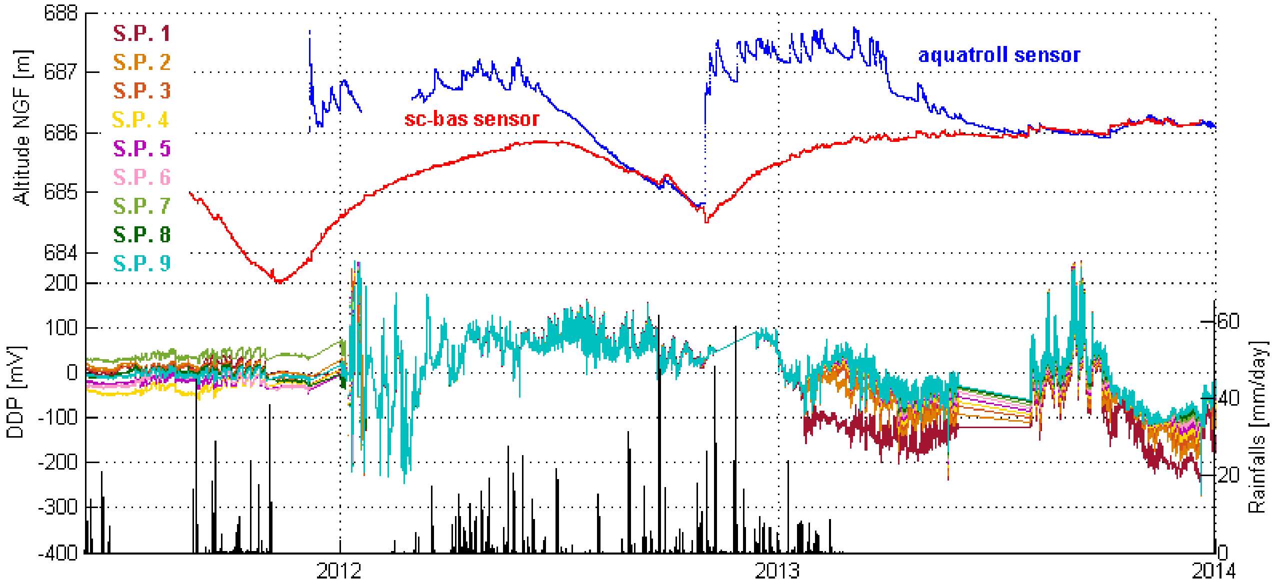

Figure 19 – *Comparison among SP, piezometry and pluviometry.*
The spontaneous potentials in more detail focusing on the changing behaviour during 2012.

2.2.3 Geodesy

The considerations about meteorology, piezometry and ground hydrogeology could be supported also by geodetic experiences. Particularly, we focused on AVP2 GPS station *(Figure 6)* that records continuous data until now. Representing the GPS data in the three component North (N), East (E) and Vertical (Z) we can infer the landslide relative displacements and direction. We can infer that the displacements are markedly in East direction *(Figure 20)* according to slope. In fact, East relative displacements are increasing while the North displacement are practically null the period; the elevation (Z) component experiences a light increasing until 2012 when it started decreasing.

The GPS dataset are consistent with the opening of a fissure in 2012 (see paragraphs 2.2.2.3 and 2.2.2.4) orientated North-South; the direction of the opening is East-West hence the differential movement of East component, the stillness of North component and the decrease of the elevation component Z.

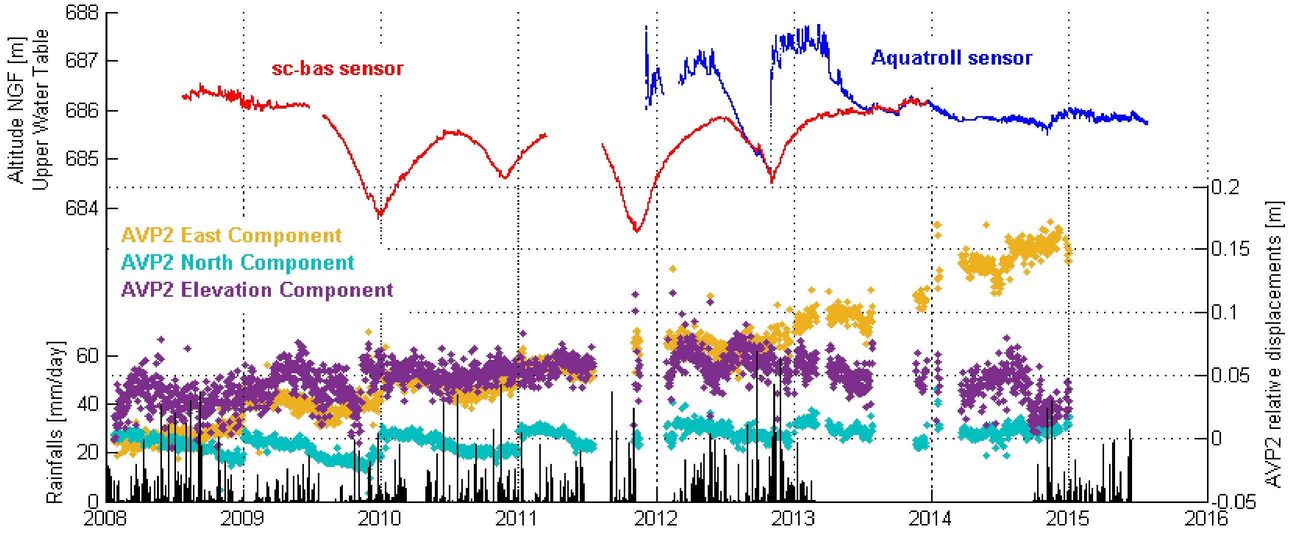

Figure 20 – *Comparison among GPS, piezometry and pluviometry.*
Comparison of GPS relative displacements in the three components (East (yellow) – North (blue) and Vertical (violet)) with upper water table (sc_bas (red) and aquatroll (blue)) and rainfalls in black. It is

\

important to notice that from 2008 to the beginning of 2015 the relative displacements have a value of about 15 cm with an acceleration at the end of 2012.

2.2.4 Geophysics

Meteorological, hydrogeological and geodetic measurements are performed in the degraded active area because of its rapid evolution respect to the surroundings. This area has been investigated for the last years also by several geophysical surveys (Bièvre, 2010). Particularly, in this work we focused on the conductive anomaly seen by previous electrical profiles performed in 2008 and 2009. In order to localise spatially and identify its composition, we implemented resistivity geophysical surveys. Particularly, we applied firstly the electromagnetic method (EM31) and then the electrical resistivity tomography (ERT) figuring out its surface extension (EM31) and its spatial distribution in depth (ERT).

2.2.4.1 EM31 campaign

We realised an electromagnetic campaign with EM31 (performed on 02-12-2015) in order to detect surface resistivity (conductivity) anomalies of the degraded active area. In fact, EM31 is able to measure rapidly the soil conductivity between 0 to 6 m depth (depending on orientations) allowing the retrieval of anomalous values due to different geology formation, water flows and foreign bodies.

It is an electromagnetic induction system (*Figure 21)* with a 9.8 KHz frequency that is portable and battery dependant. It has a couple of sensors put on a rigid beam with an inter-spacing of 3.66 m and transported by walk covering the interested area. It measures the apparent conductivity (ground conductivity) in (mS/m) and the in-phase ratio of the secondary to primary magnetic field in parts per thousand (magnetic susceptibility) (ppt), registered in a data logger with GPS positions (*Figure 22).*The beam has a sender and receiver coil. The sender induces electrical current circuits in the soil. The intensity of electrical circuits is directly proportional to soil conductivity crossed. Every secondary loop in soil generates a secondary magnetic field proportional to the electrical current of the associated circuit. The receiver coil detects a part of this field in the form of a potential difference signal. The equipment is calibrated to average conductivity values if the ground presents layers with different conductivity values. The unity of measure of conductivity is the (mS/m) that is converted into (Ohm x m) to represent the resistivity.

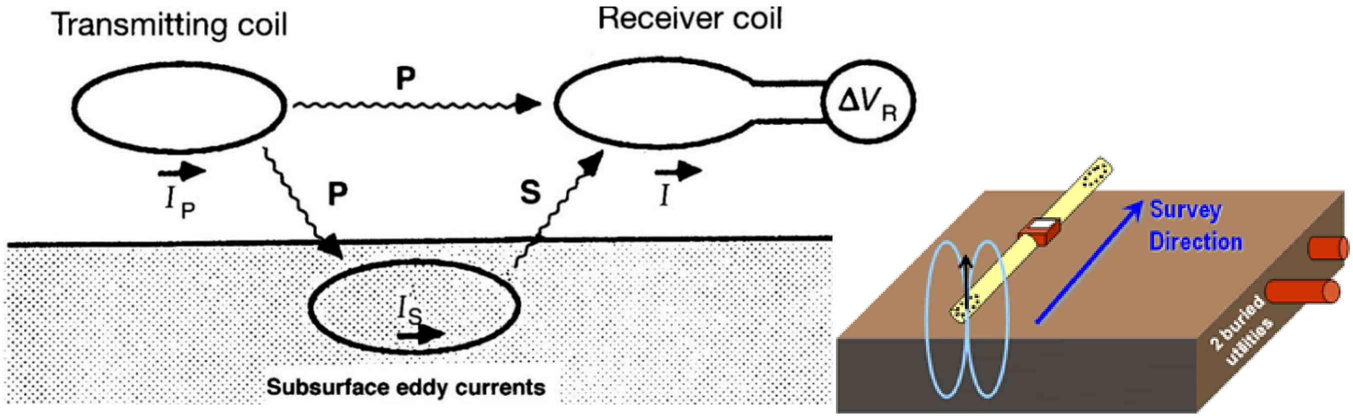

Figure 21 – *EM31 physical principle.*
EM31 functioning: I_p *is the current emitted by the transmitting soil,* I_s *the induced current in the soil and I the current. P and S are the lines of the primary and the secondary magnetic fields induced.* ΔV_R *is the voltage detected by the receiver coil.*

\

The measure was taken with the vertical dipole (beam parallel to survey direction) allowing a deeper investigation in the soil that is the double of the horizontal one (beam perpendicular to survey direction). We traversed the area walking in parallel lines in north-south direction perpendicularly to slope.

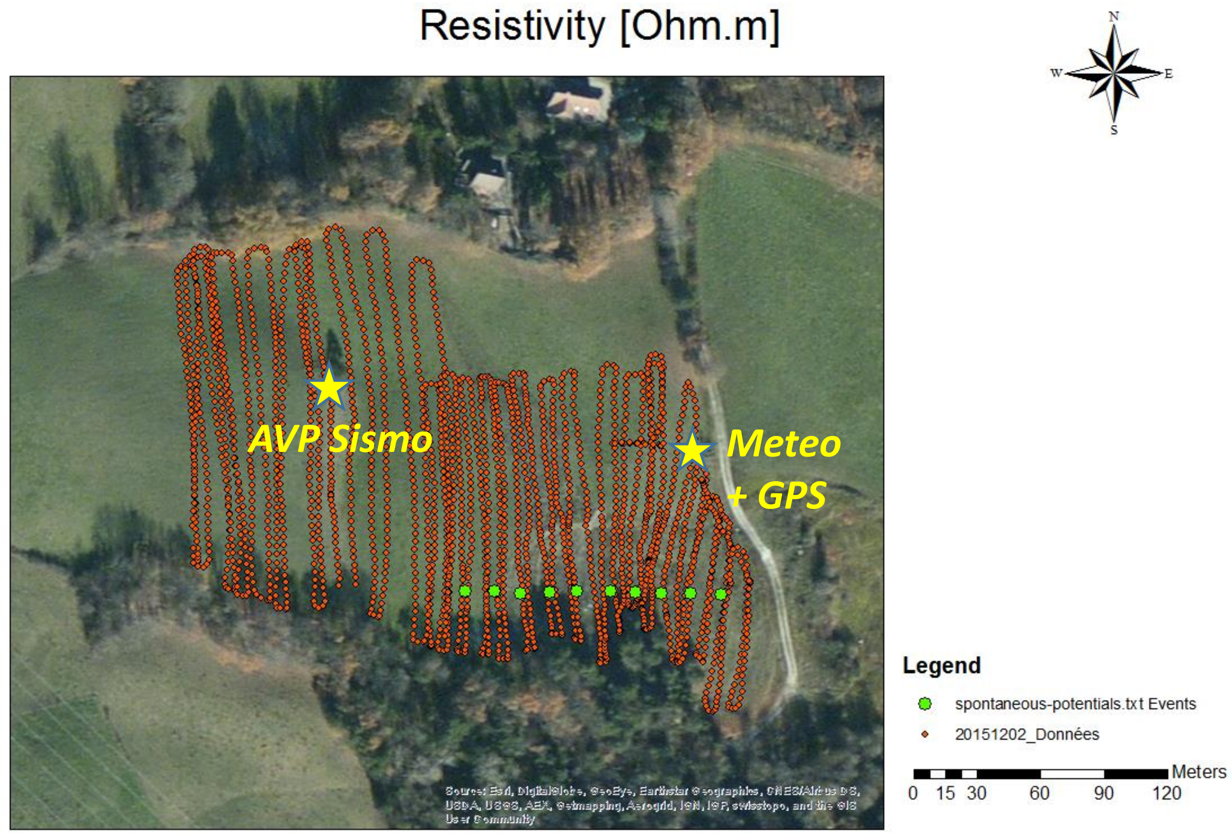

Figure 22 – EM31: GPS coordinates.
GPS coordinates (red dots) recorded every 2 s in the "Combe du Mas d'Avignonet". The green dots are the spontaneous potentials coordinates. The yellow stars the seismic station AVP and the meteorological station AVP2.

The instrument gets measurements every 2 s. Therefore, we have 2558 values of resistivity that we interpolated in Matlab (*Figure 23 - 24*) and in ArcMap *(Figure 25)* getting the spatial distribution of the resistivity values not taking into account anomalous values due to anthropic devices (metallic).

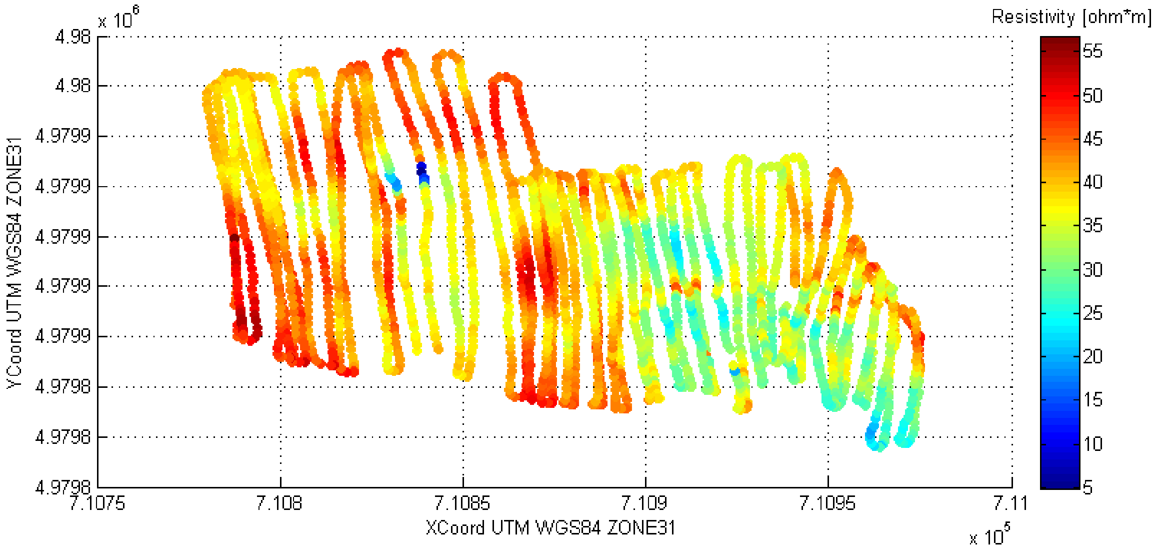

Figure 23 – EM31: Data points resistivity values (Matlab).
Resistivity values calculated by matlab software.

\

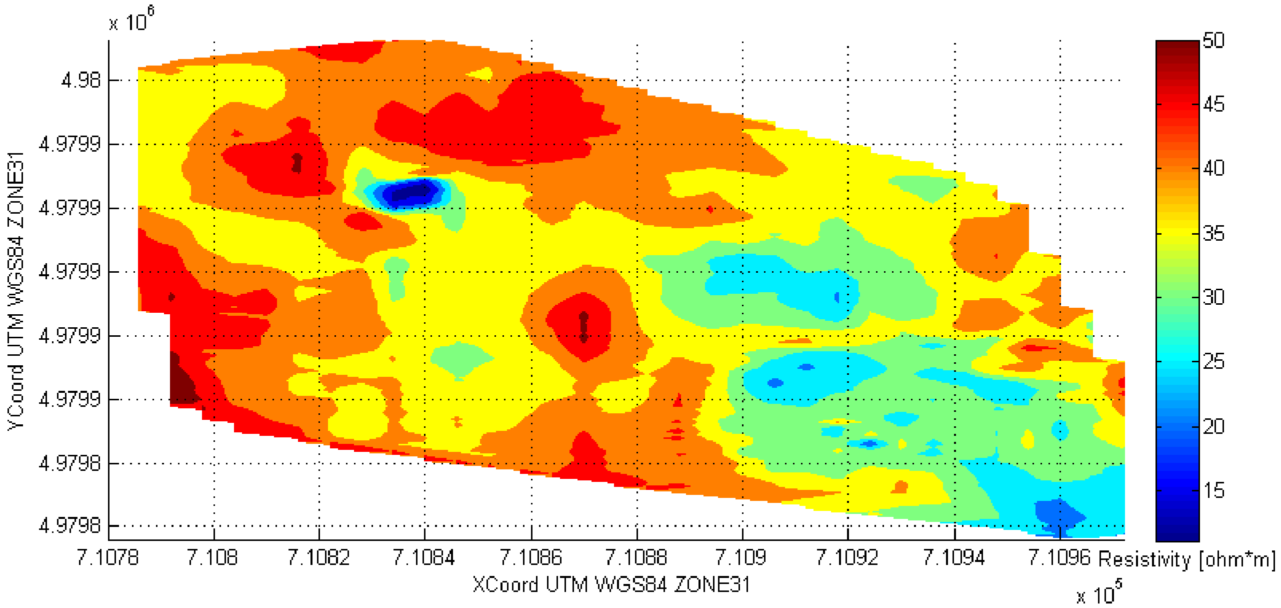

Figure 24 *– EM31: 2D Resistivity values interpolation (Matlab).*
It is important to define the grid of definition because in the figure 22 we see that the data are denser in Y axis rather than X axis because of survey direction that is parallel to the slope. Consequently, to avoid disequilibrium between the two directions, we use a larger X inter-distance.

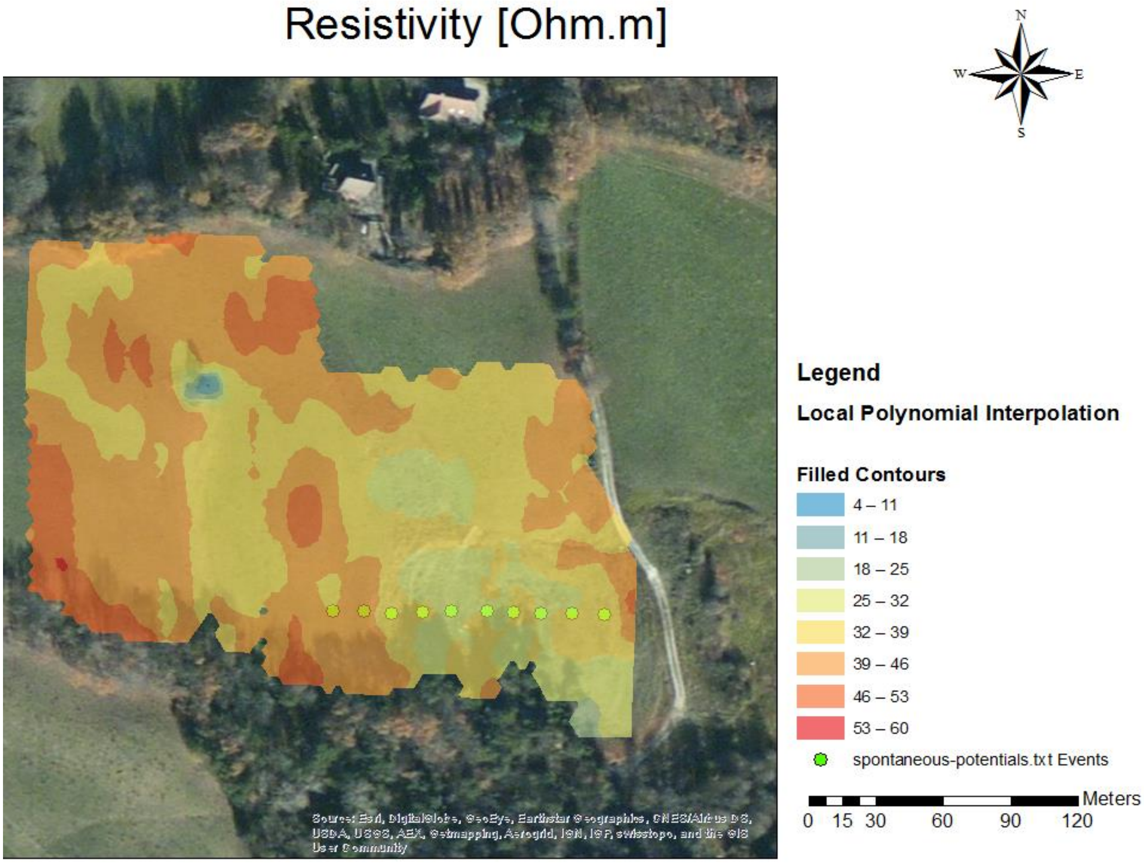

Figure 25 *– EM31: 2D Resistivity values interpolation (ArcGIS).*
Resistivity values obtained by local polynomial interpolation.

We see that the degraded area is less resistive than the surroundings as we expected. Particularly, we retrieved that the conductive lens has north-south extension. The resistivity values are between 18 and

\

25 Ω.m that are typical of clays (see table 1) probably influenced by water saturation. This qualitative survey gives us the average value of resistivity in the subsurface but it does not offer a definition of its spatial distribution. Therefore, in order to investigate in depth we will develop electrical resistivity tomography (ERT) leading to 3D resistivity imagery (paragraph 2.2.4.2.2).

2.2.4.2 Electrical campaign

In electric methods electrical sources energize the ground measuring its potential distribution by a couple of electrodes connected to a voltmeter. There are two methods inserting directly the current in the ground: equipotential lines method and resistivity method. The second one has been employed during this work in order to realise a 3D resistivity imagery.

2.2.4.2.1 Method's introduction

The geoelectrical method is carried out by recording the electrical potential arising from current input into the ground with the purpose of achieving information on the resistivity structure in the ground. The device consists of two electrodes' couples (*Figure 26 b*): a dipole AB (current electrodes) allowing the current flow (ammeter) and the dipole MN (potential electrodes) allowing the measure of the potential difference (Voltmeter). In a homogeneous and isotropic medium the electric current emitted by a single source electrode would flow radially in every direction (*Figure 26 a*) while with both a current source and a current sink, the current flow lines and the equipotential surfaces become more complex (*Figure 26 b*). Geoelectrical data are then commonly expressed in term of resistivity.

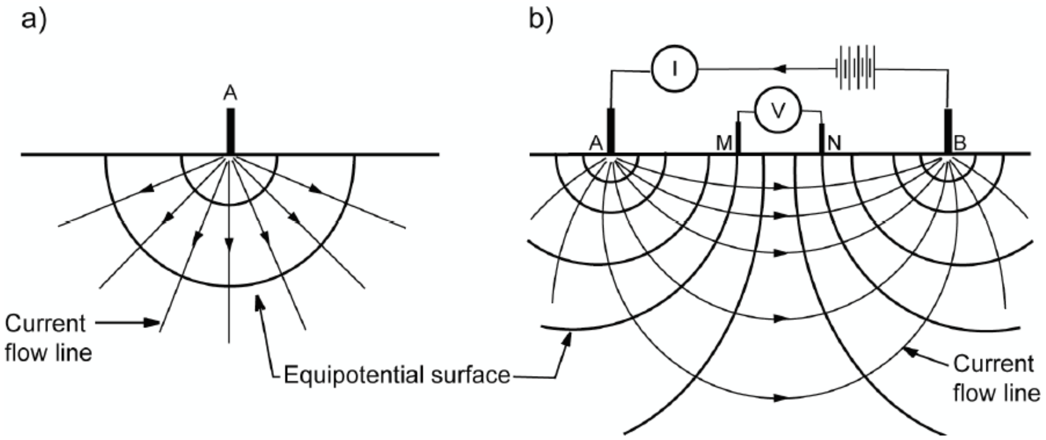

Figure 26 *– ERT: Physical principle.*
Simplified current flow lines and equipotential surface arising from a) single source and b) electrodes' couple. Figure taken from https://www.liag-hannover.de/fileadmin/user_upload/dokumente/Grundwassersysteme/BURVAL/buch/077-088.pdf

The resistivity ρ of a material is a measure of how well the materials retards the flow of electrical current. The following relationship is described by the Ohm's law:

$$V = I\,R \qquad \textbf{(2.4)}$$

Where V is the voltage in Volts, R is the resistance in Ohms and I is the current flowing in the circuit expressed in Amps. Resistivity depends also on geometrical properties K:

$$\rho = K \cdot \frac{V}{I} \qquad \textbf{(2.5)}$$

\

Where ρ is the resistivity, K the geometrical factor, V the potential difference and I the current flow. The geometrical factor K depends on the position of the four electrodes and particularly their inter-distance. In particular:

$$K = 2\pi * \left(\frac{1}{|r_A - r_M|} - \frac{1}{|r_A - r_N|} - \frac{1}{|r_B - r_M|} + \frac{1}{|r_B - r_N|}\right) \tag{2.6}$$

Where r_A, r_B, r_M, r_N are the positions of the 4 electrodes.

The resistivity ρ obtained in case of a homogeneous and isotropic medium, remains constant even if the distances between the electrodes are changed. But generally, the medium is not homogeneous and the physical quantity is the apparent resistivity ρ_{app} considering the average resistivity of a ground volume in which the current flows.

The resistivity varies a lot among the different geologic materials (see table) and it depends mainly upon the amount of groundwater present in the subsurface. Particularly, it is related to the amount of dissolved salts, the presence of contaminants but also to permeability and porosity of the medium. Conduction refers to the flow of electricity and in the rocks this occurs in two ways: electronic in metallic ores with electrons migrations or electrolytic/ionic involving cations and anions' motion.

Porous, water-bearing rocks and sediments may be ionic conductors. Their resistivity is roughly equal to the resistivity of the pore fluid divided by the fractional porosity. This relationship is expressed by the empirical Archi's law:

$$\rho = a \cdot \rho_w \cdot \varphi^{-m} \tag{2.7}$$

Where ρ the resistivity of a saturated porous medium, φ is the fractional porosity, ρ_w is the pore fluid resistivity and a, m are empirical quantities determined by the geometry of the pores.

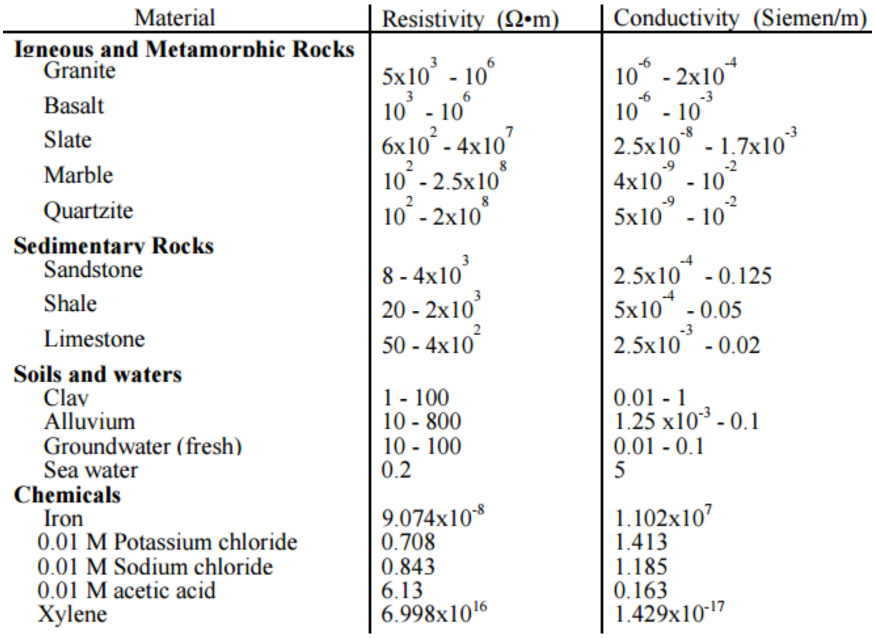

Material	Resistivity (Ω•m)	Conductivity (Siemen/m)
Igneous and Metamorphic Rocks		
Granite	$5x10^{3} - 10^{6}$	$10^{-6} - 2x10^{-4}$
Basalt	$10^{3} - 10^{6}$	$10^{-6} - 10^{-3}$
Slate	$6x10^{2} - 4x10^{7}$	$2.5x10^{-8} - 1.7x10^{-3}$
Marble	$10^{2} - 2.5x10^{8}$	$4x10^{-9} - 10^{-2}$
Quartzite	$10^{2} - 2x10^{8}$	$5x10^{-9} - 10^{-2}$
Sedimentary Rocks		
Sandstone	$8 - 4x10^{3}$	$2.5x10^{-4} - 0.125$
Shale	$20 - 2x10^{3}$	$5x10^{-4} - 0.05$
Limestone	$50 - 4x10^{2}$	$2.5x10^{-3} - 0.02$
Soils and waters		
Clay	1 - 100	0.01 - 1
Alluvium	10 - 800	$1.25\ x10^{-3} - 0.1$
Groundwater (fresh)	10 - 100	0.01 - 0.1
Sea water	0.2	5
Chemicals		
Iron	$9.074x10^{-8}$	$1.102x10^{7}$
0.01 M Potassium chloride	0.708	1.413
0.01 M Sodium chloride	0.843	1.185
0.01 M acetic acid	6.13	0.163
Xylene	$6.998x10^{16}$	$1.429x10^{-17}$

Table 1 – *Resistivity and Conductivity of some common rocks, minerals and chemicals.*
(http://www.geo.mtu.edu/~ctyoung/LOKENOTE.PDF)

\

The measurements are performed moving the four electrodes in a particular configuration conditioning the measure's resolution. Some of the most common electrode arrays are Wenner, Schlumberger, pole-pole, pole-dipole and dipole-dipole array (*Figure 27*).

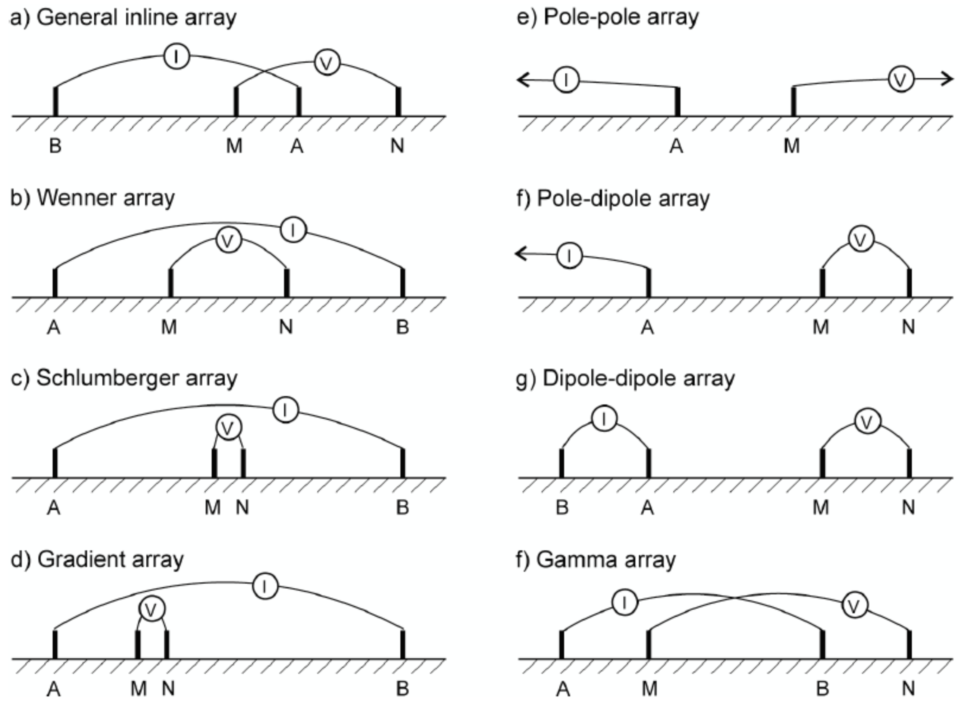
a) General inline array
b) Wenner array
c) Schlumberger array
d) Gradient array
e) Pole-pole array
f) Pole-dipole array
g) Dipole-dipole array
f) Gamma array

Figure 27 – ERT: Possible arrays configurations.
AB are the current electrodes, MN the potential. https://www.liag-hannover.de/fileadmin/user_upload/dokumente/Grundwassersysteme/BURVAL/buch/077-088.pdf

To sum up Direct-Current Resistivity Survey are divided into:

- Electrical Profiling Configurations (EPC)
    - DC Resistivity Survey (Dipole – Dipole array)
    - DC Resistivity Survey (Pole – Dipole array)
- Vertical Electrical Sounding Configurations (VES)
    - DC Resistivity Survey (Schlumber array)
    - DC Resistivity Survey (Wenner array)

Electrical profiling aims to trace lateral variations with apparent resistivity structure of the subsurface. Traditionally, electrical profiling provides qualitative information of relative apparent resistivity values in order to detect anomalous geological features. Vertical Electrical Sounding instead, provides information regarding the change in apparent resistivity with depth. In this work, we use Dipole-Dipole and Wenner array configuration aiming to realise an Electrical Resistivity Tomography. In Dipole-Dipole the inter-distance between the current electrodes is constant as well as the potential electrodes. In Wenner the inter-distance is instead always constant.

\

2.2.4.2.2 Avignonet’s case study

Electrical surveys improved their performances with the development of the informatics tools (Bièvre, 2010) leading to resistivity imagery ERT (Electrical Resistivity Tomography) in 2D or in 3D. Geolectrical imaging technique are now widely used in environmental and engineering problems producing spatial models of subsurface resistivity distributions (Wilkinson et al., 2010). In order to get an Electrical Resistivity Tomography it is necessary an inversion phase of the data acquired. The inversion of the datasets is carried out with RES2DINV for 2D profiles and with RES3DINV with 3D tomography using a 3D smoothness-constrained nonlinear least-squares algorithm (Wilkinson et al., 2010). Particularly, the inversion phase computes a model that satisfies the observed data (Wilkinson et al., 2010).

Considering Avignonet’s landslide case study electrical surveys were performed in the most active area of the landslide (*Figure 6*) by Bièvre (2008-2009) in order to assess the role of fissures in water infiltration within a clay landslide. They applied resistivity method with ERT profiles EP1 and EP2 oriented E-W along the slope (*Figure 28)*. The acquisitions were performed in different time lapses between 2008 and 2009 in order to see the water propagation function of time and the appearance of fissures.

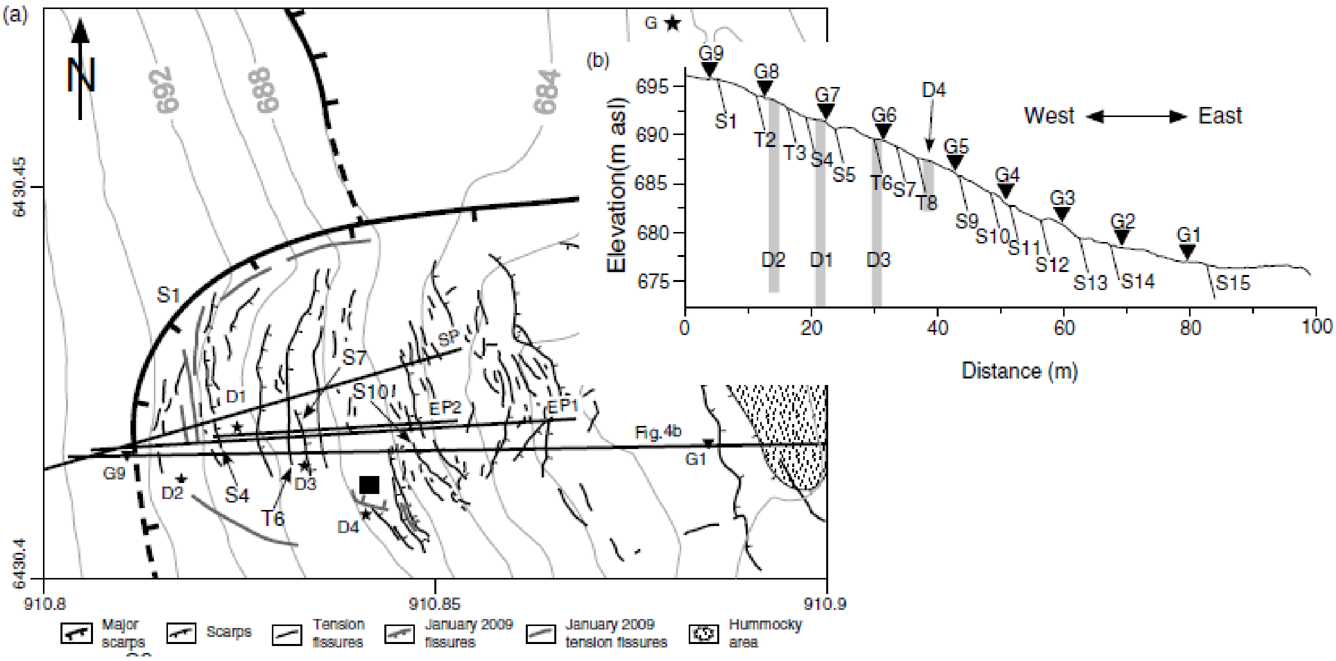

Figure 28 – Geomorphology in “Combe du Mas d’Avignonet”.
Geomorphological map of the area of interest with location of the geophysical measurements. ***a****) Topographic mapping with location of scarps, tension fissures and hummocky areas. G: GPS reference station and meteorological station (AVP2_meteo_gps in fig. 6). SP: seismic profile; EP1 and EP2: electrical resistivity profile; D1 to D4: boreholes. S1 to S15: scarps (location in Figure 4b); T6: tension fissure (location in Figure 4b). Black-filled rectangle corresponds to VWC probes location.* ***b****) E-W cross-section of the site along GPS points (location in Figure a) with position of main scarps (S) and tension fissures (T). G1 to G9: GPS points. This figure is taken from Bièvre et. al, (2010). Note the correspondence with fig. 6.*

\

The two profiles were performed using 64 electrodes with Wenner configuration but different resolutions: EP1 with 64 electrodes 1 m apart and EP2 with 64 electrodes 0.5 m apart (better resolution). Their results (*Figure 29*) show that the blocky clays have low resistivity values (15-25 Ω.m) overcome by higher resistivity layers (up to 100 Ω.m). The most interesting part corresponds to the central lens with low resistivity (below 15 Ω.m) that is better observable in the EP2 profile where we can define its extension. This conductive lens is above the water table level so it could be interpreted by a higher clay concentration or by higher water content in unsaturated clay.

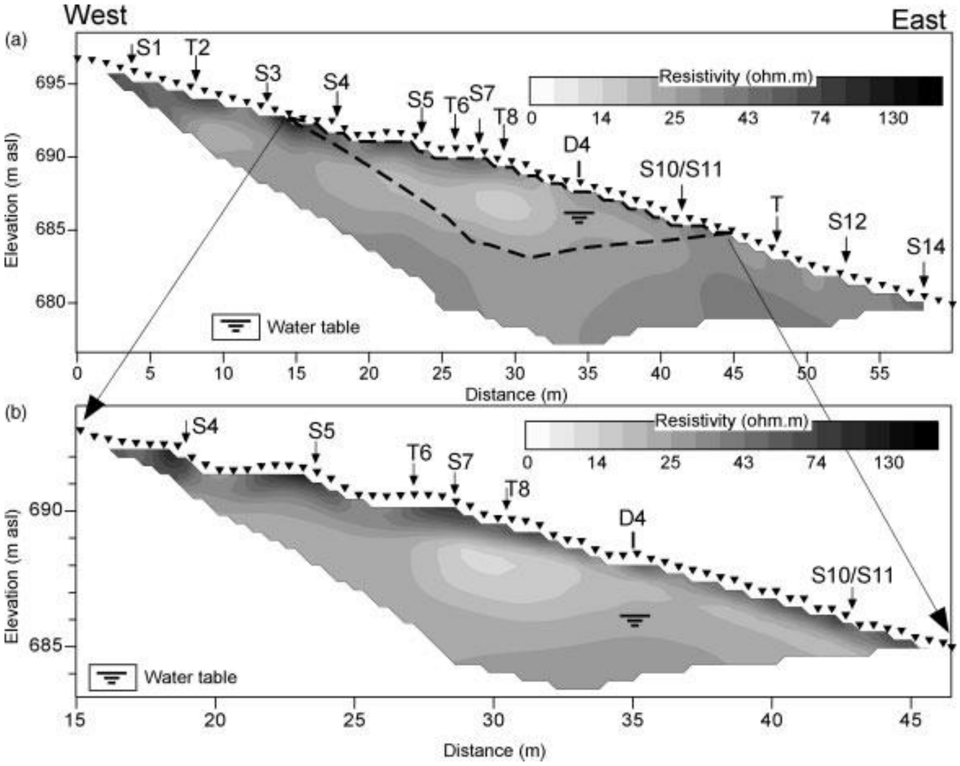

Figure 29 – ERT: profiles. a) EP1 b) EP2.
The filled triangle represent the 64 electrodes used; S1 to S15 are the scarps; T are the tension fissures while D the boreholes. It is interesting that in the more refine profile it is possible to define better the central lens. This figure is taken from Bièvre et al. (2011).

In order to know exactly what this conductive lens is, Direct Current (DC) Resistivity Surveys have been performed on 02-03-2016 in order to get 3D Electrical Resistivity Tomography. We wanted to observe the spatial distribution of the anomaly in the subsurface above the water table like the previous investigations (Bièvre et al., 2011). The survey strategy consisted in a rectangular grid of 128 electrodes (16 in E-W direction and 8 N-S direction) with an inter-distance of 2 m. The 16 x 8 electrodes array covers up a 30 x 14 m area located in correspondence of the previous 2D profiles EP1 and EP2. Moreover the grid's localisation depends on EM31 results (described in the 2.2.3.1 paragraph). The surface resistivity is obtained averaging the resistivity values of the first 4-5 metres. However ERT is a quantitative method because of dependence of resistivity respect to depth. In *Figure 30* EM31 results are overlapped to the electrodes disposition adopted in ERT. The equipment consisted of 128 electrodes organised in 8 parallel lines of 16 electrodes with a grid distance of two meters. They are placed above the assumed conductive lens. We can distinguish the conductive lens along the N-S direction in parallel to the slope. The station

\

was set up injecting a 200 mA in the ground with the Electrical Profiling configuration (Dipole-Dipole) and with the Vertical Electrical Survey configuration (Wenner).

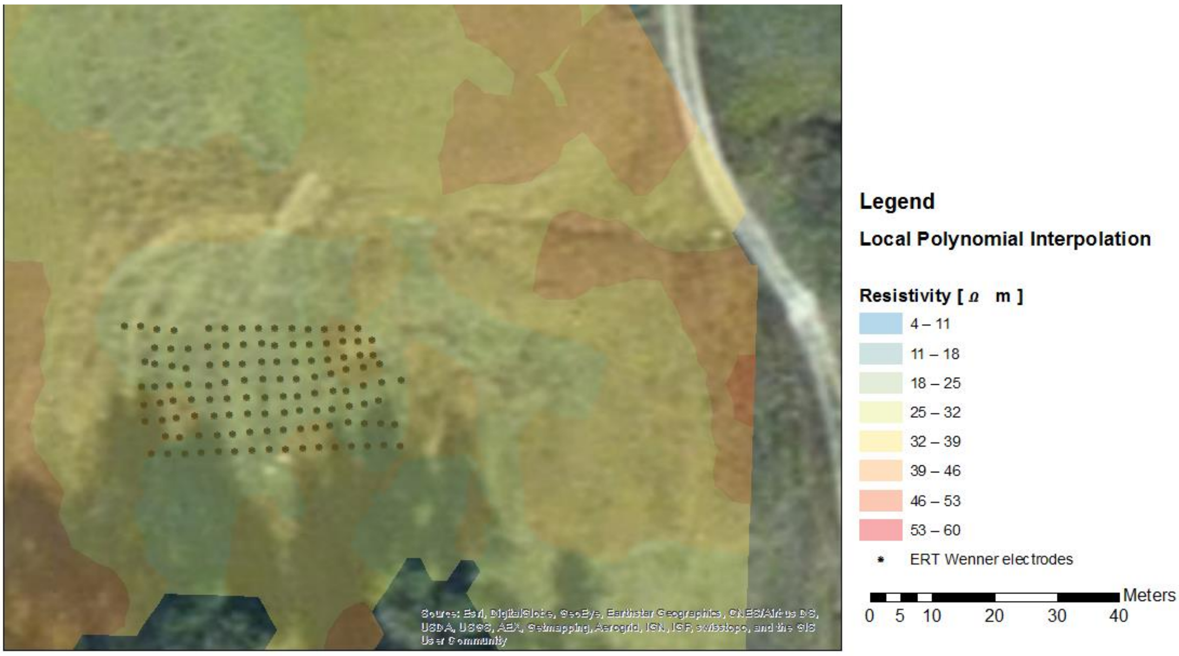

Figure 30 *– ERT: Array disposition.*

EM31 mapping in Wenner configuration array. The rectangular grid has a non-uniform shape and it is located above a conductive lens (18-25 Ω.m). The area has a degraded morphology with scarps and tension fissures. During the acquisition some electrodes did not work correctly;

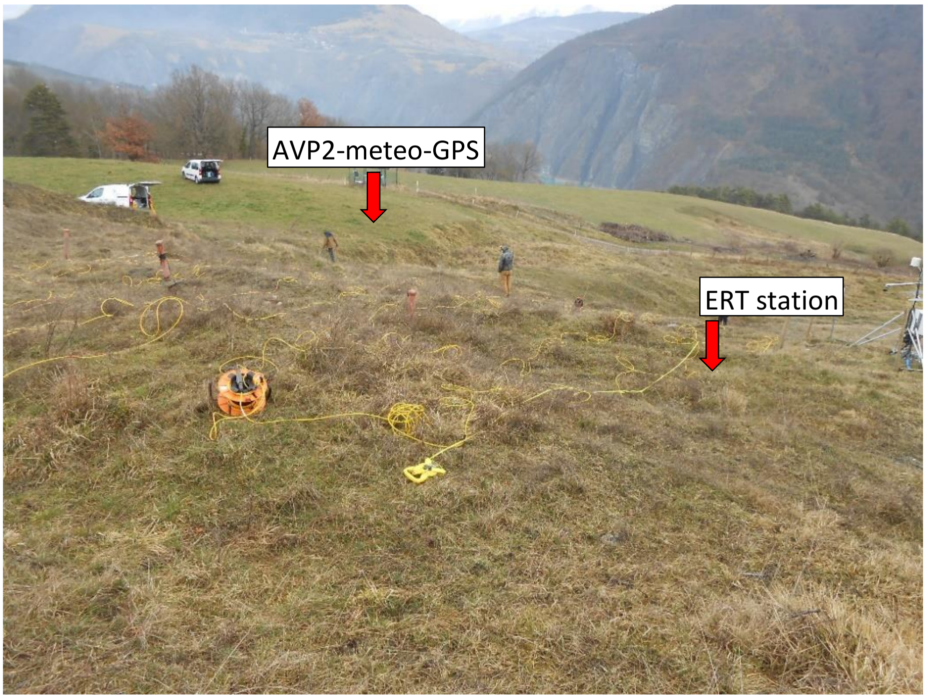

Figure 31 *– ERT: Array picture.*

Picture taken during the electrical survey (02-03-2016). It is possible to observe the morphology of the degraded area respect to the outside region.

\

2.2.4.2.3 Data Processing

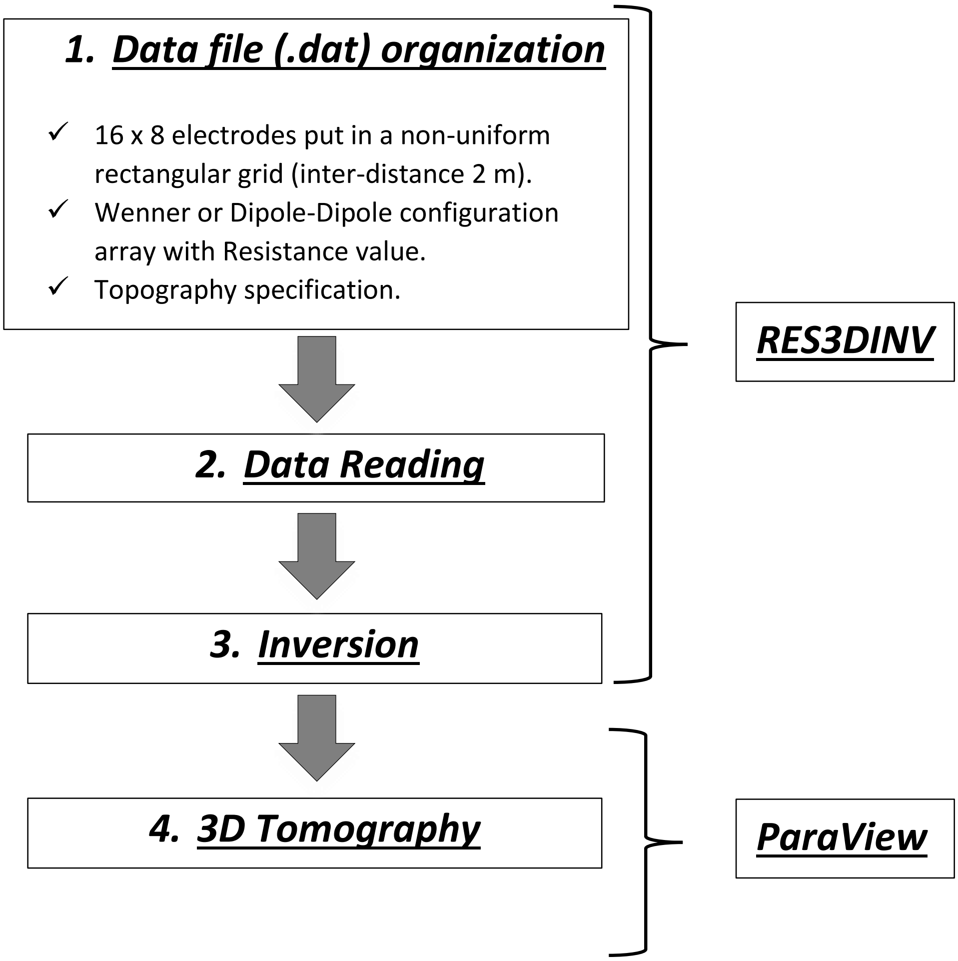

Figure 32 – ERT: Data processing (Flow Chart).
Data processing represented in a flow chart.

In **Phase 1**, it is necessary to prepare the .dat file in order to read it in RES3DINV. Particularly, we specify the grid of electrodes (non-uniform rectangular grid), the array configuration (Wenner or Dipole-Dipole) and finally the electrodes' topography. The .dat file is then read in RES3DINV and the inversion is carried out (**Phase 2**). In order to represent the 3D profiles it is necessary to export the inversion results in .vtk software acceptable by ParaView visualization software.

2.2.4.2.4 Results

The inversion was carried out and the results are represented here below (*Figure 33*) in 7 longitudinal 2D sections in the XZ plane. It is possible to retrieve in all the sections the conductive lens at 2 m depth (roughly in the midpoint of the x axis). These results confirm the previous electrical surveys (Bièvre, 2008-2009). Particularly, Bièvre wanted to define geometrically this anomaly in order to understand its real reason. Observing the 2D sections it is possible to see that the conductive lens is not very localized but extended in N-S direction. The anomaly could be better described by the 3D tomography exporting the inversion results in ParaView software (*Figure 34*) and representing in the range 1-100 Ω.m. These considerations are especially evident for Wenner configuration results that we decided to present here below:

\

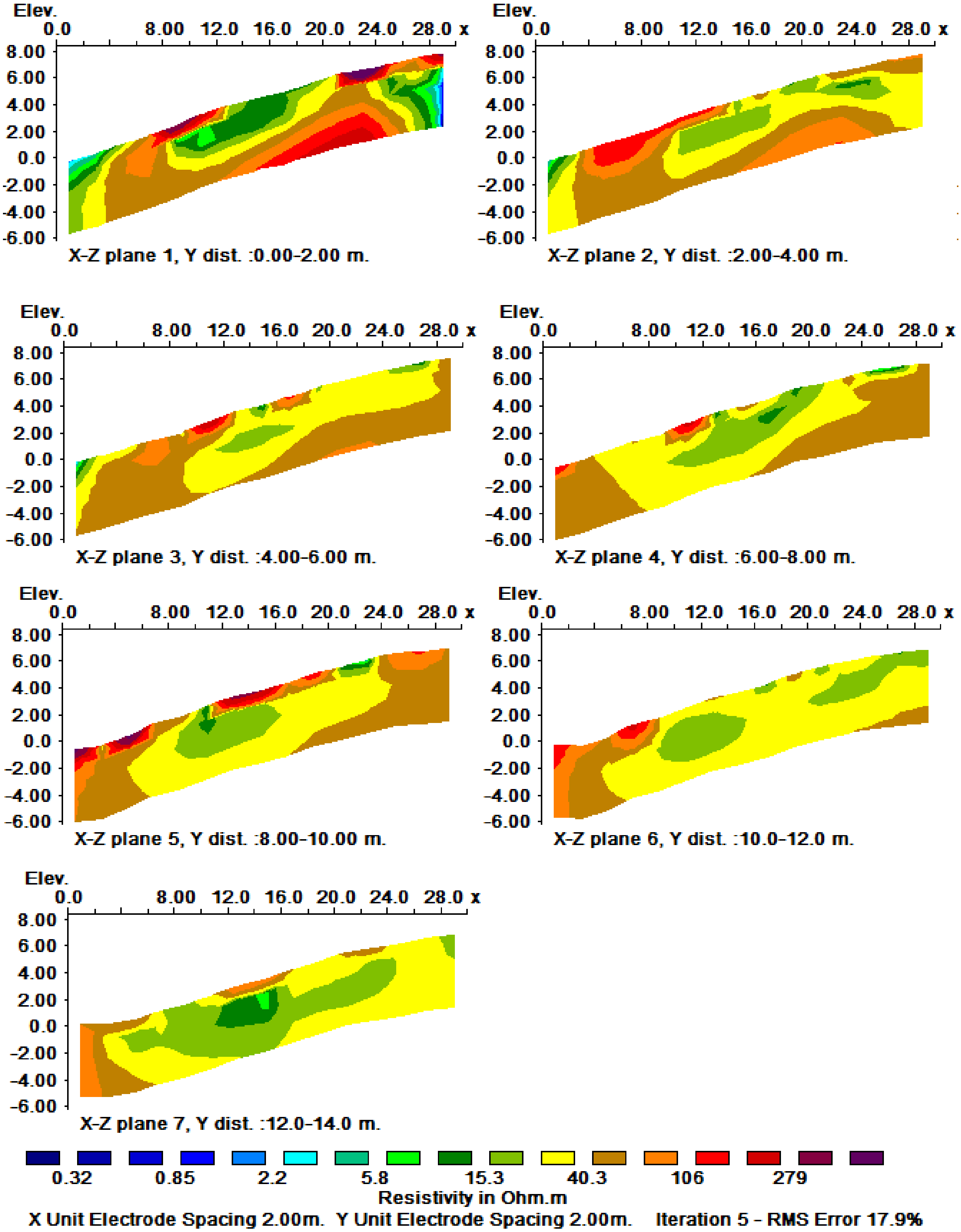

Figure 33 – *ERT: Sections profiles.*

X-Z sections realised every 2 m with Wenner configuration. The electrodes disposition has been chosen considering as electrode number 1 the North-East electrode and the sequence follows the x axis (West direction) and y axis (South direction) like a snake.

\

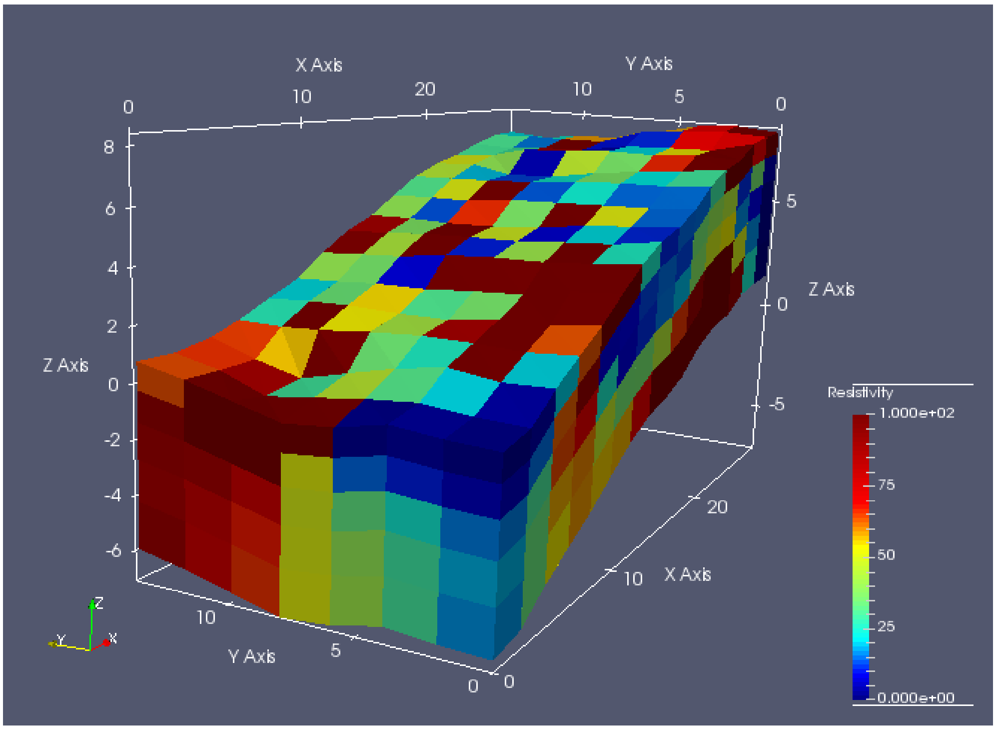

Figure 34 – *ERT: 3D Tomography.*
Electrical Resistivity Tomography got by Wenner configuration. The relative coordinates are expressed respect to the North-East electrode of the non uniform rectangular grid.

In order to define N-S distribution we isolated resistivity values in a range of values. *Figure 35* presents the threshold 15-22 *Ω*.m. It is therefore possible to observe a conductive structure extended perpendicular to the slope.

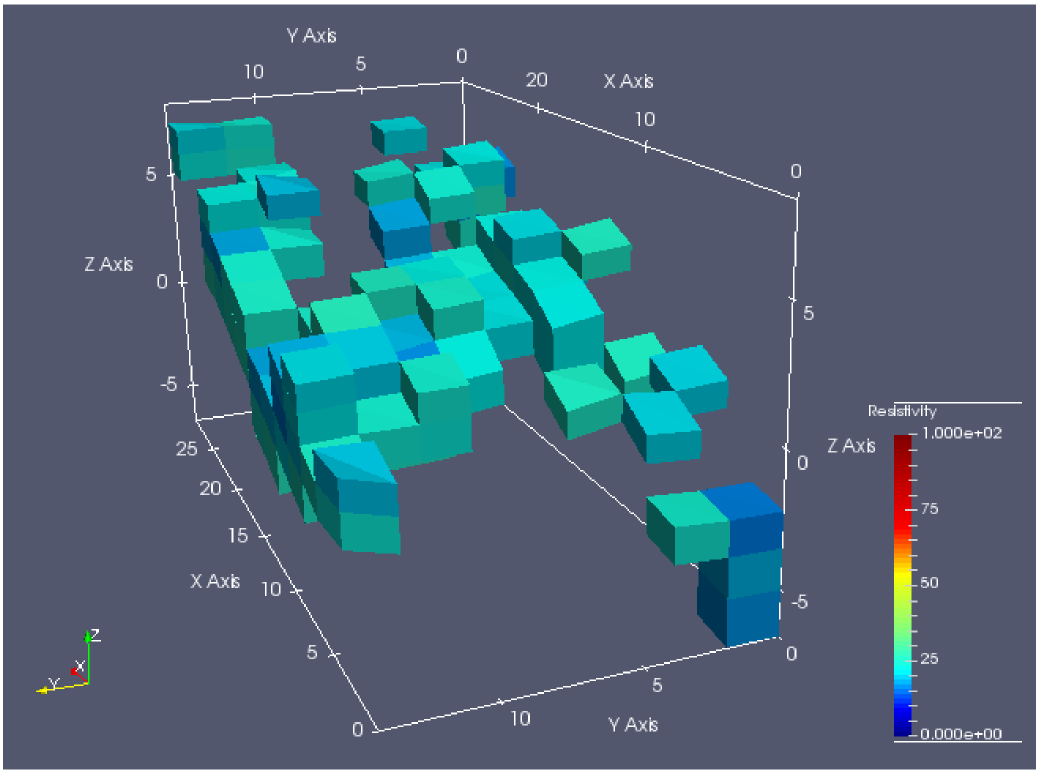

Figure 35 – ERT: Conductive lens extension.
The conductive lens (15-22 *Ω*.m) perpendicular to slope.

\

Bièvre (2010) assumed that this conductive anomaly was due to water circulation or to a clay-rich soil layer. In order to define geometrically this structure we performed ERT finding that it is extended in North-South direction.

In order to define exactly this structure, it could be useful to realize an IP tomography or realize boreholes. The second hypothesis consists of two boreholes realised in two different media (taking into consideration the ERT tomography). This could be advantageous because the layer is not so deep (we are above the water table level).

\

3 Seismology

This chapter represents the core of this work because it deals with the cross correlation of ambient seismic noise method. Particularly, after an introduction illustrating the application and the attainments of the method, the physical understanding of the method are presented. Then, the following part is about the method's application to Avignonet case study with the conventional approach (cross correlation of a couple of stations) and the empirical approach (one station monitoring) with a final section about results' interpretation.

3.1 Introduction

The daily cross correlation of ambient seismic noise, whose principle will be discussed later, proved its feasibility in seismology to monitor continuous changes within volcanoes and active faults. This technique proved a great potential to study the Earth interior at different scales in space and time. There are mainly three main types of seismological applications related to noise correlations: (1) studies of spatio-temporal distribution of seismic noise sources, (2) noise-based seismic imaging, and (3) noise-based seismic monitoring.

The third application is really important to our monitoring purpose because the seismic velocity variations are retrieved continuously. The principle is, as mentioned before, to apply a differential measurement to correlation functions, considered as virtual seismograms. Temporal changes could explain both earthquake activities (*Figure 36*) and hydrogeology (*Figure 37*).

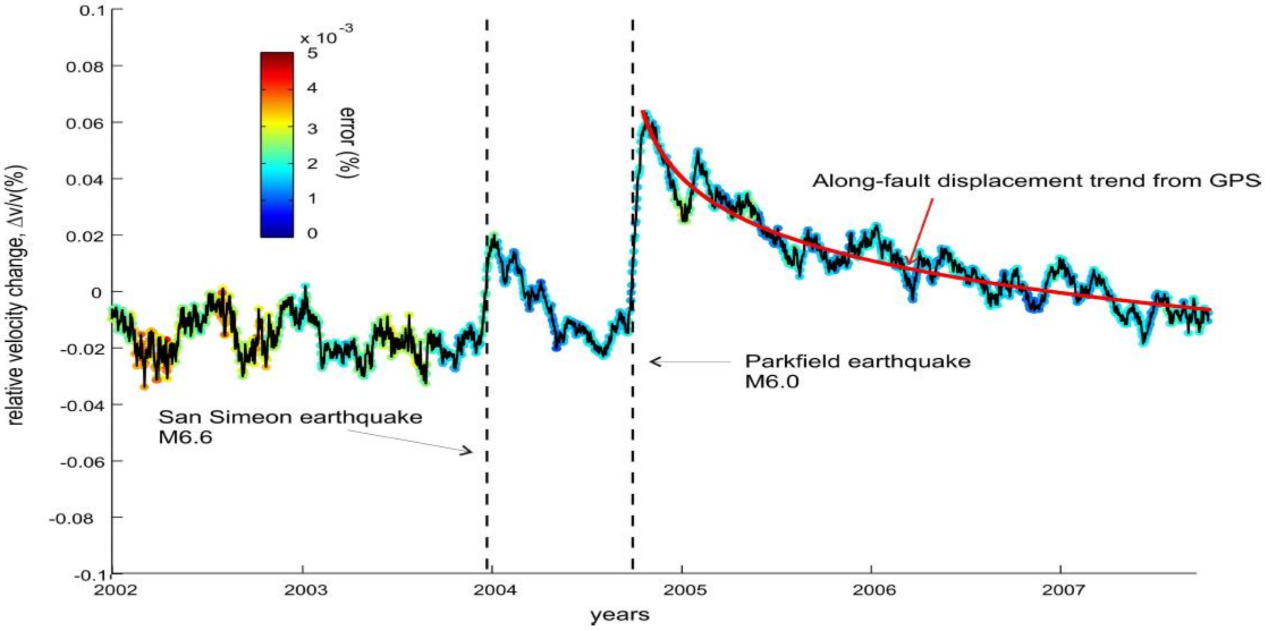

Figure 36 *- Relative seismic velocity changes (Parkfield case study).*
Relative seismic velocity changes during 6 years measured from continuous noise correlations in Parkfield. The dashed lines indicated two major earthquakes: the San Simeon event that occurred 80 km from Parkfield and the local Parkfield event (from Brenguier et al. 2008b)

\

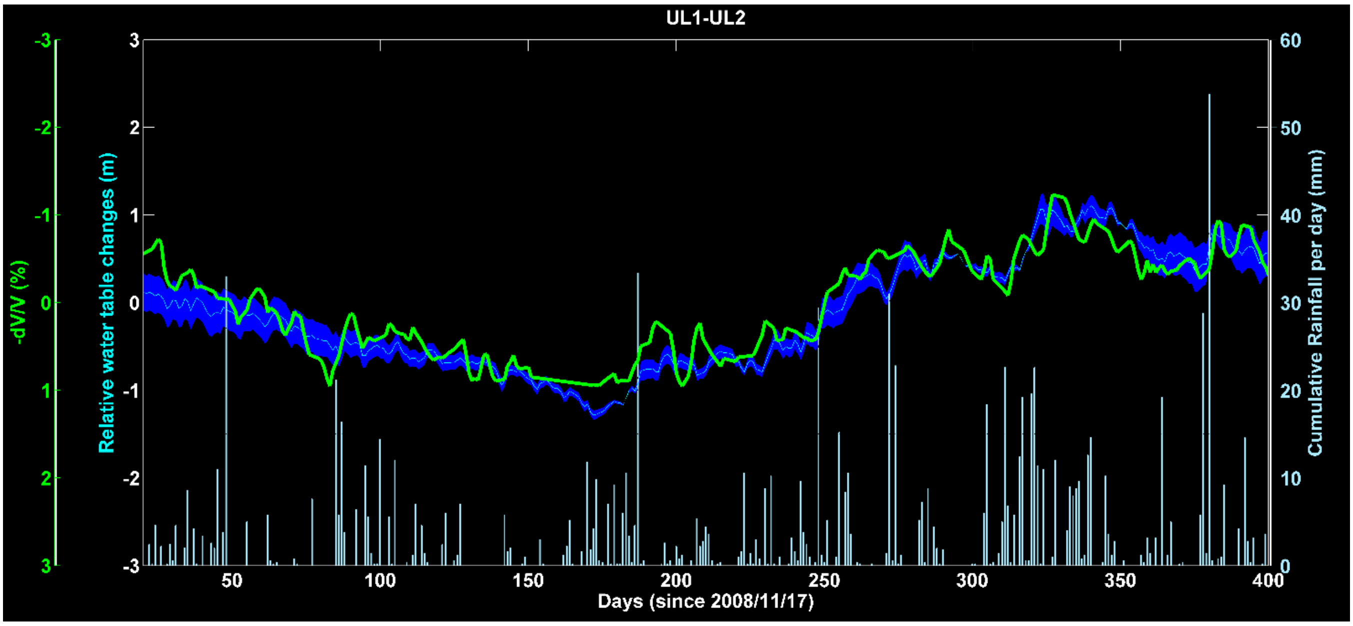

Figure 37 - Relative seismic velocity changes (Utiku case study).
Relative seismic velocity changes during 400 days measured from continuous noise correlations in Utiku of the UL1-UL2 station pair. The blue line represents the water table changes and the green line the seismic velocity variation. Also the rainfalls per day are plotted.

3.2 Cross Correlation of Ambient Seismic Noise technique (principle)

The ambient noise represents the ground motion which is recorded in the absence of an identifiable source of seismic energy, such as an earthquake. The main cause of ambient seismic noise is the interaction of low frequency (< 1 Hz) oceanic surface waves with the Earth's crust (Ardhuin et al., 2011). Therefore, we distinguish microseisms (low frequency waves < 1 Hz) due to natural causes (mainly ocean waves (0.1 – 0.3 Hz)) and microtremors (high frequency waves > 1 Hz) mainly produced by human activities (traffic, outside activities etc.…) but also by natural sources such as rivers and wind (about 1 Hz). We can infer that microseisms are more related to faraway causes rather than microtremors that are related to regional sources and that we mostly exploit in our work. These considerations tell us that the seismic sources of ambient noise are everywhere and consequently we adopt the assumption to be in a diffuse field (Wapenaar, 2004).

Ambient seismic noise signal is mainly dominated by surface waves (Love and Rayleigh) but also by body waves (P and S waves). Seismic waves in earth materials are subject to attenuation and dispersion in a broad range of frequencies. Attenuation is related to the exponential decay of wave amplitude with distance; dispersion is a variation of propagation velocity with frequency (http://www.geos.ed.ac.uk/homes/imain/Attenuation.pdf). These two important properties could be caused by a variety of physical phenomena that could be divided into elastic processes (scattering attenuation and geometric dispersion), where the total energy of the wavefield is conserved, and inelastic dissipation, where the energy is converted into heat. Particularly the presence of fluid in soil's pores (related to water table level and fluid saturation zone) could effectively cause dispersion of the seismic waves. Each frequency generates a wavefield with a different sensitivity to Vs changes and amplitude of displacement as a function of depth. In the broadband there are specific bandwidths more sensitive to seismic velocity changes. They correspond to discontinuities in physical properties like the

\

presence of water table or fluid saturation. Cross correlation of ambient seismic noise leads to Rayleigh waves' ground response allowing a temporal monitoring of seismic velocity variations.

Considering a seismic signal recorded at two stations R1 and R2 (*Figure 38*), the cross correlation consists on measuring the similarity of two signals of two waveforms in time by identifying the **time lag** (τ), the amount which one of the signals is shifted relative to the other, at which they are most similar.

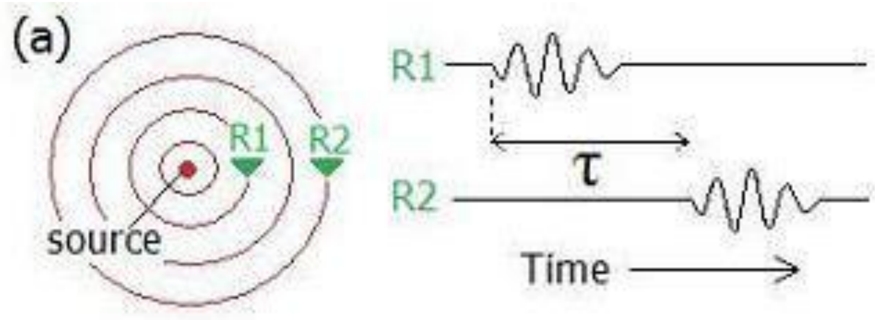

Figure 38 – *Ambient noise: physical understanding.*
a) understanding of cross correlation taking two stations R1 and R2 that register the signal generated by the source (red dot). The signals are almost identical but they are shifted by time lag t. Taken from http://volc_seis_commission.leeds.ac.uk/indexa63d.html?option=com_content&task=view&id=75&Itemid=29.

The cross-correlation of two signals **a** and **b**, $C_{a,b}$, is a function of time lag, and is commonly defined as:

$$C_{a,b}(\tau) = \int u(t,a) \times u(t-\tau,b)dt \qquad \textbf{(3.1)}$$

Where the integration is performed on the length of records and u is the amplitude of a signal as a function of time. The operation is a convolution between the two signals.

$C_{a,b}$ (noise cross correlation function) is maximum when the sum of the products $u(t,a) \times u(t-\tau,b)dt$ is at a maximum, meaning that **a** and **b** are most similar when **b** is shifted by that amount relative to **a**. An auto-correlation (cross-correlation of a signal with itself) therefore has its maximum at a time lag of zero. The two signals are overlapped moving the first on the second obtaining the function $C_{a,b}$ or CCF (Cross Correlation Function) that its maximum represents the time lag τ that is the time that the wave particle takes to move from R1 to R2 that is when the similarity is better.

The Cross Correlation is performed for positive and negative time lag and consequently the cross correlation functions have both positive and negative parts called causal and anti-causal parts. The symmetry of the cross correlation function is possible depending on the noise sources distribution (*Figure 39*).

\

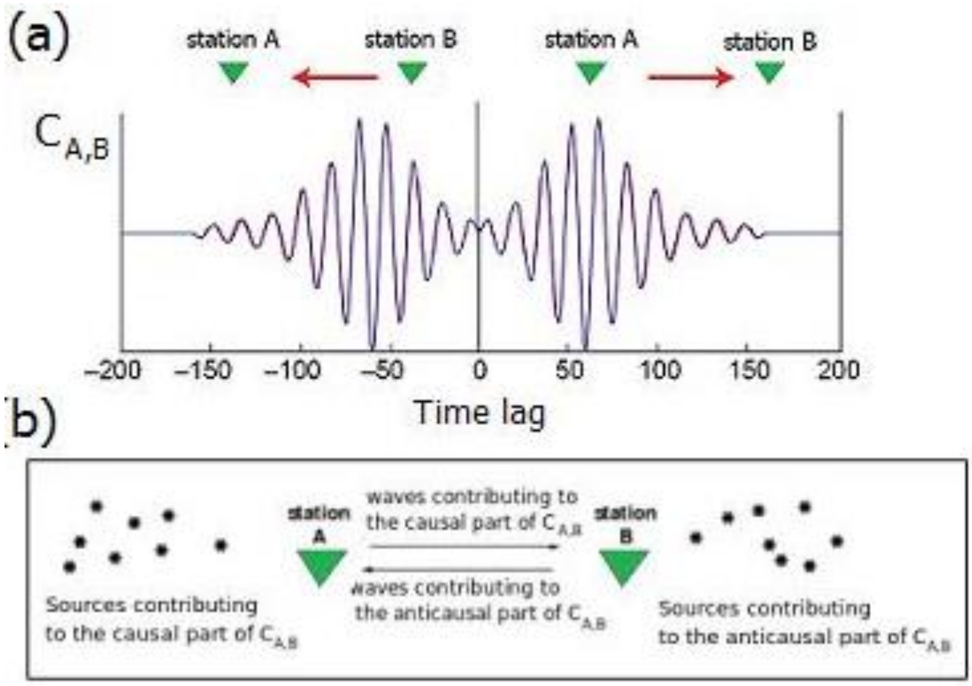

Figure 39 – *Cross correlation function and source distribution.* *http://volc_seis_commission.leeds.ac.uk/indexa63d.html?option=com_content&task=view&id=75&Itemid=29*

The output of cross correlation will be the noise cross correlation function that could lead to elastodynamic Green Functions (GF) that is the wave field that would be observed at one of these receiver positions if there was an impulsive source at the other (Wapenaar, 2004) (*Figure 40*).

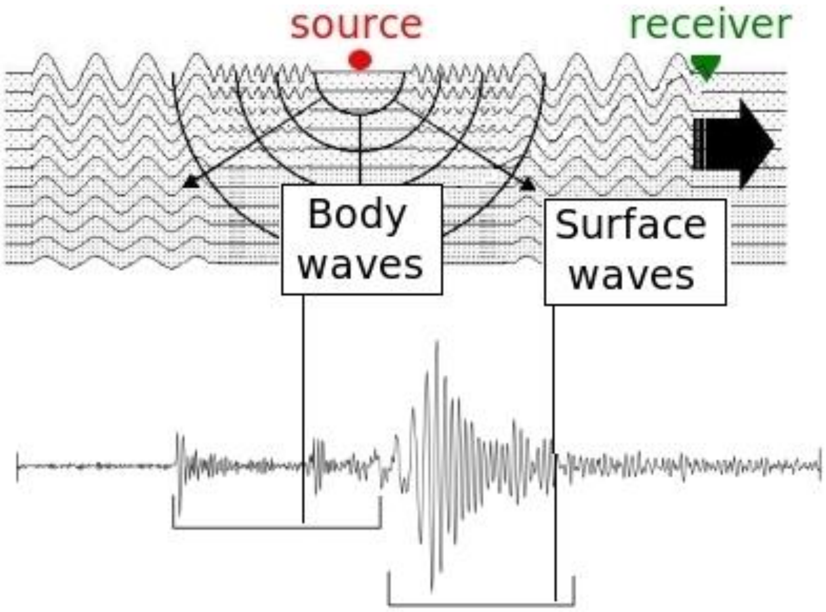

Figure 40 – *Ground physical model.*

The Greens Function represents the ground energy in response to a source that is the other station of the pair as the seismogram registered in the receiver. Taken from http://volc_seis_commission.leeds.ac.uk/indexa63d.html?option=com_content&task=view&id=75&Itemid=29.

\

If the noise sources distribution is isotropic then the correlation function (GF consequently) is symmetric. Asymmetry of the correlation function is a “measure” of the source distribution anisotropy. Therefore we can observe a stronger energy flux in one direction respect to the other (*Figure 41*) but it is not important for seismic velocity variations monitoring because the Greens Function retrieval is not required (Campillo and Paul, 2003). However the necessary assumption is that the noise sources are stable over time (Hadziioannou, 2011).

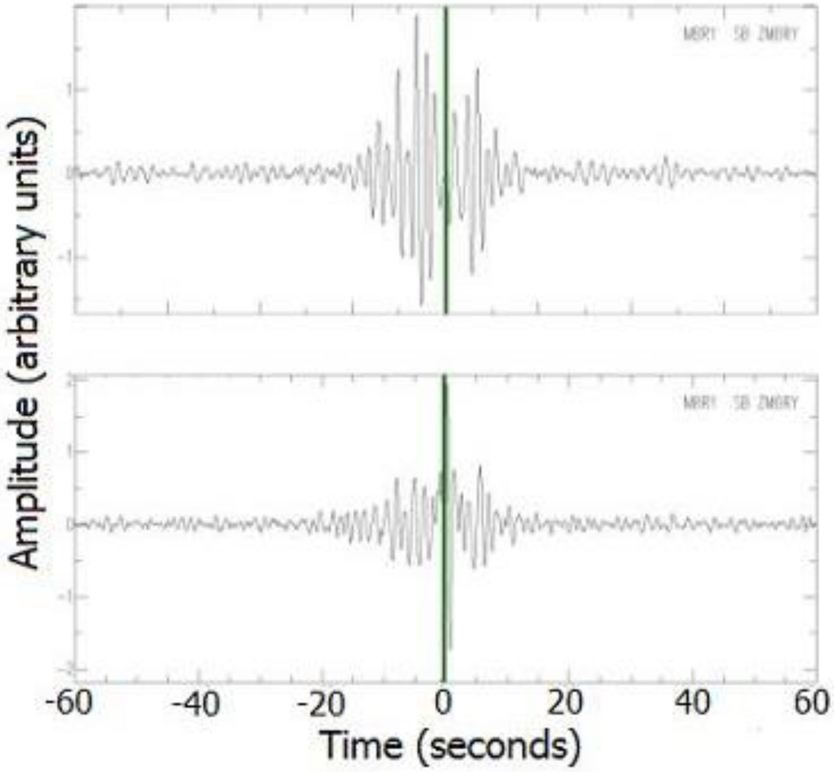

Figure 41 *– Daily noise cross-correlation example. (*[*http://volc_seis_commission.leeds.ac.uk/indexa63d.html?option=com_content&task=view&id=75&Itemid=29*](http://volc_seis_commission.leeds.ac.uk/indexa63d.html?option=com_content&task=view&id=75&Itemid=29)*). Note the asymmetry due to source anisotropy. In the upper part we can see more energy propagate to one direction respect to the other (left side).*

The station pair components’ signal records are considered on a 24 h basis averaging the anthropic noise sources (mostly due to traffic flows and human activities in the Sinard village) and they are cross correlate after bandpass filtering and spectral whitening (Shapiro et al, 2005; Stehly et al., 2006). These aspects will be further discuss in detail in the next chapter where we will analyse every single phase.

In order to investigate the first meters of subsurface mostly related to water table level variations, we have to retrieve the surface waves that are prevalent here as mentioned before speaking about the wave dispersion property. In particular the retrieval of Rayleigh waves, whose particle motion is retrograde elliptical (*Figure 42*) in the vertical radial plane, is possible by cross correlating the vertical components of the station pair. The property of these waves is that the amplitude decreases with depth and consequently low frequency waves investigate deeper than higher frequency waves that are closer to surface. Therefore for a specific depth there will be a specific wave field corresponding to a specific frequency band leading to water table variation characterisation.

\

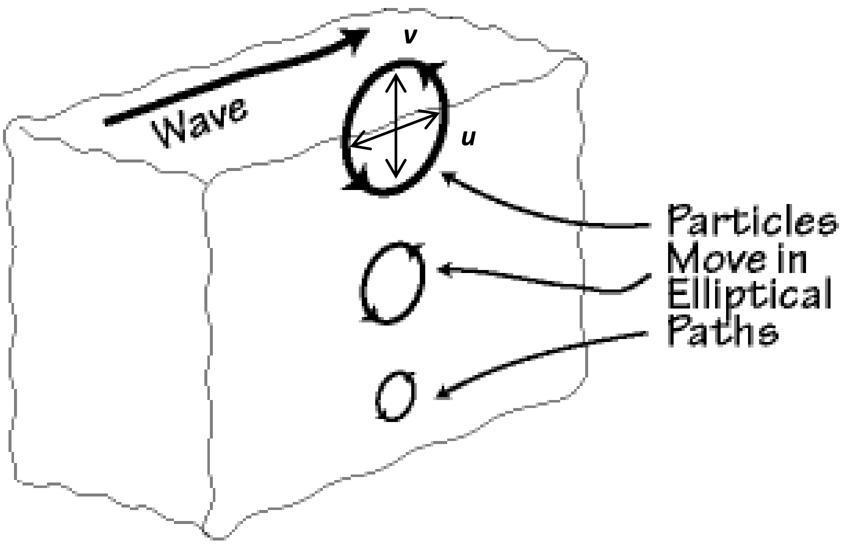

Figure 42 – Rayleigh waves dispersion with depth.
They have a retrograde elliptical motion and the amplitude of the displacement (u is the horizontal v the vertical) decreases with depth. Image taken and modified from http://eqseis.geosc.psu.edu/~cammon/HTML/Classes/IntroQuakes/Notes/waves_and_interior.html

Daily cross correlations are put in sequence in a correlogram where the x axis represents the time lag and in y axis the period with all the daily correlations expressed in amplitude of the phases (*Figure 43*).

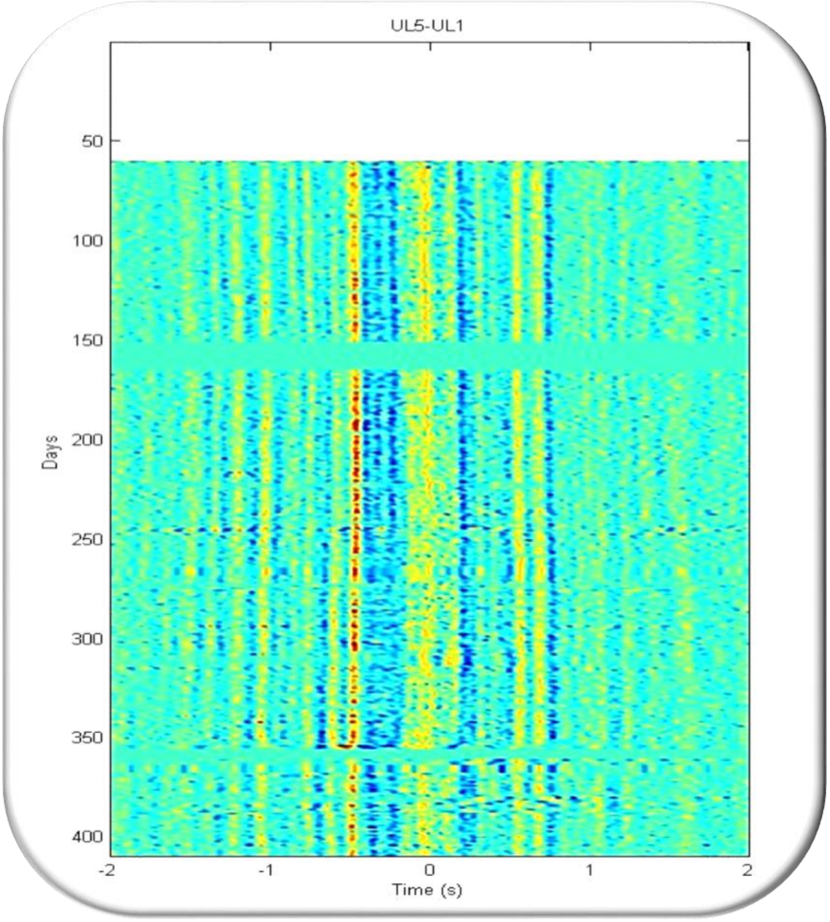

Figure 43 – Broadband correlogram (Utiku case study).
Broadband correlogram (30 s – 40 Hz) resulting from the cross correlation of the vertical components of the stations' couple UL5 – UL1 in Utiku clayey landslide. We can see the stability of arrivals (e.g. at time=-

\

0.4 s) confirming the temporal stability of the noise sources, and the asymmetry of the correlogram due to the anisotropy of the sources. The light blue horizontal bands are missing data. Image taken from Garambois S., Voisin C. (2016).

The computation of seismic velocity variation follows the procedure deployed for Utiku landslide in New Zealand (Voisin C., Garambois S. et al., 2016) and it consists on using stretching technique that is particularly appropriate for localised velocity variations rather than doublet technique (Sens-Schoenfelder and Wegler, 2006). In order to perform it, it is necessary to choose a time lapse window to compute velocity variations. This choice could be subjective because of the quality of continuity of the different seismic phases or the late arrival time (Voisin C., Garambois S., 2016). However it is possible to avoid this problem choosing a fixed window and moving it on the x-axis as many times as needed to giving less importance to this subjective criterion.

For each window the stretching technique (*Figure 44*) is performed computing the velocity of each windows with respect to the reference correlation computed by averaging the daily correlations during all the period of interest. When the window is chosen and supposing that the signal experienced a global velocity variation dV/V, that is stretched or compressed by a factor $t(1 \pm \varepsilon)$ respect to the reference where $\varepsilon = dV/V$ (Hadziioannou, 2006).

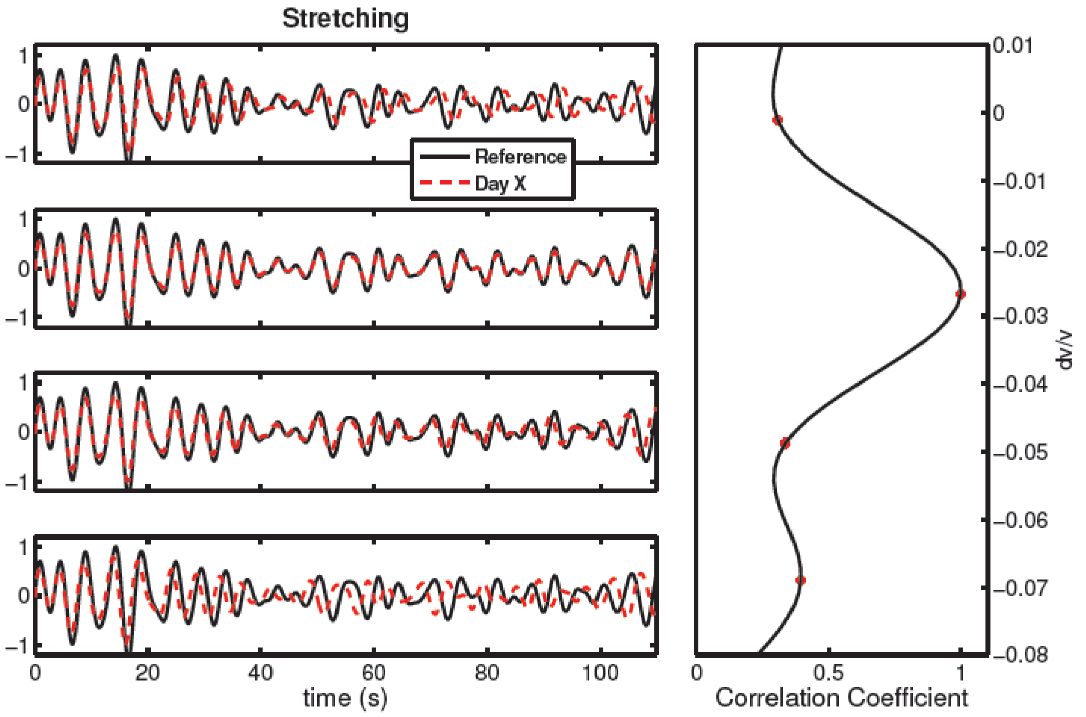

Figure 44 – *Stretching method: physical understanding.*
The signal is stretched for different values ε (left). Coefficient correlation between the signal (red) and the reference (black) are calculated for every test daily signals (right). Taken from (Hadziioannou, 2006).

The coefficient of correlation between the signal stretched h(t) and the reference h_0(t) is computed as:

$$CC(\varepsilon) = \frac{\int_{t_1}^{t_2} h\left[t(1-\varepsilon)\right] h_0[t]dt}{\sqrt{\int_{t_1}^{t_2} h^2\left[t(1-\varepsilon)\right]dt. \int_{t_1}^{t_2} h_0^2[t]dt}} \qquad \textbf{(3.2)}$$

Where t_1 and t_2 are the limits of the window chosen in the arrival time on x axis (*Figure 44*).

\

The coefficient of correlation increases until ε is similar or equal to the real value dV/V. The real seismic velocity variation corresponds to the ε in which the CC (correlation coefficient) is maximum. It is obtained by the interpolation of the CC values resulting by the tests. If the shape of the two signals is the same the CC is 1.

The stretching is applied to each 1 s window in an arbitrary time band (x axis of the correlogram). Then the probability density function (PDF) is computed. The seismic velocity variation corresponds to the $\max(PDF)$ value. The spreading of the PDF represents the confidence in the measurement and the sensitivity to moving sources that contribute to the dv/V.

Once the seismic velocity variations are computed it is necessary to compare with water table level variations or with other monitoring parameters in order to establish correlations hence assessing the goodness of the method.

We mentioned before that we are interested in surface waves' retrieval and particularly Rayleigh waves because they cross the subsurface detecting changes in physical properties. Cross correlation describes their behaviour combining specific signal components recorded by each seismometer. The possible combinations in order to get the ground motion hence the cross correlation function (CC) associated to Surface waves, are presented in *Figure 45 (a, b, c).*

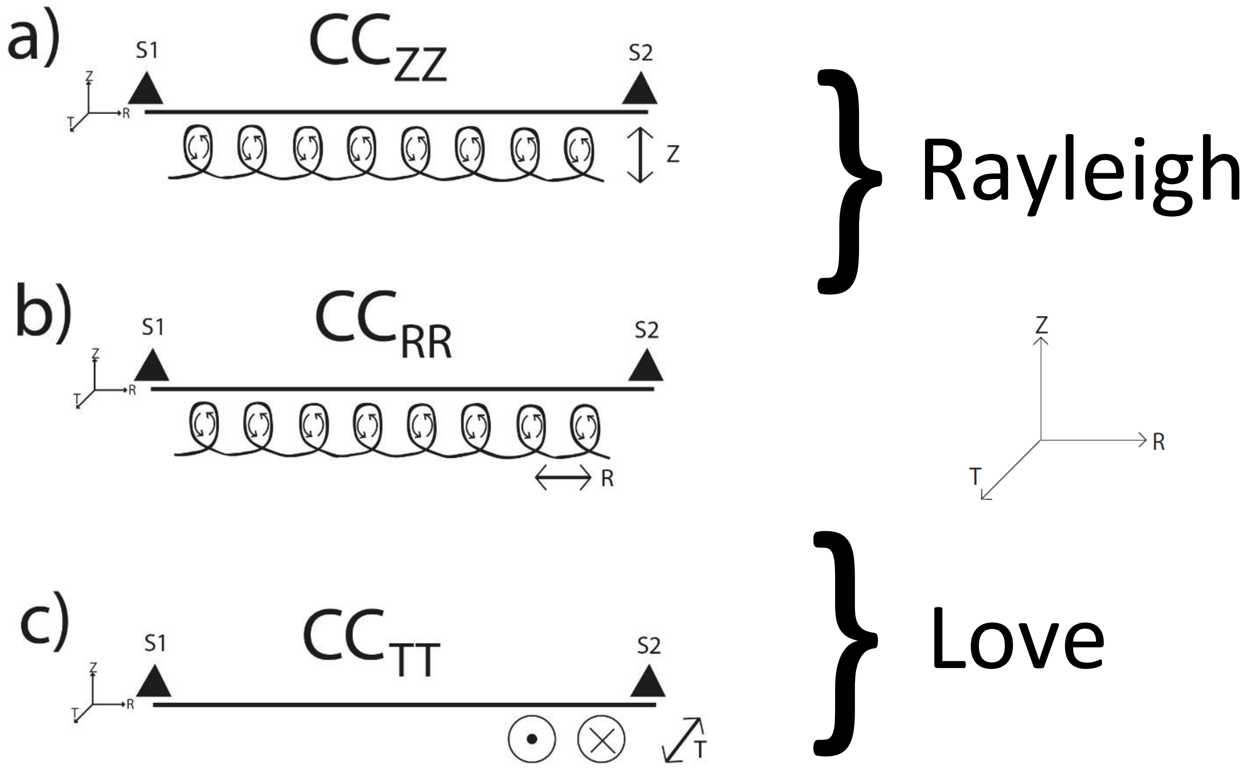

In this work the innovative clue consists in considering a single seismic station as virtual source and receiver at the same time. Therefore cross correlation is performed combining the signals of different components of the same station. The components choice is illustrated in *Figure 45 (d,e*). This new approach can have important consequences: firstly, it could lead to a new monitoring tool halving the

\

cost to seismic stations deployment but also it could give information locally nearby the station. This new technique is quite innovative.

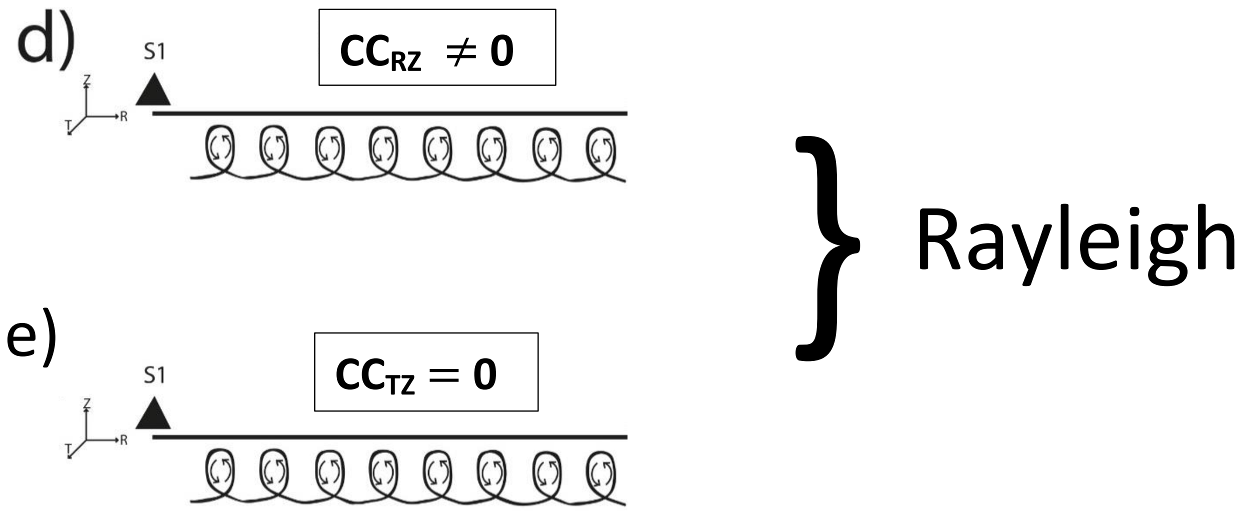

Figure 45 – Cross correlation combinations.
Cross correlation between 2 stations S1 and S2: a-b) Rayleigh waves recorded in vertical (a) and radial (b) direction; c) Love waves recorded in transverse direction. Cross correlation of the component of the same station AVP: d-e) Rayleigh waves recorded in radial (d) and transverse (T) direction.

\

3.3 Instrumentation

The research observatory OMIV "Observatoire Multidisciplinaire Instabilités de Versant" deployed three stations (3 components seismometers), AVM, AVP and AVR, in the Mas d'Avignonet *(Figure 46)* landslide in order to record continuously seismic ambient noise and analyse Earthquake activity. These three seismic stations consist on CMG40 sensors, Kephren digitizer and WARAN electronic control unit that is the station. AVR substituted CSI as reference station. AVR began to work from 05-12-2007 (when it replaced CSI) while AVM and AVP from 21-09-2006 (http://dx.doi.org/10.15778/RESIF.MT)

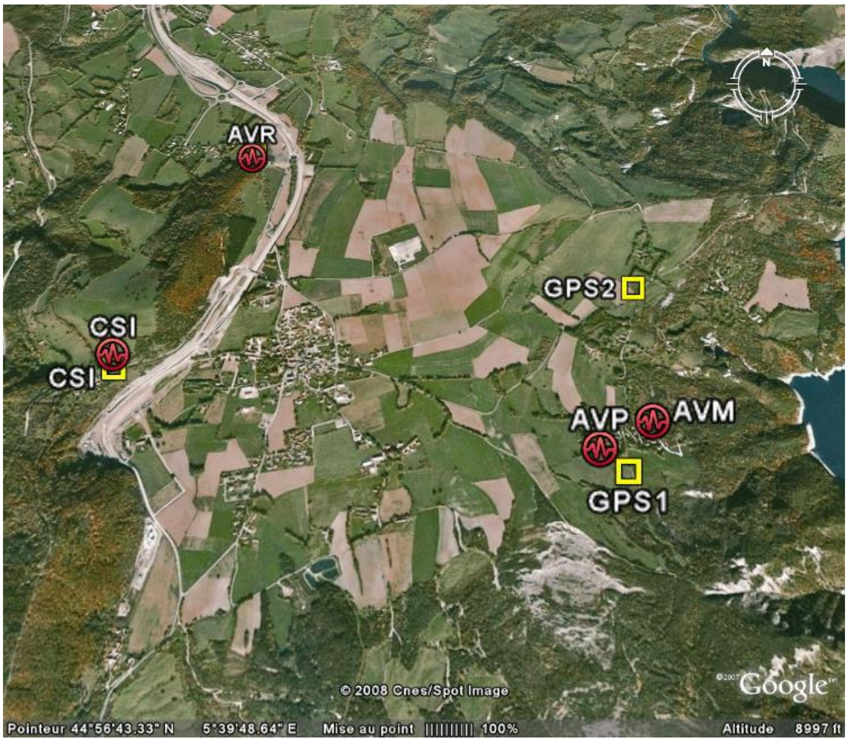

Figure 46 – Seismic and GPS stations location.
Position of the seismological stations. AVM and AVP are in the Combe du Mas d'Avignonet while AVR is on the substratum. CSI is not used actually because of practical reason.

The stations are placed:

- AVM: sensor and station are sheltered in an expropriated house in the housing estate of the Mas d'Avignonet; particularly the sensor is on the ground at foundation level.
- AVP: sensor sheltered in thermic box is buried below 30-40 cm of ground.
- AVR: sensor at 50 cm depth, 10 m far than the station (inside thermic box).

The sensor (CMG40 velocimeter) converts the ground motion (oscillation velocity of the ground particle) in electric signal that is further digitized by the seismic station (digitizer). The deconvolution of the digitized signal firstly and of the velocimeter after is necessary to retrieve the ground motion. The signal is recorded with a sampling frequency of 125 Hz.
Therefore the raw data are recorded continuously in data inventories that are accessible through RESIF web services.

In order to execute the cross correlation technique in Avignonet landslide, we decide to cross correlate the station AVM and AVP (250 m distant) (Figure 46).

\

3.4 Data processing

We perform the cross correlation of ambient seismic noise using almost 8 years (from 01-01-2008 and 16-10-2015) of continuous 3-component broadband seismic records of the AVM and AVP stations in “Mas d’Avignonet” clayey landslide. The data were provided by *RESIF - Réseau Sismologique et géodésique Français* in *.mseed* format. The main processing is presented in *Figure 47*.

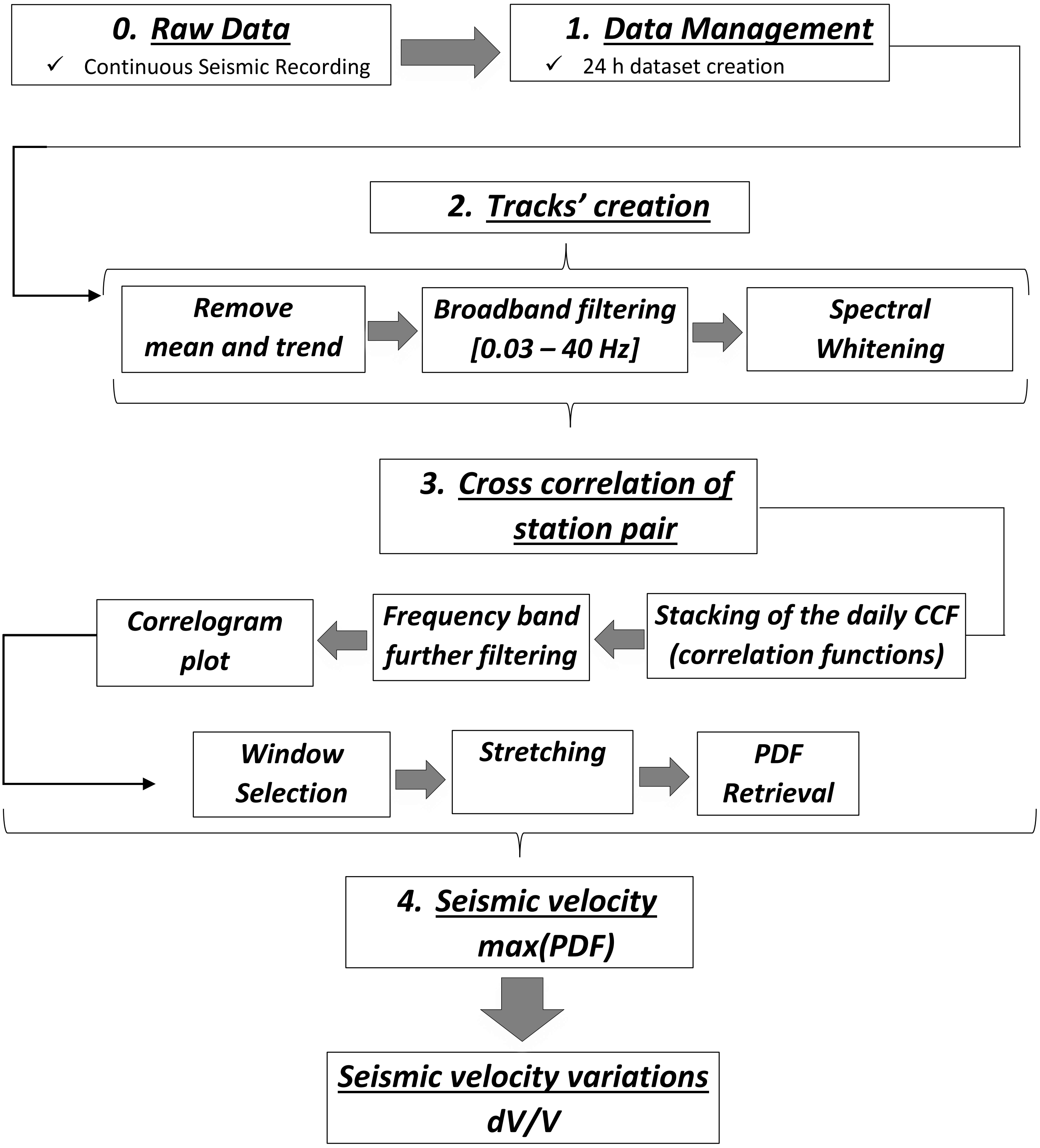

Figure 47 – Cross correlation data processing (Flow Chart).

\

Here below we describe the phases representing in bracketed italic the command used in the codes and in underlined the script used.

In **Phase 1** the data are managed and organised in daily records using "*wget*" and *"dataselect"* command in linux operating system. The daily files are then collected to yearly files because of their big amount. The data are then treated in the sub phases of **Phase 2** using PYTHON software by implemented codes:

- tracesGetParam.py set tracesParam.py for the execution.
- goodNumbers.py defines the parameter for sampling.
- tracesParam.py defines the setting parameters like the stations, the stations' components, the sampling frequency and the period of interest.
- tracesDefineTreatments.py defines the de-meaning and de-trending, the filtering (broadband) and the whitening.
- tracesMain.py calls back the previous scripts using "*python2.7 tracesMain.py*" in linux.

The output of these steps are the daily tracks created in *.npy* format. These tracks are then cross correlated in **Phase 3** by the python codes:

- correlationsParam.py defines the setting parameters like the stations, the stations' components, the maxlag, track' format (.npy) and the saving format (.mat) because of the next matlab processing.
- correlationsMain.py contains the steps in order to compute the correlations and it is executed by "python2.7 correlationsMain.py 'oneList' ../TestTraces ../TestCorr Z Z 1 0 1 0" command in linux where.

The output are the daily correlations saved in *.mat* format in order to be treated in MATLAB software taking up the **Phase 4**. This phase is treated by the matlab script:

- makeZZ.mat leading to final seismic velocity variations.

This script could be split into two steps:

Phase 4.1. The cross correlation is performed considering firstly the vertical components of AVM and AVP because we want to retrieve the vertical component of the Rayleigh Waves. Secondly, because of data loss in AVM station we perform the cross correlation between the horizontal (North and East) components and the vertical (Z) components of the AVP station in order to retrieve the radial component of the Rayleigh waves. As mentioned before these waves are dispersive and their amplitude decreases with depth. For this reason we define a specific frequency band in order to investigate a specific depth. Therefore, the Butterworth filtering is performed backward and forward in order to cancel the de-phasing. After that, the code envisages Savitsky-Golay filtering in order to increase the signal-to-noise ratio (SNR) without distorting the signal. It is important to specify the order of the stations and components definition because of wave type described (Rayleigh or Love). Moreover, defining the station pair AVM – AVP, the casual part is represented by the AVM – AVP wave's propagation (positive arrivals) while the anti-casual part the AVP – AVM direction (negative arrivals). Observing the correlogram, come out stacking up all the daily correlations in the RESU matrix, it is possible to observe the anti-symmetry of the energy arrivals because of not homogeneous noise sources distribution.

Phase 4.2. This step leads to seismic velocity variation applying the stretching method described in the section 2.1. It is necessary to select a window in the correlogram (Figure 48) in which the seismic velocity variation is computed. Because of the subjective selection, we are interested in consider the most energetic and coherent part of the correlogram. Consider the cross correlation of the vertical

\

components of the station pair AVM – AVP, this energetic part corresponds to the arrivals of ballistic surface waves and it is the maximum around 1 s (observing clear phases until 3 s). For this reason, we decided to select 1 s window in the anti-casual part from -0.6 s to -1.6 s; in order to analyse a wide range, we moved this window for 125 times (note that 125 is the sampling frequency) obtaining 125 seismic velocity variations. The Probability Density Function (PDF) is then calculated and its maximum max (PDF) allows retrieving the most probable seismic velocity variation dV/V.

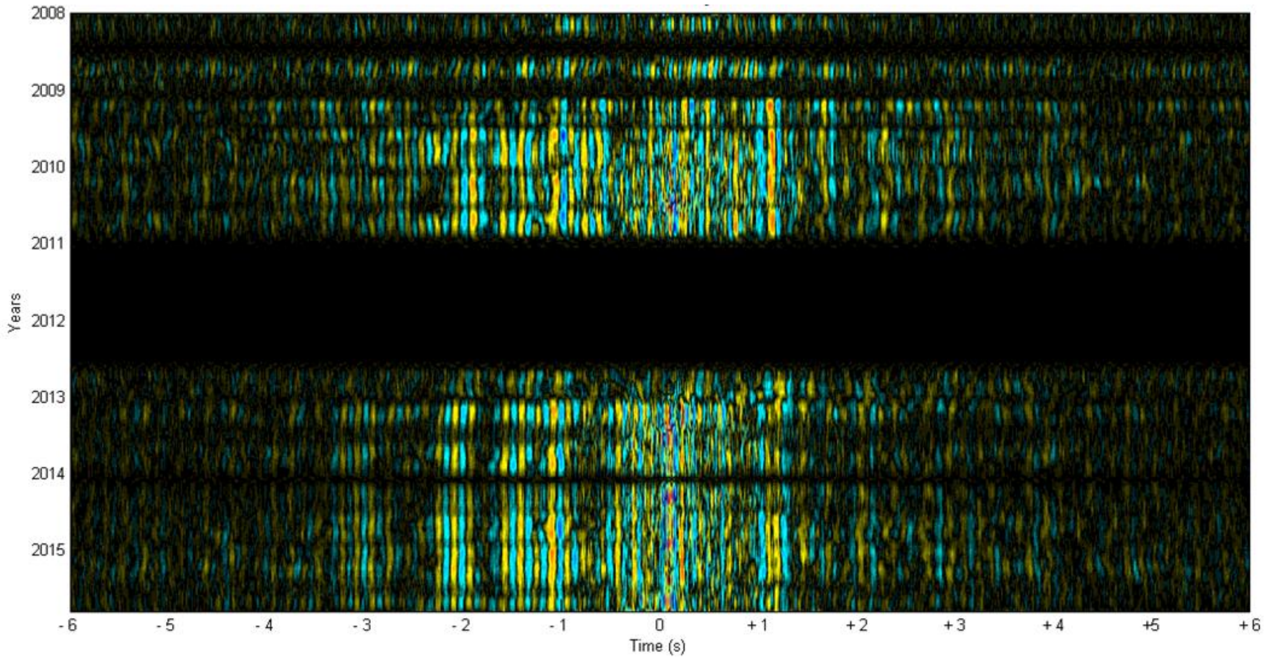

Figure 48 *– AVM_Z – AVP_Z Broadband Correlogram.*

We introduced theoretically in the section 2.1 the cross correlation of the signals of different components of the same station. Because of missing data (Figure 49) and particularly in AVM station due to work in progress in the building sheltering station, the cross correlation between the vertical components of the station pair AVM - AVP could not detect the seismic velocity variation during the whole period of interest (2008 – 2015).

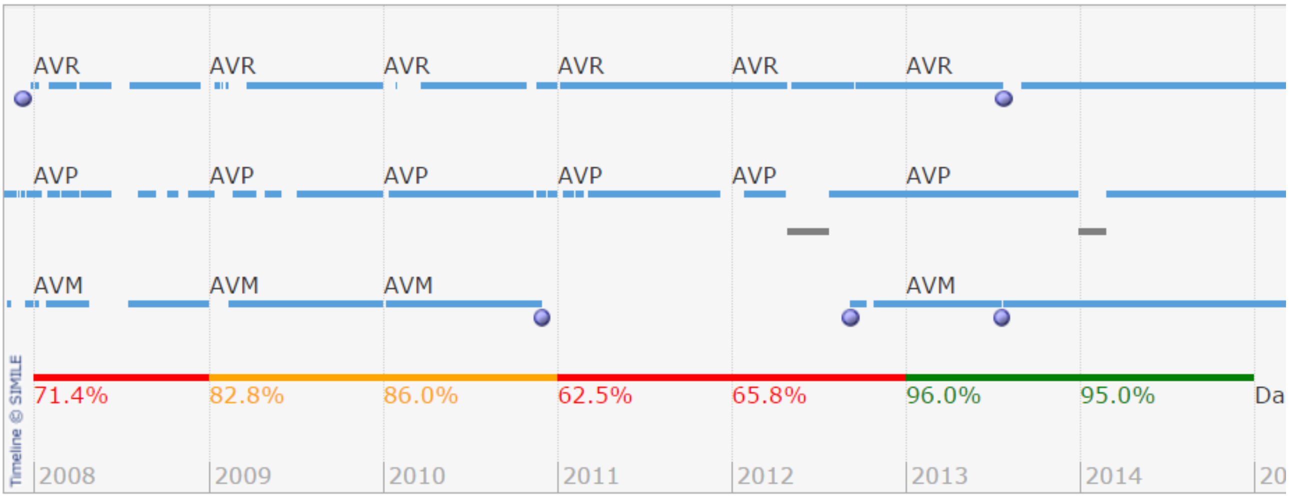

Figure 49 *– Seismic records availability.*

Timeline for the Avignonet landslide's seismological data. We observe that AVM does not work for almost two years (2011 and 2012). The line at the bottom represents the completeness of the data for every year. Taken from OMIV website. The data represents the completeness until the beginning of 2015.

\

Then the strategy is cross correlate horizontal with vertical components of the AVP station (particularly North with Z and East with Z). AVP is located in the “Combe du Mas d’Avignonet” (figure 47) 250 m far from AVM. The cross correlation between the components of the same station could be an important discovery in monitoring field because it would allow to use a station only. However, this new approach is very empirical and we will discuss about its feasibility comparing it with water table variations and with seismic velocity variations derived from the station pair AVM-AVP cross correlation.

The set of problems arisen are about the sources because AVP becomes source and receiver at the same time. The signals come from external sources that are localized everywhere around AVP and the waves could be surface or body waves but not more ballistic as before. In this case the correlograms that come out (East – Z (figure 50) and North – Z (figure 51)) present strong amplitude’s phase in the origin (source-receiver). Therefore, we select for the both cases a 0.8 window in the casual part between 0 s and 0.8 s and we moved 100 times towards the anti-casual part (until -0.8 s). Moreover, we observe more continuity in the arrival phases in East – Z correlogram than North – Z correlogram, suggesting a strong anisotropy of the medium and/or an East-West distribution of noise source. This last consideration could be right because the sources are mainly represented by the highway and anthropic activities at East and Lake and rivers at West. The only known natural noise source in North – South direction is the wind because of the Drac Valley orientation.

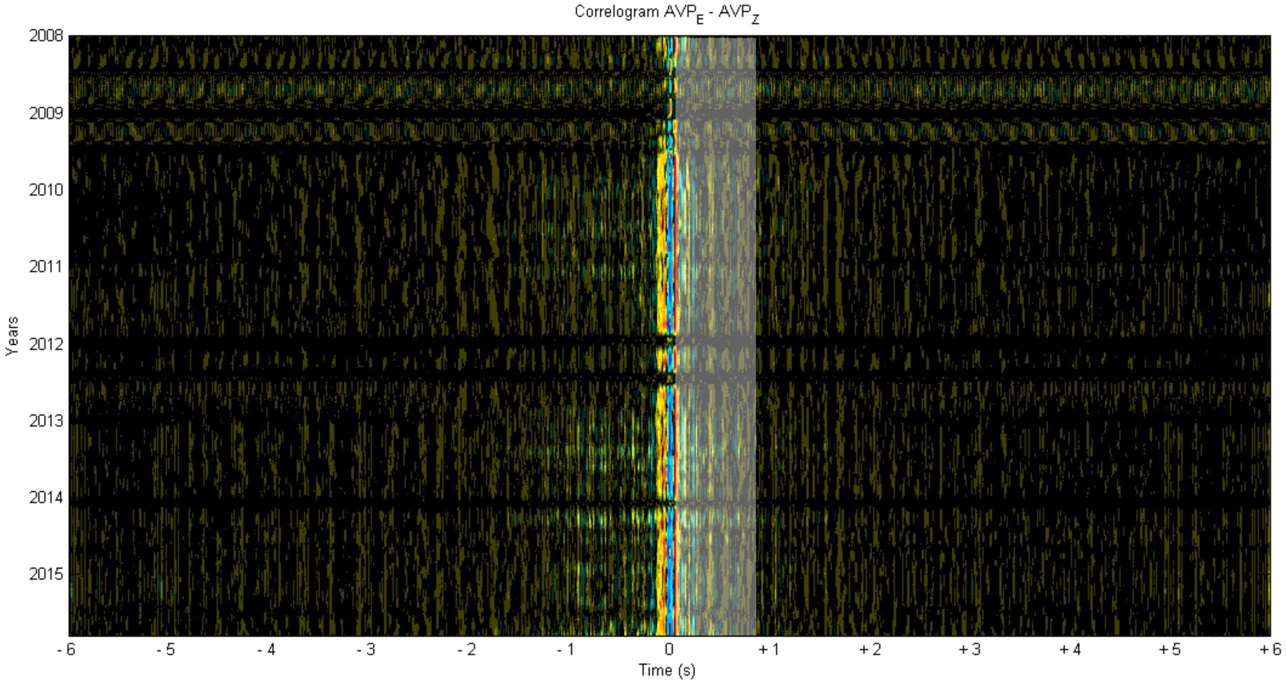

Figure 50 - *AVP$_E$ – AVP$_Z$ Broadband Correlogram.*
The white transparent rectangle represent 0.8 s window. This window is moved for 100 times through left and for everyone the seismic velocity variation is computed. The most probable seismic velocity variation among the 100 computed is the dV/V for which the PDF is maximize.

\

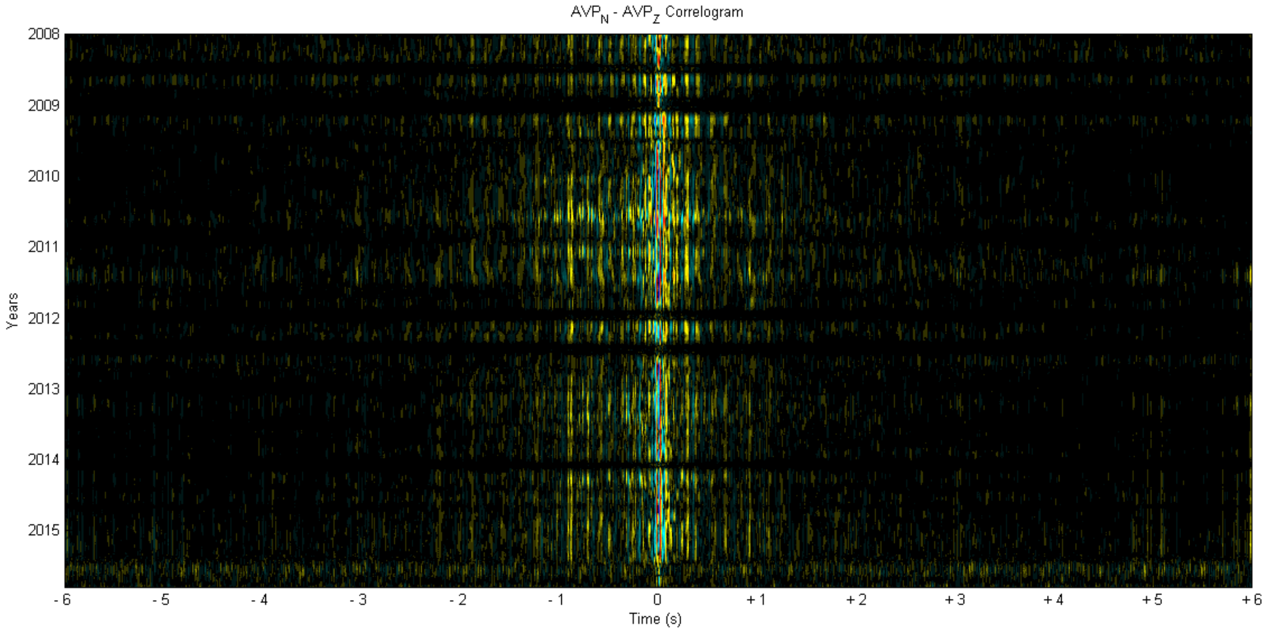

***Figure 51** – AVP_N – AVP_Z Broadband Correlogram.*

\

3.5 Results

Data processing leads to seismic velocity variations retrieval from 2008 and 2015. Firstly, we developed the “conventional” method that consists in cross correlating the seismic records of the vertical components of the stations AVM and AVP considering the broadband frequency band [0.03 – 40 Hz] (Figure 52).

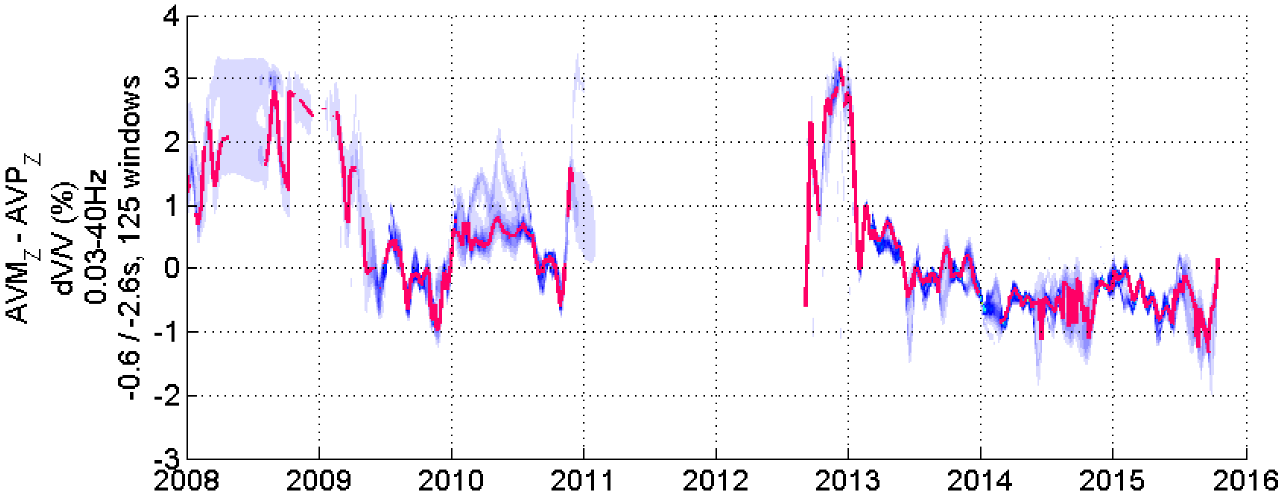

***Figure 52** – Seismic Velocity Variations for AVM_z-AVP_Z.*
dV/V obtained by the cross correlation of the vertical components of AVM and AVP in the broadband frequency [0.03 – 40 Hz]. Purple line interpolates the maximum values of the probability density function [max (PDF)]. PDF’s values are represented in blue to yellow colour scale (yellow is not apparent in the picture because hidden by purple line). We notice that most of values are distributed around the reference with PDF’s values in a limited range (intense blue colour). There are periods with high values (more than 2 %) very scattered (2008) probably because of missing data or periods in which there are an effective variation (the values around 3 % at the end of 2012) explaining probably a real physical event.

Observing the Figure 52, we can see that there is a large period with missing data because of AVM interruption. Moreover, the first year (2008) and the first part of the second (2009) are not very reliable even if we could get a general idea about the right side (positive or negative). It is worth noting that the seismic velocity variations sign is arbitrary depending on the order of the station in cross correlation. When we will correlate seismic variations with water table, we will ensure that the two trends will be consistent.

The presence of water gets slower seismic waves’ propagation provoking consequently seismic velocity variations. Therefore, we correlate these observations with the upper-perched water table because we suppose it is the most evident change in the subsurface.

The cross correlation of the seismic records of the vertical components of the station pair AVM-AVP considering broadband frequency combined with upper-perched water table variations and rainfalls is presented in the Figure 53:

\

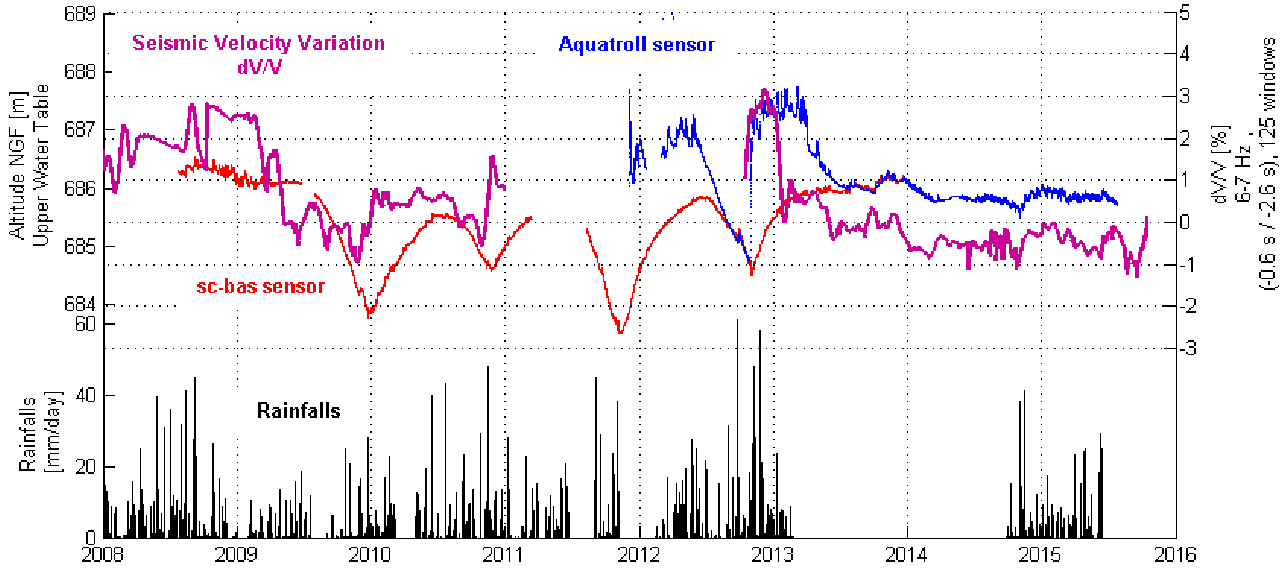

Figure 53 – *Comparison among dv/V (AVM$_Z$-AVP$_Z$, Broadband), piezometry and pluviometry. Comparison between the seismic velocity variations (purple) obtained by cross correlation of the vertical components of the station pair AVM-AVP and the upper water table (red for sc_bas and blue for aquatroll) in broadband frequency. It is possible to well correlate the annual oscillation (2009-10). From 2011 to 2013 we cannot correlate because of missing data. High values at the end of 2012 are explained by the sudden replenishment observable in aquatroll making it far from reference. From 2013 seismic trend is more stable like water table. Rainfalls are represented at the bottom in black stems.*

Previously we spoke about the sensitivity of seismic velocity changes with depth, affirming that specific frequency bands investigate specific depth. Consequently, there is a frequency band that will detect water table changes. Therefore, we tried to analyse different bands and we finally decide that the most meaningful is the 6-7 Hz band (Figure 54).

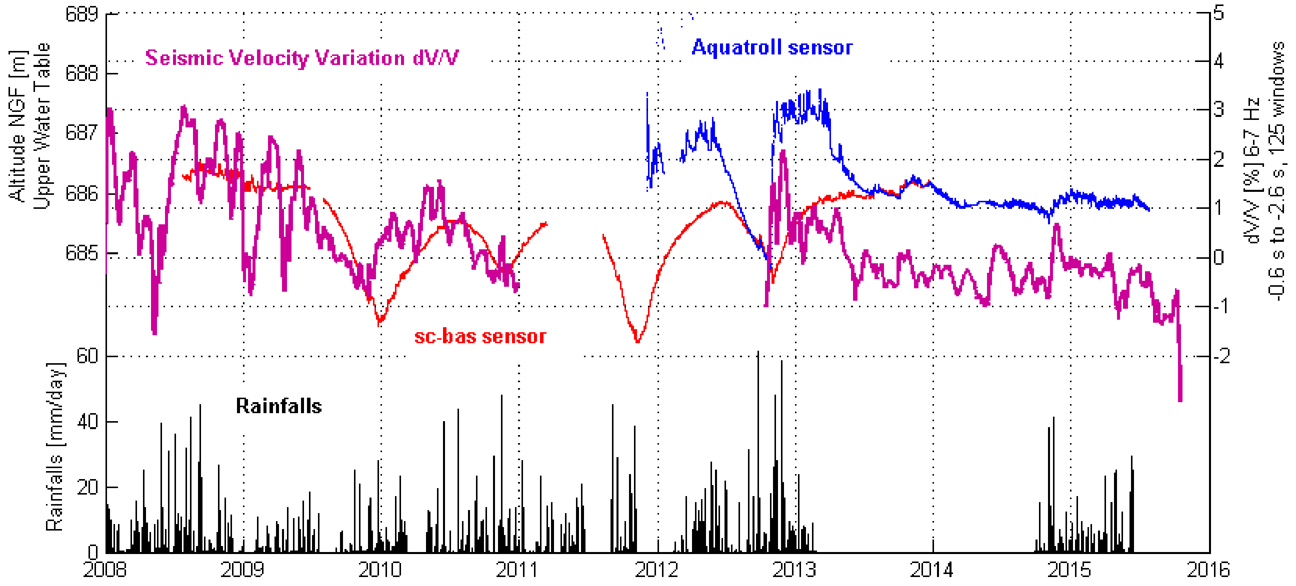

Figure 54 – *Comparison among dv/V (AVM$_Z$-AVP$_Z$, 6-7 Hz frequency band), piezometry and pluviometry. Comparison between the seismic velocity variations (purple) obtained by cross correlation of the vertical components of the station pair AVM-AVP and the upper water table (red for sc_bas and blue for aquatroll) filtering in the 6-7 Hz frequency band. It is possible to confirm the considerations done by the broadband frequency. Rainfalls are represented at the bottom in black stems.*

\

Because of the complexity of the landslide, we know from piezometrical surveys a deeper water table exists under the upper-perched water table. Therefore, we want to see if the lower water table could be detected cross correlating the seismic records of the vertical components of the two seismic stations AVM and AVP. However, first of all we have to say that the lower water table used to comparison is an interpolation resulting an approximation of the real behaviour. Secondly, since we consider a deeper layer the frequency band will be lower than the upper-perched water table and this medium change is less evident than the upper water table not allowing a satisfying detection.

Finally, we found that the frequency band that shows the better correlation with lower water table is 1-3 Hz frequency band even if the results are not so clear (Figure 55). Therefore, these results are only ground-braking understanding to verify the functioning of the method.

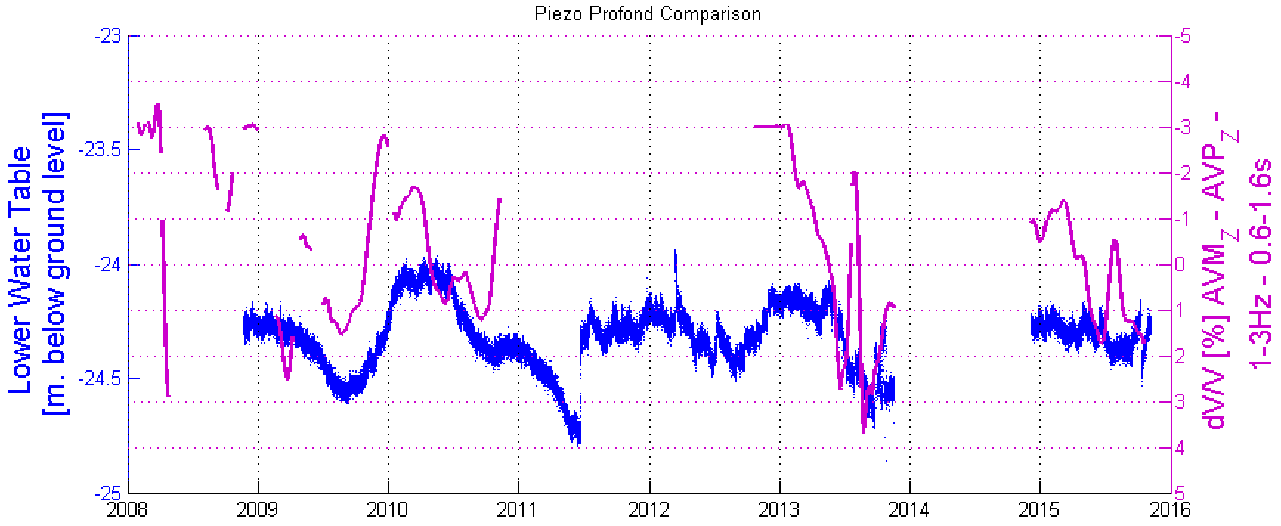

Figure 55 – *Comparison between dv/V and lower water table.*
Comparison between the lower water table and the Seismic Velocity Variation dV/V computed by the cross correlation of the vertical components of the station pair AVM – AVP filtering with 1-3 Hz frequency band. The violet line represents dv/V while the blue values represent the interpolation of the lower water table levels. This correlation is not good because of seismological and piezometrical missing data.

In order to show different behaviour choosing various frequency bands we present in the same figure (Figure tot5) the seismic velocity variations previously computed.

\

Figure 56 *– Comparison among frequncy broadband, 6-7 Hz and 1-3 Hz bands.*
We see the strong dependence between the broadband and the 6-7 Hz because in this frequency band there is a strong change in the medium governing also the broadband.

It is worth noting that here, in order to describe completely Rayleigh waves' propagation, it would be necessary to provide a rotation of the horizontal components. In fact, as mentioned in the theoretical part, Rayleigh waves' could be observed considering radial and transverse components in cross correlation. These components are got rotating horizontal components in order to align the two component considering the alignment between AVM and AVP. Therefore, further researches could be lead in this direction.

We presented above the results got cross correlating the seismic records of two different stations AVM and AVP using the method implemented officially by researchers in the last years. However, since in Avignonet we have a single stations' couple and AVM is interrupted for a large period, we decided to apply the method to the single station AVP cross correlating the signal recorded in vertical component with signals in horizontal components North and East respectively. We expect that we will retrieve seismic velocity variations in AVM missing data period. We will consider the same hypothesis and principles of the "conventional" method.

The figure below (Figure 57) represents the cross correlations of the seismic signals recorded in horizontal (North) and vertical (Elevation) components considering frequency broadband.

Figure 57 *– Seismic Velocity Variations for AVP_N-AVP_Z correlation.*
Seismic Velocity Variation dV/V obtained cross correlating North (N) and Vertical (Z) components of AVP seismic station. Purple line interpolates the maximum values of the probability density function [max (PDF)]. PDF's values are represented in blue to yellow colour scale while blue to yellow colour scale values are not so evident because the correlation coefficients got by stretching method are not high as in the case of station pair AVM – AVP. However we observe a general decreasing that is present also in the vertical components cross correlation.

Then, we will correlate this trend with the upper-perched water table (Figure 58) in order to see if the method is efficient or not.

\

Figure 58 - *Comparison between dv/V (AVP$_N$-AVP$_Z$, Broadband) and piezometry.*
Comparison between Broadband (purple) and upper-perched water table level measured by aquatroll (blu) and by sc_bas (green) in AVP$_N$ -AVP$_Z$.

The results above are very difficult to interpret probably because of external perturbation of the noise sources that in this case are everywhere around the station. The same considerations could be observe using east component in frequency broadband (not presented here). Therefore, the strategy was filtering the signal in the 6-7 Hz frequency band to reduce the noise interference and detect the upper-perched water table. We show the cross correlations of the seismic records between the horizontal (East) and vertical (Elevation) components compared with the upper-perched water table measured with sc_bas (Figure 59 a) and aquatroll (Figure 59 b).

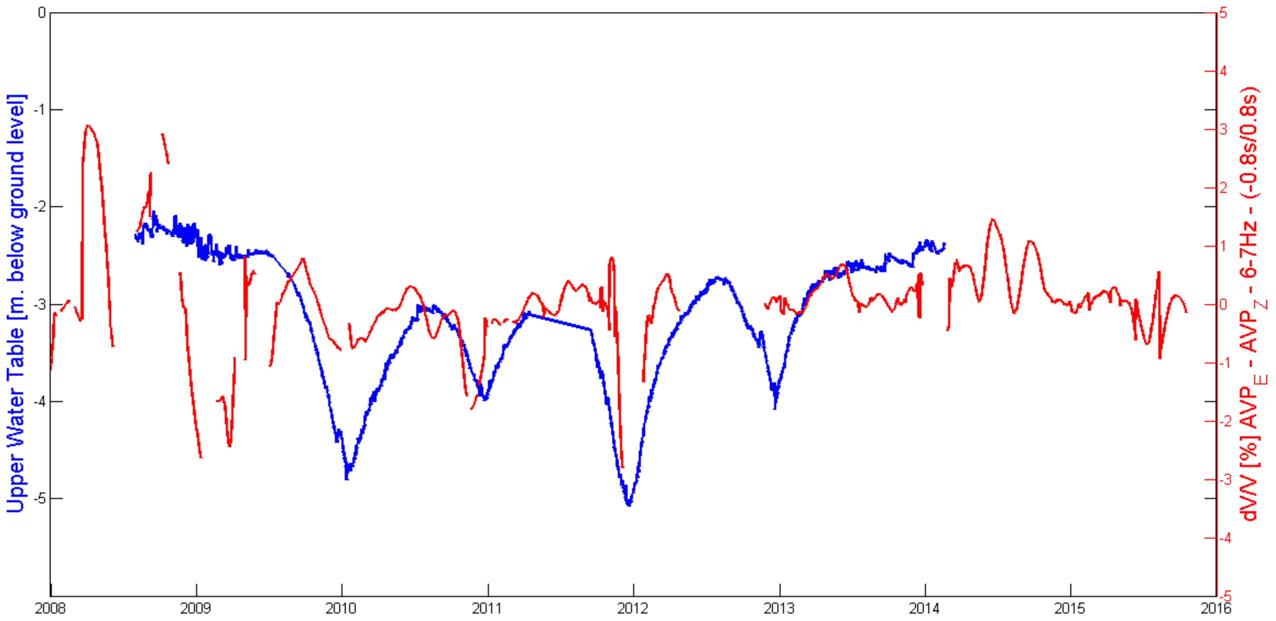

a)

\

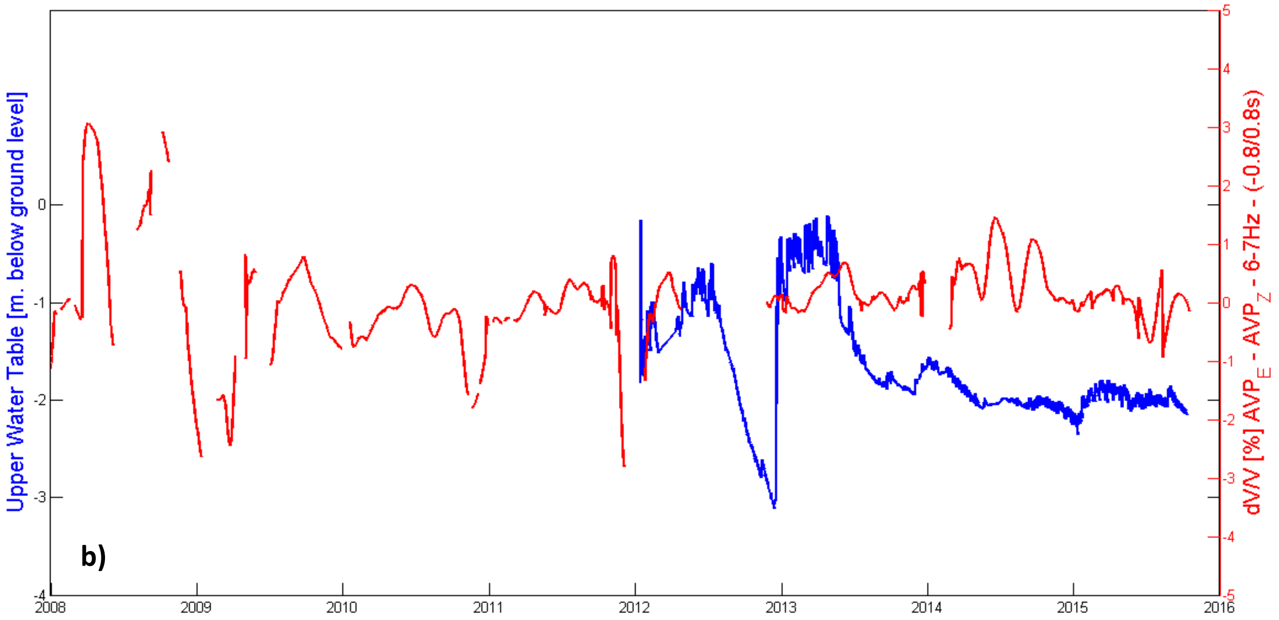

Figure 59 *– Comparison between dv/V (AVP$_E$-AVP$_Z$, 6-7 Hz frequency band) and piezometry. Comparison between 6-7 Hz frequency band (red) got cross correlating AVP$_E$ -AVP$_Z$ and upper water table level measured by (a) sc_bas and (b) aquatroll (blue).*

Observing the results, we hardly see a correlation between seismic velocities variations and the hydrology conditions of the medium. This could be due to the case study complexity and/or to the physical understanding of the method. However, it would be interesting and recommended to examine in depth its feasibility because it could be a very innovative and more economic monitoring tool.

\

4 Seismic velocity variations using poroelastic models and fluid saturation change

Previously, we proved the goodness of cross correlation of ambient noise retrieving a correspondence between seismic velocity variations and water table changes. We discussed also about the wave dispersion property showing a decreasing in frequency's wave proceeding deeply. The seismic properties changes with depth are also due to the presence of water. The influence of water table changes on Rayleigh waves could be explained by poroelastic models and fluid saturation changes (Voisin et al., 2016).

In this chapter we will apply to Avignonet's clayey landslide the principles of the Biot-Gassmann poroelastic homogenization theory (Dupuy, 2011) in order to compute the P and S waves' velocities (V_p and V_s) variations according to the water saturation. It is necessary to use poroelastic models that have to be calibrated in order to get the values of velocity observed in the field. The parameters used are seven but the porosity ϕ and the consolidation coefficient c_s are essential for model calibration. This theory was successfully verified in Utiku clayey landslide, New Zealand by Garambois and Voisin (2016) because of consistency between computed and real observed velocities. Once computed the seismic velocities as function of water saturation, it is necessary to describe the water table variation with time. Assuming that the limit between the saturated and non-saturated layer varies constantly from the minimum to the maximum depth, the corresponding surface waves dispersion curves are computed considering as boundary velocities the values previously got with poroelastic models assuming an arbitrary value of water saturation. The dispersion curves describe the slowness (reciprocal of velocity) of the Rayleigh waves respect to the frequency. Considering the velocity, we take a reference (corresponding to the average water depth) and we compute the seismic velocity variations as a function of frequency. This procedure is described schematically in the flow chart in the data processing section.

Observing Figure 60 related to the results got by Garambois and Voisin (2016) in Utiku, it is possible to observe that the seismic variations are frequency dependant and in this case are consistent with the seismic velocity changes obtained by cross correlation of ambient seismic noise. It also allow to get dv/V generated by water table variations which also were consistent with observations.

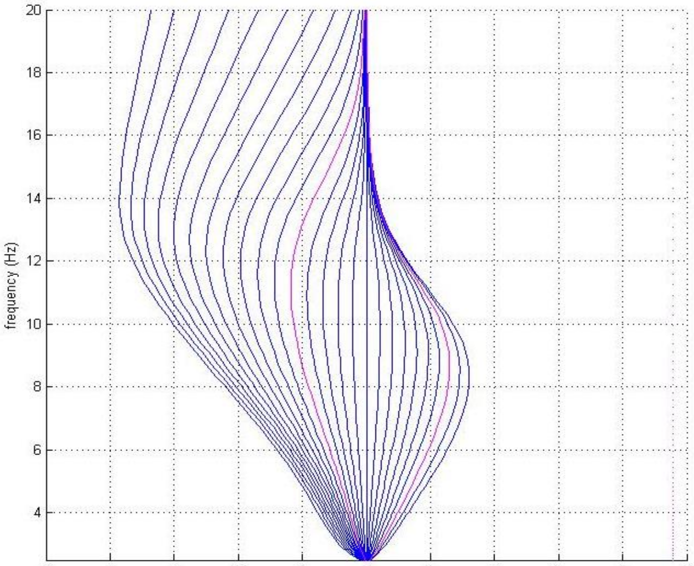

Figure 60 – *dv/V as a function of frequency (Utiku case study).*
The red lines correspond to the minimum (right) and maximum (left) depth of water table.

\

We will apply the same procedure to the Avignonet case study in order to implement a further monitoring tool to widely described landslide independently to the results obtained. Before applying it we will present on a quality level the Biot-Gassmann homogenization theory and the dispersion curve retrieval procedure.

4.1 Biot – Gassmann homogenization theory

The Biot-Gassmann homogenization theory was developed in order to study the waves' propagation in multiphasic porous media (Dupuy, 2011). Before that, the seismic waves' propagation was described by the elastodynamic theory (Lamb, 1904). The fundamental dynamic principle of the conservation of momentum (Newton's second law) was applied to a solid elastic medium approximation. The material rheology was described by Hooke's law relating stresses (σ) and strains (ε) linear relationship making the assumption of small displacements consistent with the wave propagation properties (Dupuy, 2011). Therefore, making the assumptions that the waves propagate in a plane with an invariant direction, the general elastodynamic equations by literature are:

- Equation of motion:

$$\frac{\partial \sigma_{j,i}}{\partial x_j} + F_i = \rho \frac{\partial^2 u_i}{\partial t^2} \qquad (\mathbf{4.1})$$

Where $\sigma_{j,i}$ are stresses, F_i are body forces, ρ mass density and u_i displacements.

- Strain-displacement equations:

$$\varepsilon_{i,j} = \frac{1}{2}(u_{j,i} + u_{i,j}) \qquad (\mathbf{4.2})$$

Where $\varepsilon_{i,j}$ are strains, $u_{i,j}$ displacements.

- Constitutive equations:

$$\sigma_{i,j} = C_{ijkl}\varepsilon_{kl} \qquad (\mathbf{4.3})$$

Where C_{ijkl} is the stiffness tensor.

The body waves are P and S waves that in surface they interact producing the elliptical and dispersive Rayleigh waves (Figure 61).

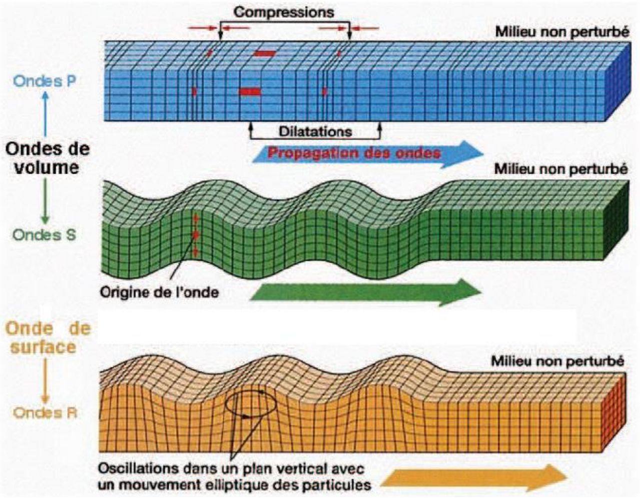

Figure 61 – Waves' propagation in a 2D elastic medium.
(Figure taken from Dupuy, 2011).

\

In the middle of 20th century, there was the exigence not to consider the soil only as an elastic continuum. Poromechanics considered the soil as fluid-saturated porous media whose solid matrix is elastic and the fluid is viscous. Biot and Gassmann are considered the fathers of the poroelastic homogenization theory. In his studies (1935-1957), Biot described the mechanical behaviour of a poroelastic medium. The equation's theory are derived from:

- Linear elastic equations for solid phase
- Navier-Stokes equations for liquid phase
- Darcy's law for the flow of fluid through the porous matrix

<u>Poroelastodynamic equations</u> are presented in a system in frequency domain (Dupuy, 2011) are the following:

$$\begin{cases} \nabla.\tau = -\omega^2(\rho\,\vec{u} + \rho_f\vec{\omega}) \\ \tau = [K_U\nabla.\vec{u} + C\nabla.\vec{\omega}]I + G\left[\nabla\vec{u} + (\nabla\vec{u})^t - \frac{2}{3}\nabla.\vec{u}\,I\right] \\ -P_f = C\nabla.\vec{u} + M\nabla.\vec{\omega} \\ -\nabla P_f = -\omega^2\left(\rho_f\vec{u} + \tilde{\rho}(\omega)\vec{\omega}\right) \end{cases} \qquad \mathbf{(4.4)}$$

These equations are deducted by solid and fluid dynamics and mechanics. Tensor τ is the stress tensor and P_f is pore-water pressure. By the definition of solid and fluid displacements $\overrightarrow{u_s}$ and $\overrightarrow{u_f}$, we get the porous medium's volume displacement $\vec{u}$. The vector $\vec{\omega}$ is the relative solid/fluid displacement related to $\overrightarrow{u_f}$ by the relationship $\omega = \varphi(\overrightarrow{u_f} - \overrightarrow{u_s})$. The physical parameters $(K_U, C, G, M, \rho_f\,, \rho, \tilde{\rho}(\omega))$ are constant in time and space dependent while the displacements are dependent on space and time.

The physical parameters come from the homogenization of solid and fluid phases in order to build a unique equivalent poroelastic medium defined by these 7 parameters. The homogenization (Dupuy, 2011) is obtained combining the drained medium that is the solid matrix derived by the association of minerals grains and the undrained medium that is the combination of the solid matrix and the fluid phase (*Figure 62*). Each step has its parameters leading to the 7 parameters employed in the poro-elasto-dynamic equations.

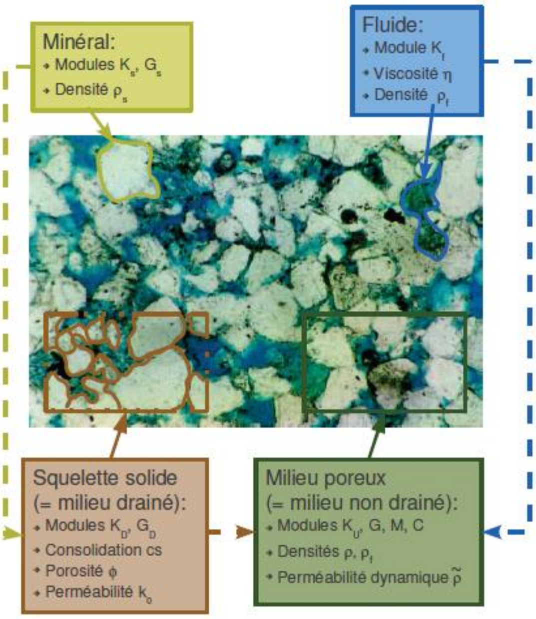

Figure 62 – Schematic representation of the different phases in a porous medium. Homogenization process specifying physical parameters for each phase.

\

Once defined the porous medium it is necessary to study the waves' propagation through it defining the waves' velocity as a function of water saturation applying the poroelastodynamic equations defined previously.

In poroelastic media there are three elastic seismic waves: a shear wave, and two types of compressional waves, which Biot called type I and type II waves. The transverse and type I (or fast) longitudinal waves are similar to the S and P waves in an elastic solid, respectively. The slow compressional wave, (also known as Biot's slow wave) is unique to poroelastic materials. The prediction of the Biot's slow was confirmed by Thomas Plona experiments in 1980.

For our case study we neglect the Biot's wave type because we are interested in dispersive Rayleigh waves that are the combination of P and S longitudinal waves. In the following chapter we will present how to build a dispersion curve that expresses the Rayleigh wave slowness respect to frequency.

4.2 Dispersion curves

Previously, we discussed about the dispersion of the surface waves (Rayleigh or Love) with frequency (depth). Rayleigh and Love are generated by the interaction of P and S waves with discontinuities of the shallow subsurface. The propagation wave velocity depends on the frequency increasing with depth (low frequencies). This aspect gives us information about the medium crossed (*Figure 63*).

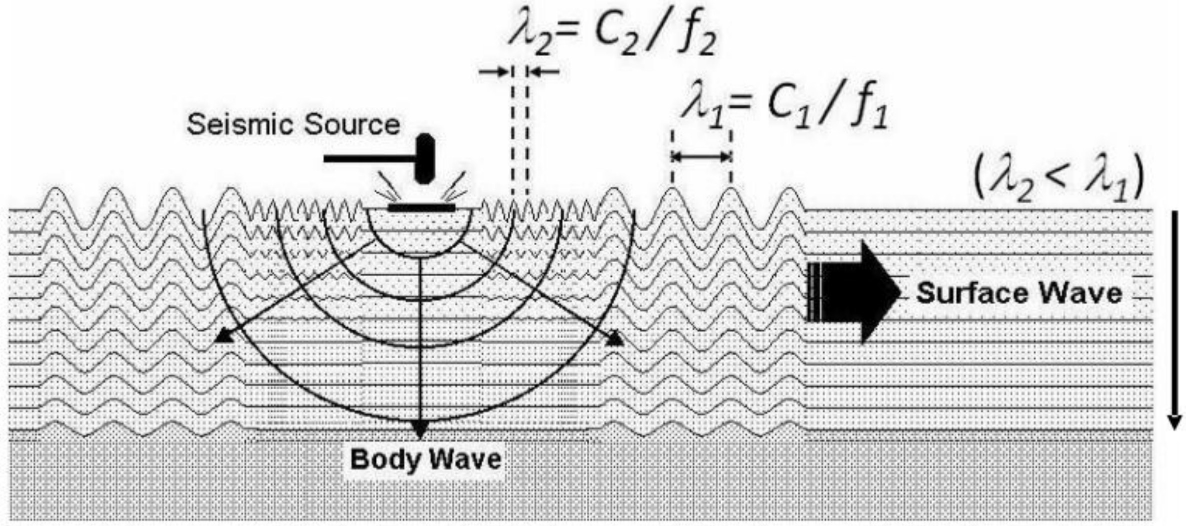

Figure 63 – Surface wave formation and propagation in the subsurface.
The dispersion property is observed by the fact that high frequency waves are more superficial than low frequency (high wavelength). Large wavelength interact with lower layers.

In this work our purpose is to observe the weak influence of the water table level in the dispersion curve retrieval. Assuming the Biot-Gassmann homogenization theory, we consider that water table changes with time dividing the ground layer in saturated and non-saturated zone. The waves' propagation is different if the medium is above or below the water table. Computing with poroelastic model P and S waves' velocities as a function of water saturation, we take the values for saturated and non-saturated layer. Then dispersion are computed changing the water table levels from the lower to the higher one. In this work the phase velocity of Rayleigh waves is considered. GEOPSY command –gpdc in linux environment computes "phase or group velocity dispersion curve for either Rayleigh or Love waves given a layered 1D earth model in simple ASCII format (Geopsy official website).

\

4.3 Data Processing and Results

The main processing flow is represented by the following figure:

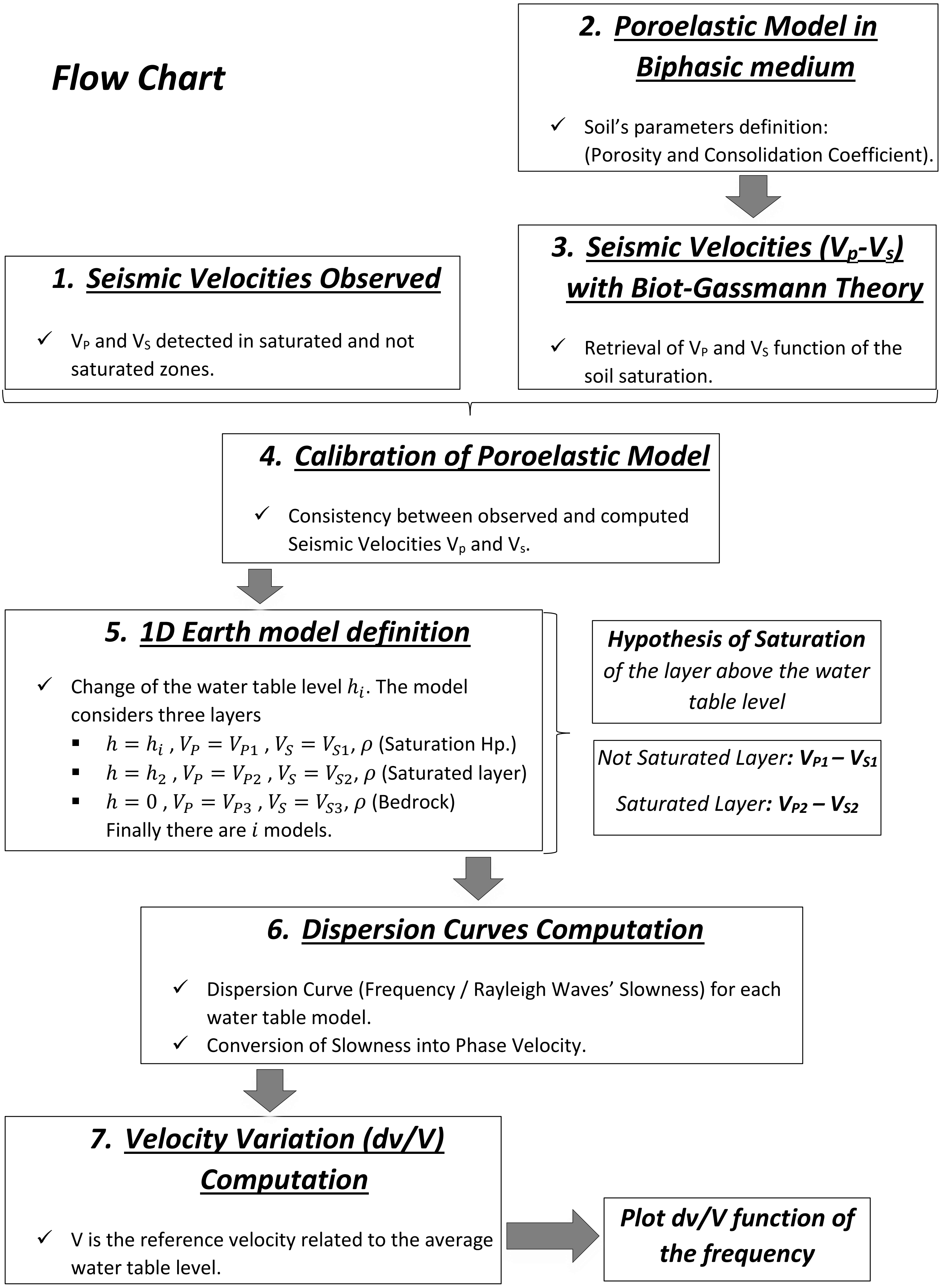

Flow Chart

2. *Poroelastic Model in Biphasic medium*

- ✓ Soil's parameters definition: (Porosity and Consolidation Coefficient).

1. *Seismic Velocities Observed*

- ✓ V_P and V_S detected in saturated and not saturated zones.

3. *Seismic Velocities (V_p-V_s) with Biot-Gassmann Theory*

- ✓ Retrieval of V_P and V_S function of the soil saturation.

4. *Calibration of Poroelastic Model*

- ✓ Consistency between observed and computed Seismic Velocities V_p and V_s.

5. *1D Earth model definition*

- ✓ Change of the water table level h_i. The model considers three layers
  - $h = h_i$, $V_P = V_{P1}$, $V_S = V_{S1}$, ρ (Saturation Hp.)
  - $h = h_2$, $V_P = V_{P2}$, $V_S = V_{S2}$, ρ (Saturated layer)
  - $h = 0$, $V_P = V_{P3}$, $V_S = V_{S3}$, ρ (Bedrock)

  Finally there are i models.

Hypothesis of Saturation *of the layer above the water table level*

Not Saturated Layer: $V_{P1} - V_{S1}$

Saturated Layer: $V_{P2} - V_{S2}$

6. *Dispersion Curves Computation*

- ✓ Dispersion Curve (Frequency / Rayleigh Waves' Slowness) for each water table model.
- ✓ Conversion of Slowness into Phase Velocity.

7. *Velocity Variation (dv/V) Computation*

- ✓ V is the reference velocity related to the average water table level.

Plot dv/V function of the frequency

\

Figure 64 – Data processing (Flow Chart).

Now we will describe every phase with the values of the parameters used:

In the **Phase 1** we recover from previous monitoring surveys (Bièvre, 2010) P and S waves' velocities (V_P and V_s), porosity (ϕ) and consolidation parameter (c_s). These terms will be used to create (ϕ, c_s, **Phase 2**) and calibrate (V_P and V_s, **Phase 4**) the poroelastic models (Dupuy, 2011).

Considering that the earth's model required by GEOPSY (**Phase 6**) for the dispersion curve computation is 1D layer, we assume an average value for porosity and consolidation parameter for the layer. By literature we assume as reasonable a value of porosity 42 % (table) while the consolidation parameter will be essentially the adimensional calibration parameter (finally we used 500). These values are put in the *avignonetbid.mod* poroelastic model where the other physical parameters of the homogenization theory are present.

Table 2 – Values of the physical ground properties. Average values ρ_{sat}, volumic water content and porosity measured in the borehole T4. It is interesting to see the stratigraphy. (Bièvre, 2010).

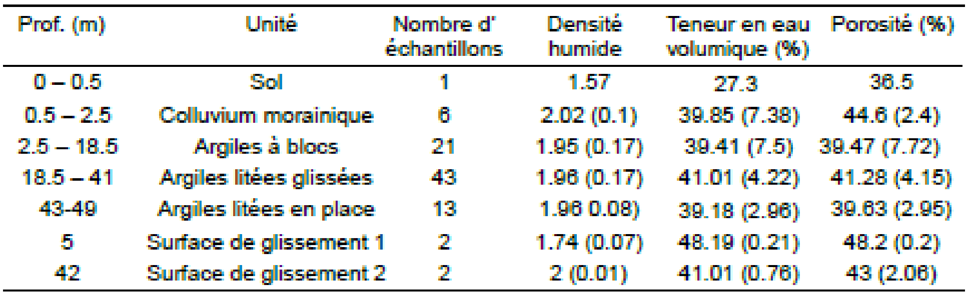

Prof. (m)	Unité	Nombre d' échantillons	Densité humide	Teneur en eau volumique (%)	Porosité (%)
0 – 0.5	Sol	1	1.57	27.3	36.5
0.5 – 2.5	Colluvium morainique	6	2.02 (0.1)	39.85 (7.38)	44.6 (2.4)
2.5 – 18.5	Argiles à blocs	21	1.95 (0.17)	39.41 (7.5)	39.47 (7.72)
18.5 – 41	Argiles litées glissées	43	1.96 (0.17)	41.01 (4.22)	41.28 (4.15)
43-49	Argiles litées en place	13	1.96 0.08)	39.18 (2.96)	39.63 (2.95)
5	Surface de glissement 1	2	1.74 (0.07)	48.19 (0.21)	48.2 (0.2)
42	Surface de glissement 2	2	2 (0.01)	41.01 (0.76)	43 (2.06)

V_P and V_s values are taken from the different monitoring campaigns realised. We take into account the down-hole essays and the seismic tomography realised. Finally, the observed values (combining down-hole and tomography) are:

Non-saturated layer: V_{P1}=500 m/s, V_{S1}=220 m/s; Saturated layer: V_{P2}=1850 m/s, V_{S2}=200 m/s;

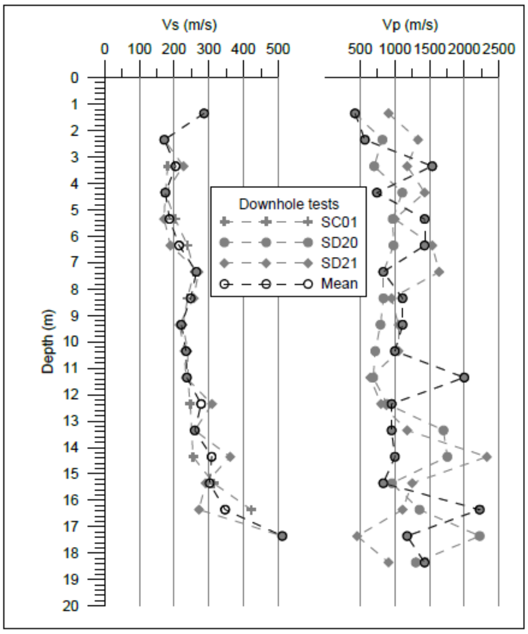

Figure 65 – Down-hole essays realised in the boreholes.
SC01, SD20 and SD21. (see location fig. 6). Figure taken by Bièvre (2010).

\

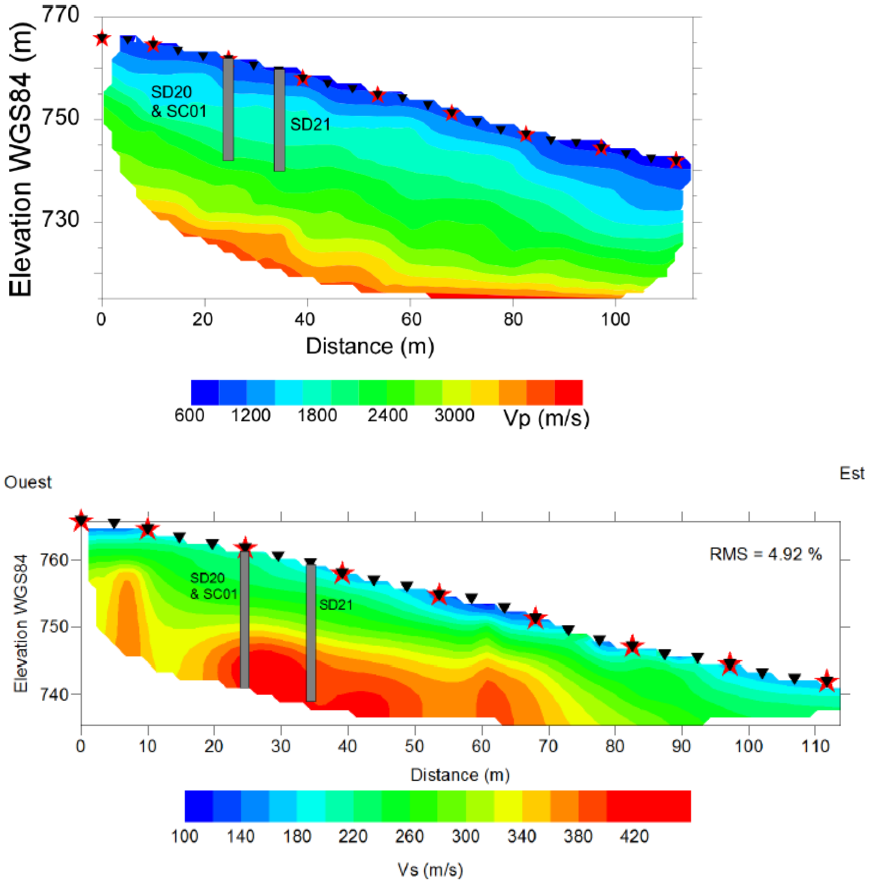

Figure 66 – *Seismic Tomography for P and S waves' velocity.*
Taken from Bièvre (2010).

In **Phase 3** P and S waves' velocities are computed theoretically compiling the fortran code *vitesse.f* (developed by Garambois, 2011) computing V_P and V_s as a function of water saturation (figures).

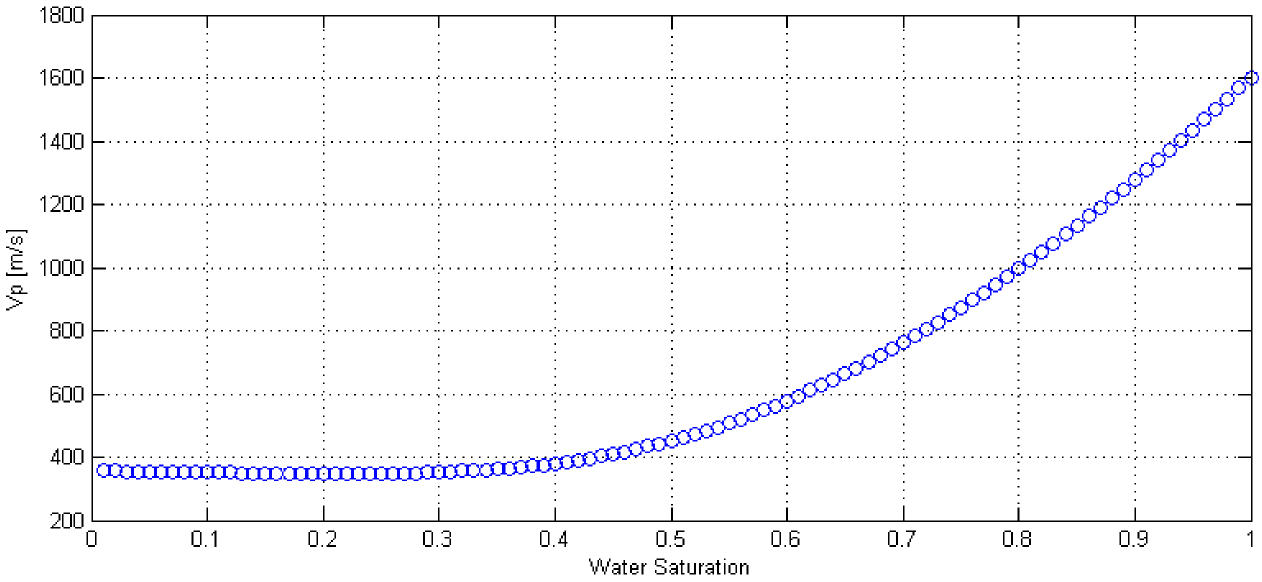

\

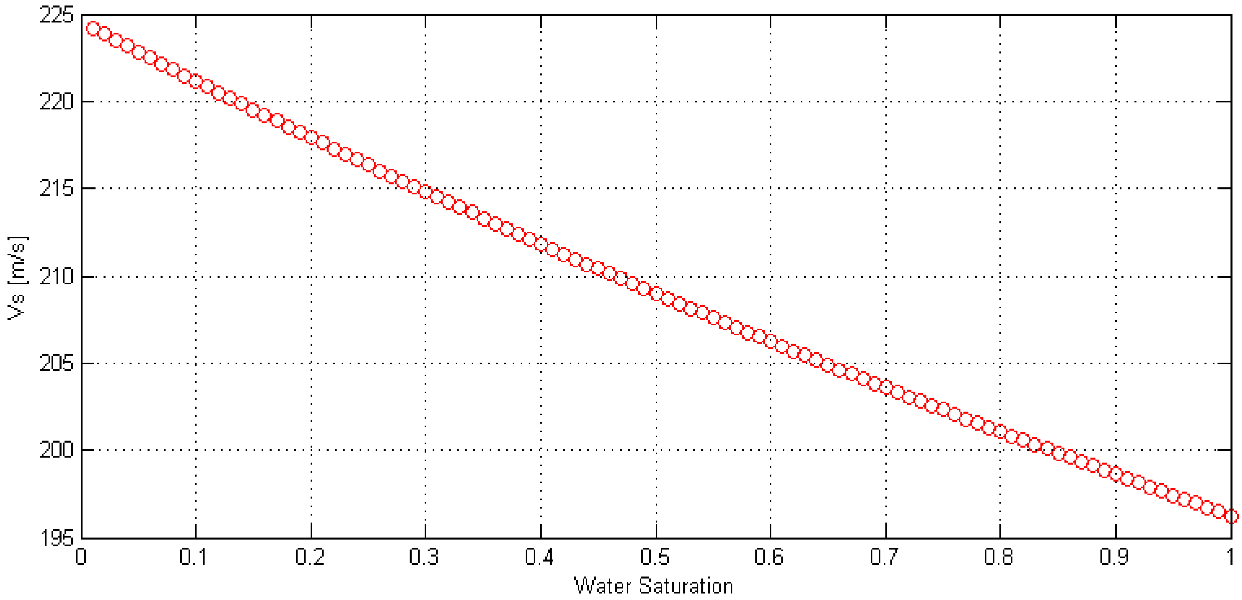

Figure 67 – *Seismic velocities (V_P and V_S) respect to water saturation*.
V_P a) and V_S b) as a function of water saturation. We observe that V_S decreasing is almost linear while V_P shows an exponential growth.

Poroelastic models are then calibrated respect to the real observed values previously defined playing mostly on the consolidation parameter.

After this we assume from TDR results and volumic water content (fig. above) that the fluid saturation of the non-saturated zone is about 60%. Therefore taking the corresponding V_P and V_s values for saturated (100% water saturation) and non-saturated (60% saturation) layer we can define the 1D Earth models for every water table levels. The model requires also a value of density ρ that we set 2000 kg/m^3. We decided (**Phase 5**) to create a model *watertableiim.model* every 0.2 m from 6 m to 0.2 m depth (the command lines are taken from geopsy website):

```
Line 1: <number of layers including half-space for first model>
Line 2: <thickness (m)> <Vp (m/s)> <Vs (m/s)> <Density (kg/m3)> [<Qs> <Qp>]
 ....
Line n: 0 <Vp (m/s)> <Vs (m/s)> <Density (kg/m3)> [<Qs> <Qp>]
Line n+1: <number of layers including half-space for second model>
```

The dispersion curves are then computed (**Phase 6**) with the GEOPSY command gpdc:

```
-  gpdc < test.model < newdispersioncurve.disp
```

\

We are interested in the mode 0 of the Rayleigh phase velocity computation in the frequency range -3 to -70 Hz so the options are set by default:

```
-n <count>                Number of frequency samples (default=100)
-L <n modes>              Number of Love modes (default=0)
-R <n modes>              Number of Rayleigh modes (default=1)
-grid <L | R>             Ouput a grid of the wave solutions (not set by default). The letter L or
                          R stands for Love or Rayleigh.
-group                    Switches to group slowness (default=phase)
-s <sampling>             Defines the sampling type:
                            period     regular sampling in period
                            frequency  regular sampling in frequency
                            log        regular sampling in log(frequency) (default)
-min <min>                Minimum of range for dispersion curve (default=0.2)
-max <max>                Maximum of range for dispersion curve (default=20)
-vn <count>               Number of velocity samples (only for -grid, default=100)
-vmin <min>               Minimum of range for velocity (only for -grid, default=100)
-vmax <max>               Maximum of range for velocity (only for -grid, default=3000)
```

Phase velocity is the velocity of each wave with a given frequency. In particular the dispersion curves expresses results in term of slowness (reciprocal of Rayleigh wave's phase velocity) as function of frequency (*Figure 68*). The output of –gpdc command has .dat format that we implement in matlab in order to change the slowness in Rayleigh waves velocity.

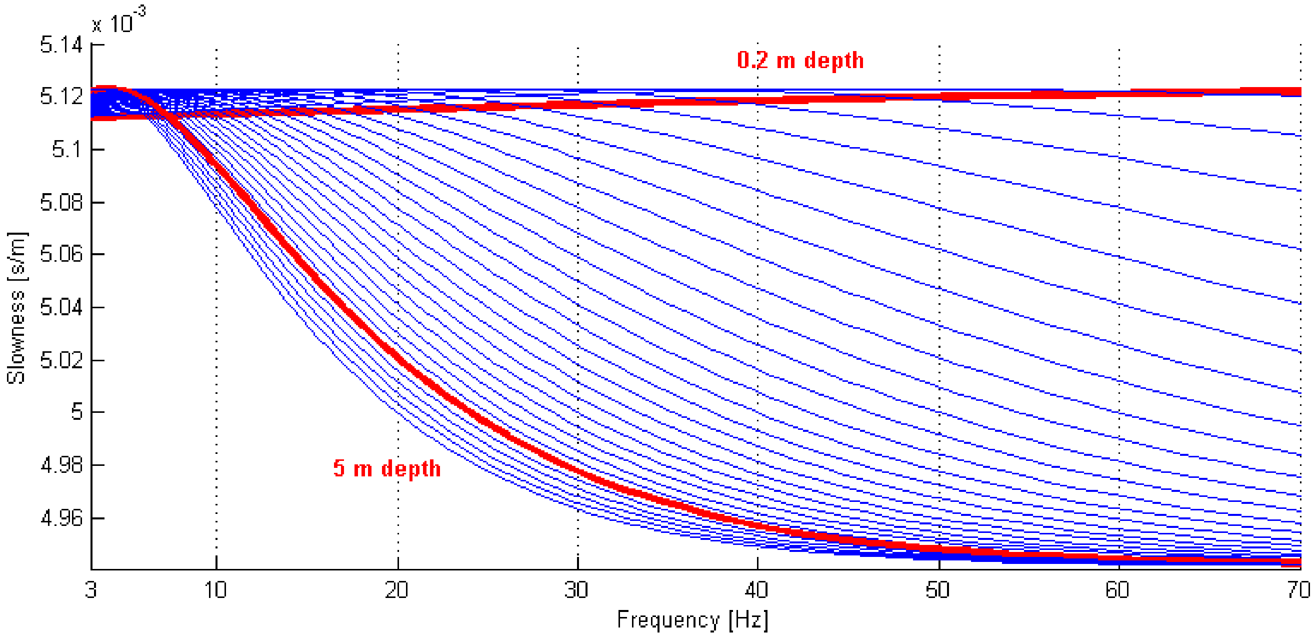

Figure 68 – Dispersion curves computed by –gpdc command.
It is possible to see that the dispersion is more evident for the deepest layers. The red lines are the curves related to the minimum and the maximum water table level.

In order to compute the seismic velocity variations, it is necessary to convert the slowness into the Rayleigh waves' phase velocity (*Figure 69*).

\

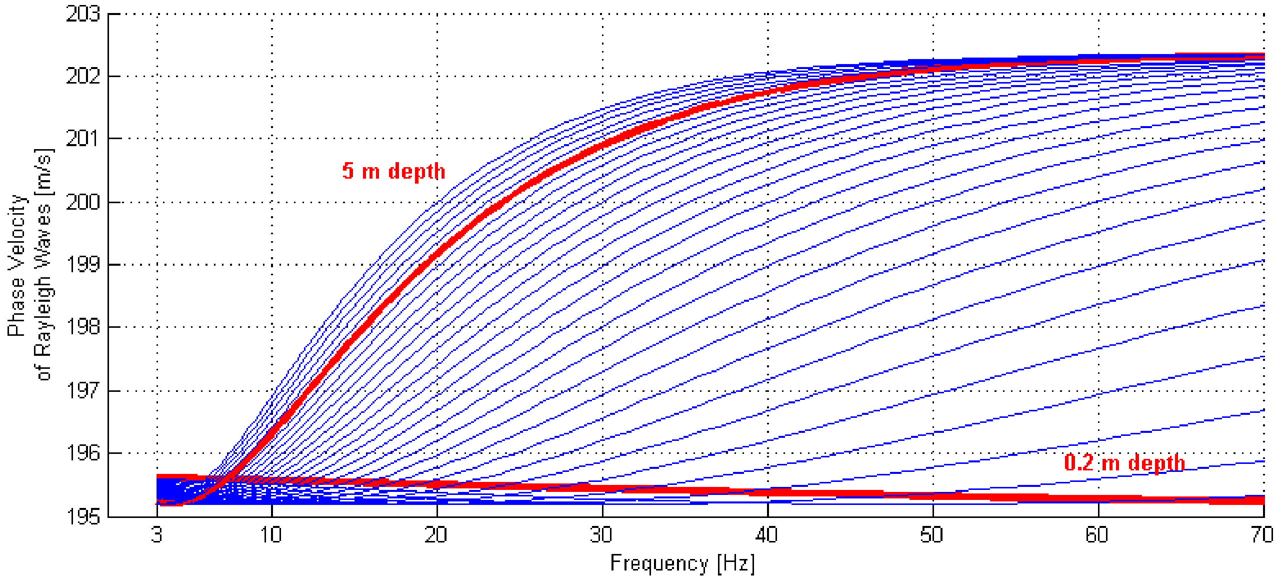

Figure 69 – The dispersion curves got converting the slowness into velocity.
It is possible to see that the dispersion is more evident for the deepest layers. The red lines are the curves related to the minimum and the maximum water table level.

We then consider a reference velocity corresponding to the average water table level (- 3 m depth) and we compute the difference between velocities got by each model and the reference (**Phase 7**). The final output is represented by seismic velocity variations respect to the reference value as function of frequency like Utiku results *(Figure 70).*

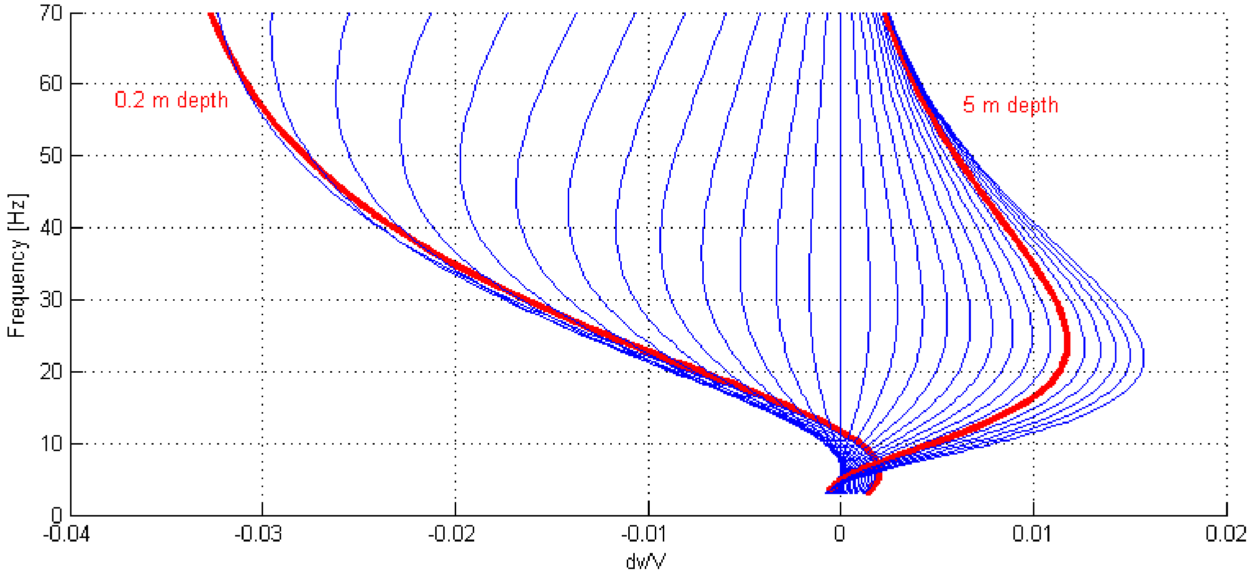

Figure 70 – Seismic Velocity Variations dv/V as a function of frequency.
The bold red lines correspond to the minimum and the maximum level reached by the water table. We can see that the deepest layers are influenced by low frequency while the shallow surface is more sensitive to high frequencies.

We can see that the shape is the same of that got by Garambois and Voisin (2016) confirming the method consistency. The deepest layers are not sensitive to the highest frequencies contrary to the shallow layers. However, the frequency values corresponding to the seismic velocity variations computed with cross correlation of ambient seismic noise are higher respect to Garambois and Voisin results. This could

\

be explained assuming that in Avignonet's case we have not homogeneous conditions and the role of fissures is very important.

Here below we consider seismic velocity variations (*Figure 71*) and frequency values (*Figure 72*) corresponding to the minimum and maximum level of the water table. They are represented respect to reference value consider as water table level moving it from 1 m to 6 m below the ground surface.

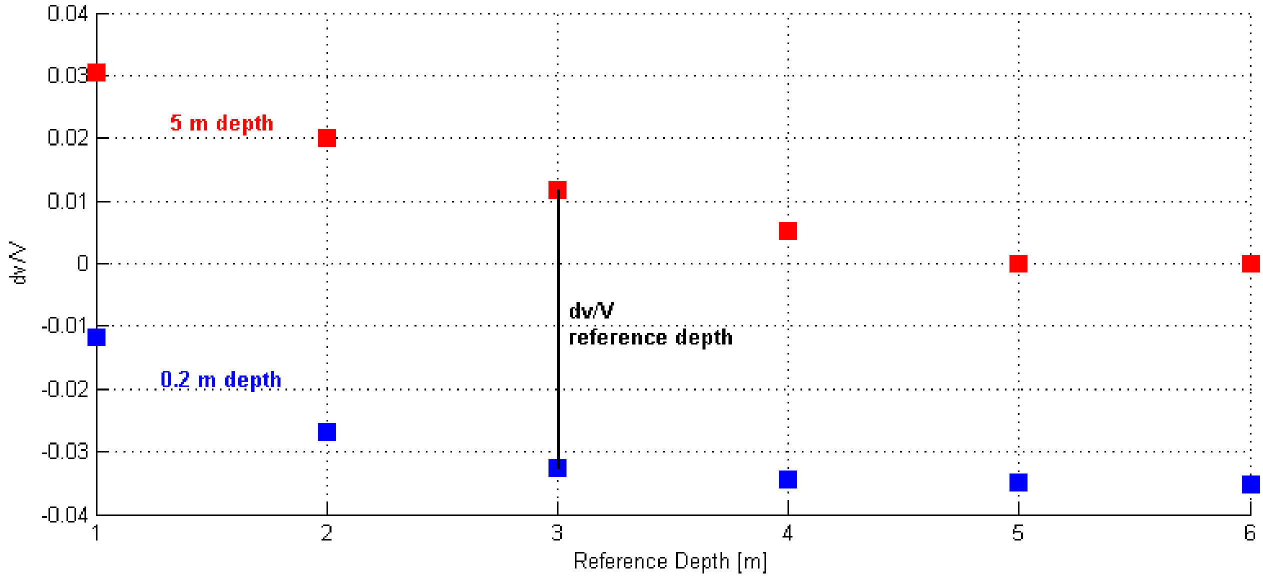

Figure 71 – Seismic Velocity Variations dv/V as a function of water table reference.
We move the water table level from 1 m to 6 m (arbitrary choice). Red square values are associated to 5 m depth below the ground level corresponding to the deeper observable value. Instead, blue squares are associated to 0.2 m the ground level that is the shallow level ever reached during the observations (aquatroll sensor). The black line illustrates dv/V got for 3 m depth that is the average value taken from observations.

The amplitude of the seismic velocity variations (dv/V) is consistent with changes observed in ambient noise correlation. In order to assess the goodness of the method, we have to verify also the frequency range in which we obtain these values (*Figure 72*).

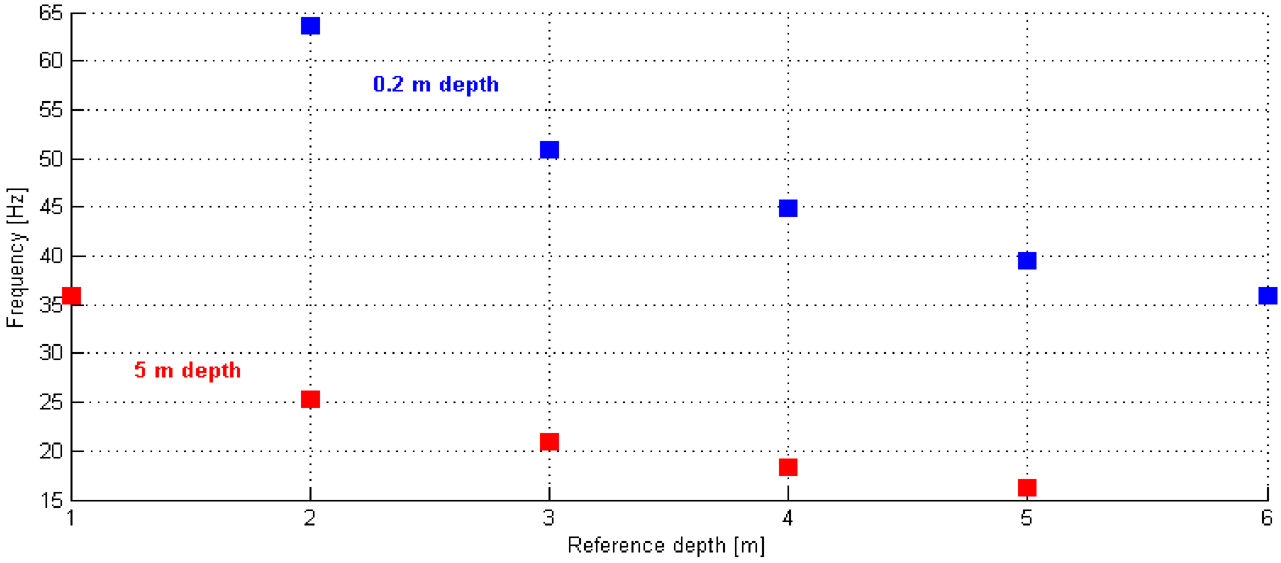

\

Figure 72 – *Frequency values as a function of water table reference.*
Frequency values (red and blue squares) as a function of water table reference. Red values are related to 5 m depth (minimum level of the upper-perched water table) and to 0.2 m depth (higher water table level).

It is possible to see by Figure e that, considering the average observable value (3 m depth) the frequency range is between 20 to 50 Hz associated to 4 % dv/V amplitude (- 3 % to 1 %) (Figure f). We know from cross correlation of ambient seismic noise that dv/V amplitude is associated to 6-7 Hz frequency band. Therefore, there is not a consistency of the frequency values. It would be recommended to consider more complex model considering the rising damp as well as realise more accurate vertical water content measures.

\

5 Conclusions

The aim of this work was to achieve a multidisciplinary monitoring study of a slow moving clayey landslide for better understanding ambient seismic noise cross correlation method by two monitoring approach. The conventional approach consisted in cross correlating a pair of seismological stations while the single station approach consisted in cross correlating different components of the same station. Our application case study was Mas d'Avignonet landslide (France), a large clayey landslide included since 2007 to the French National Landslide Observatory (OMIV) network benefiting from multi-parameter monitoring.

The first part of this work consisted in analysing the multi-physical data collected by monitoring stations and sensors scattered in a degraded active area of the landslide. Considering the presence of water in soil as a triggering factor of a landslide, we combined firstly Meteorology (with a special regard to rainfalls), Piezometry (water table levels), Time Domain Reflectometry (volumetric water content), Spontaneous Potentials (electric potential) and Geodesy (relative displacement of a permanent GPS station) in order to study the influence of hydrology in landslide evolution.

Considering an upper-perched water table, we assessed the correlation among these physical quantities. Particularly, we noticed that continuous rainfalls and snowmelt are responsible of replenishment and depletion of upper-perched water table. However, in summer the high temperatures and prolonged dry periods cause the formation of fissures that could lead to water runoff in case of heavy rains. This phenomenon could be a sensitive factor controlling landslide dynamics. Geodesy confirmed this consideration because the replenishment of a fissure at the end of 2012 (observable by a sudden increase) triggered an acceleration of relative displacement in landslide direction even if the GPS station is not directly in the degraded area but right next to it. Moreover, we analysed the volumetric water content (TDR) observing annual oscillations due to fluid saturation changes well correlated to outdoor conditions. It was even possible to define the heterogeneity of the shallow layers. Finally, spontaneous potentials showed a behavioural change during the examined period but these measurements are difficult to interpret.

We detected also a deeper water table that shows a change in behaviour and we assume that a malfunctioning of the piezometer could provoke it. This assumption has to be verified better understanding the complex hydrogeology of the landslide.

After these data acquisition and interpretation phases, we carried out geophysical surveys on site: EM31 (Electromagnetic method) and ERT (Electrical Resistivity Tomography survey) in order to map the different bearing of this area with conductivity measures. We resumed the previous electrical surveys (Bièvre, 2010) and we performed EM31 campaign in order to define the surface extension of the conductive anomaly. We saw that it is more or less oriented perpendicular to the slope, confirming the shallow tensions and fissures. Therefore, in order to characterize this feature at depth, we acquired a 3D electrical survey (ERT), successfully imaging this anomaly. The final purpose would be defining the conductive anomaly's cause. It could be due to a soil with a high presence of water or clay. Therefore, we recommend boreholes' realisation in the affected area or an IP tomography depending on the budget available.

In a second part, we analysed ambient seismic noise cross correlation results with two approaches. The conventional one consists in cross correlating the seismic records of a station pair in order to detect medium changes (here, water table and fluid saturation changes) with seismic velocity variations (dv/V)

\

supposed to be Rayleigh waves' propagation. Indeed, the results are consistent with the upper-perched water table changes with amplitude between -1 % and 3 % (frequency broadband) respect to the reference got by averaging the signal for all the period of interest (2007-2015). In addition, a specific frequency bandwidth supports medium changes. Alternatively, a non-conventional empirical approach consisting in cross correlating seismic records of a single station was tested because it allows a reduction in monitoring equipment and also because it provides more local information. However, the results show a poor consistency with water table changes because of the influence of noise sources everywhere. It would be recommended to consider more complex model considering the rising damp as well as realise more accurate vertical water content measures.

Finally, we applied the principles of the Biot-Gassmann homogenization theory with the hypothesis of poroelasticity. We retrieved the amplitude of seismic velocity changes as a function of frequency with a fluid substitution approach to mimic the water saturation effect. It also confirmed that a limited frequency band contain the seismic changes, suggesting a localised change of the medium (water table depth). However, the theoretical frequency range exhibits different results compares to the one obtained from the ambient noise method on real data.

In this work, we tried to develop a multidisciplinary monitoring survey in order to get a general overview of landslides problematic. However, this transversal approach could not explain completely these complex phenomena but it wants to give a methodology to face them. This work wants to be only a starting point in order to exploit all the way the potentials of seismic ambient noise correlation in landslide monitoring. In order to go into more detail it would be recommended to search for new understanding analysing specifically every methodology employed.

\

References

Ardhuin F., E. Stutzmann, M. Schimmel, A. Mangeney, (2011). *Ocean wave sources of seismic noise.* Journal of Geophysical Research (JGR) - Oceans, 116(C09004), 21 p.

Bensen G. D., Ritzwoller M. H., Barmin M. P., Levshin A.L., Lin F., Moschetti M. P., Shapiro N. M. and Yang Y., (2007), *Processing seismic ambient noise data to obtain reliable surface wave dispersion measurements*, Geophys. J. Int. (2007) 169, 1239–1260.

G. Bièvre, (2010). *Caractérisation de versants argileux instables dans des conditions hydrogéologiques hétérogènes. Approche géophysique.* , PhD thesis, Sciences de la Terre, de l'Univers et de l'Environnement, Université Joseph Fourier - Grenoble I.

Bièvre, G., Kniess, U., Jongmans, D., Pathier, E., Schwartz, S., Villemin, T., and Zumbo, V., (2011). *Combined use of remote-sensing and ground geophysical techniques to investigate geological control of two landslides in the Trièves area*.

Brenguier, F., M. Campillo, C. Hadziioannou, N. M. Shapiro, R. M. Nadeau, and E. Larose, (2008a), *Postseismic relaxation along San Andreas fault at Parkfield from continuous seismological observations*. Science, 321(5895), 1478-1481.

Brenguier, F., N. M. Shapiro, M. Campillo, V. Ferrazzini, Z. Duputel, O. Coutant, and A. Nercessian, (2008b). *Towards forecasting volcanic eruptions using seismic noise*, Nature Geoscience, 1(2), 126-130.

Brenguier F., Clarke D., Aoki Y., N. M. Shapiro, M. Campillo, V. Ferrazzini, (2011). *Monitoring volcanoes using seismic noise correlations*, C. R. Geoscience 343 (2011) 633–638, doi:10.1016/j.crte.2010.12.010.

A. Bronner, (2009). *Combinaison de données météorologiques et géophysiques pour la caractérisation de mouvements de terrain. Application au glissement du Mas d'Avignonet dans les argiles du Trièves.* Mémoire d'ingénieur, EOSt Strasbourg, LGIT Grenoble.

Campillo, M., and A. Paul (2003), *Long-range correlations in the diffuse seismic coda*, Science, 299, 547 – 549.

Cruden, D. M., and D. J. Varnes (1996), *Landslide types and processes.* In Landslides*: Investigation and Mitigation.* Special Report 247., edited by K. A. Turner and R. L. Schuster, pp. 36-75, Transportation Research Board, Washington.

Corwin, R. F., (1990), *The self-potential method for environmental and engineering applications*, in Ward, S. H., editor, Geotechnical and Environmental Geophysics, Volume I: Review and Tutorial, Society of Exploration Geophysicists, Tulsa.

Duputel Z., V. Ferrazzini, F. Brenguier, N. M. Shapiro, M. Campillo, A. Nercessian, (2009). *Real time monitoring of relative velocity changes using ambient seismic noise at the Piton de la Fournaise volcano (La Réunion) from January 2006 to June 2007*, Journal of Volcanology and Geothermal Research 184 (2009) 164–173.

B. Dupuy, (2011). *Propagation des ondes sismiques dans les milieux multiphasiques hétérogènes : modélisation numérique, sensibilité et inversion des paramètres poroélastiques*. Sciences de la Terre. Université de Grenoble. Français.

Dupuy, B., L. De Barros, S. Garambois, and J. Virieux (2011), *Wave propagation in heterogeneous porous media formulated in the frequency-space domain using a discontinuous Galerkin method*, Geophysics, 76(4), N13-N28.

\

Garambois, S., A. Quinterro, C. I. Massey, and C. Voisin (2010) *Azimuthal and thickness variabilities of seismic site effect response of the Utiku landslide (North Island, New Zealand)*, in EGU General Assembly, edited, p. 2430, Vienna, Austria.

C. Hadziioannou, (2011). *Ondes sismiques en milieu complexe : Mesure des variations temporelles des vitesses.* École Doctorale Terre, Univers, Environnement. Laboratoire de Géophysique Interne et Tectonophysique (LGIT). Université de Grenoble.

Jongmans, D., Renalier, F., Kniess, U., Bièvre, G., Schwartz, S., Pathier, E., Orengo, Y., and Villemin, T. (2008). *Characterization of the Avignonet landslide (French Alps) using seismic techniques.* In Chen, Z., Zhang, J.-M., Wu, F.-Q., and Li, Z.-K., editors, *Landslides and engineered slopes. From the past to the future*, page 1850. Taylor and Francis Group, London. ISBN 978-0-415-41196-7.

Jongmans, D., Bièvre, G., Schwartz, S., Renalier, F., and Beaurez, N. (2009). *Geophysical investigation of the large Avignonet landslide in glaciolacustrine clays in the Trièves area (French Alps).* Engineering Geology, 109:45-56.

Larose, E., et al. (2015), *Environmental Seismology: What can we learn on Earth Surface processes with ambient noise?*, Journal of Applied Geophysics, 116, 62-74.

Mainsant, G., E. Larose, C. Broennimann, D. Jongmans, C. Michoud, And M. Jaboyedoff (2012), *Ambient seismic noise monitoring of a clay landslide : Toward failure prediction*, Journal of Geophysical Research-Earth Surface, 117.

A. Mordret, M. Landes, N. M. Shapiro, S. C. Singh and P. Roux, (2014). *Ambient noise surface wave tomography to determine the shallow shear velocity structure at Valhall: depth inversion with a Neighbourhood Algorithm*, Geophys. J. Int. (2014) 198, 1514–1525.

C. Moulin and C. Chapeau, (2004). *Le glissement de La Salle en Beaumont (Isère): Proceedings of the workshop Ryskhydrogeo*. Program Interreg III. La Mure (France).

C. Moulin and Y. Robert, (2004). *Le glissement de l'Harmalière sur la commune de Sinard : Proceedings of the workshop Ryskhydrogeo.* Program Interreg III. La Mure (France).

Picarelli, L., G. Urcioli, M. Ramondini, L. Comegna, (2005). *Main features of mudslides in tectonised highly fissured clay shales*, April 2005, Volume 2, pp 15-30.

F. Renalier, (2010). *Caractérisation sismique de sites hétérogènes à partir de méthodes actives et passives : variations latérales et temporelles*, PhD thesis, Sciences de la Terre, de l'Univers et de l'Environnement, Université Joseph Fourier - Grenoble I.

Requillard, J.P. and C. Moulin (2004). *Glissement du Mas sur la commune d'Avignonet (FRANCE), Etat de la gestion du risque en octobre 2004*. Restauration des Terrains de Montagne, 2004.

RESIF (2006) French Multidisciplinary Observatory of Versant Instabilities. RESIF - Réseau Sismologique et géodésique Français. http://dx.doi.org/10.15778/RESIF.MT

Sens-Schoenfelder, C., and U. Wegler (2006), *Passive image interferometry and seasonal variations of seismic velocities at Merapi Volcano, Indonesia*, Geophysical Research Letters, 33(21).

N. M. Shapiro and M. Campillo, (2004). *Emergence of broadband Rayleigh waves from correlations of the ambient seismic noise*, Geophysical Research Letters, vol. 31, L07614, doi:10.1029/2004GL019491.

Shapiro, N. M., M. Campillo, L. Stehly, and M. H. Ritzwoller, (2005). *High-resolution surface-wave tomography from ambient seismic noise*, Science, 307(5715), 1615-1618.

\

Snieder, R. et al., (2002). *Coda Wave Interferometry for Estimating Nonlinear Behaviour in Seismic Velocity*. Science 295, 2253; DOI: 10.1126/science.1070015.

Stehly, L., B. Fry, M. Campillo, N. M. Shapiro, (2006). *A study of the seismic noise from its long-range correlation properties*, Journal of Geophysical Research-Solid Earth, 111(B10).

Voisin C.[1], S. Garambois[1], C. Massey[2], R. Brossier[1], (2016) *Monitoring of a Deep Seated Slow Moving Landslide by Ambient Seismic Noise*. [1]Université de Grenoble, CNRS, ISTERRE (France); [2]GNS Science, Lower Hutt, New Zealand. Unprinted paper.

Vuillermet, E., Cordary, D., and Giraud, A. (1994). *Caractéristiques hydrauliques des argiles litées du Trièves (Isère)*. Bulletin of the International Association of Engineering Geology, 49:85–90.

Vuillermet, E. (1990). *Caractéristiques géotechniques des argiles glacio-lacustres du Trièves*. PhD thesis, Université Joseph Fourier, Grenoble, France.

Wapenaar, K., (2004). *Retrieving the Elastodynamic Green's Function of an Arbitrary Inhomogeneous Medium by Cross Correlation*.

Wegler, U., and C. Sens-Schoenfelder (2007), *Fault zone monitoring with passive image interferometry*, Geophysical Journal International, 168(3), 1029-1033.

Wilkinson Paul B., Jonathan E. Chambers, Philip I. Meldrum, David A. Gunn, Richard D. Ogilvy, and Oliver Kuras, (2010). *Predicting the movements of permanently installed electrodes on an active landslide using time-lapse geoelectrical resistivity data only*. Geophysical Journal International (2010) 183, 543-556.

Web references

http://eqseis.geosc.psu.edu/~cammon/HTML/Classes/IntroQuakes/Notes/waves_and_interior.html

http://www.geos.ed.ac.uk/homes/imain/Attenuation.pdf

http://volc_seis_commission.leeds.ac.uk/indexa63d.html?option=com_content&task=view&id=75&Itemid=29

http://omiv.unice.fr/index.php?page=meteo_avgn

http://omiv.osug.fr/SISMO/resif_WS_procedure.html

http://www.regione.toscana.it/documents/10180/11691226/atti_130112_4.pdf/5d14d6c6-a63d-4140-9ef0-e2fe83a3d34b;jsessionid=5324899627D6CA5D2EF3A57D969649DB.web-rt-as01-p1?version=1.0

https://en.wikipedia.org/wiki/Poromechanics

http://www.appstate.edu/~marshallst/GLY3160/lectures/12_Resistivity.pdf

https://www.liag-hannover.de/fileadmin/user_upload/dokumente/Grundwassersysteme/BURVAL/buch/077-088.pdf

http://www.geo.mtu.edu/~ctyoung/LOKENOTE.PDF

\